Electrostatically Actuated LIGA-MEMS Structures with High Aspect Ratio Beams for RF Applications and Mechanical Property Extraction

A Thesis Submitted to the

College of Graduate Studies and Research

in Partial Fulfillment of the Requirements for the Degree of

Doctor of Philosophy

in the Department of Electrical and Computer Engineering

University of Saskatchewan

Saskatoon, Saskatchewan

by

Darcy Haluzan

PERMISSION TO USE

In presenting this thesis in partial fulfillment of the requirements for a Postgraduate degree from the University of Saskatchewan, I agree that the Libraries of this University may make it freely available for inspection. I further agree that permission for copying of this thesis in any manner, in whole or in part, for scholarly purposes may be granted by the professor or professors who supervised my thesis work or, in their absence, by the Head of the Department or the Dean of the College in which my thesis work was done. It is understood that any copying or publication or use of this thesis or parts thereof for financial gain shall not be allowed without my written permission. It is also understood that due recognition shall be given to me and to the University of Saskatchewan in any scholarly use which may be made of any material in my thesis.

Requests for permission to copy or to make other use of material in this thesis in whole or in part should be addressed to:

Head of the Department of Electrical and Computer Engineering
University of Saskatchewan
Saskatoon, Saskatchewan, Canada
S7N 5A9

ABSTRACT

Microelectromechanical systems (MEMS) devices have been increasing in popularity for radio frequency (RF) and microwave communication systems due to the ability of MEMS devices to improve the performance of these circuits and systems. This interdisciplinary field combines the aspects of lithographic fabrication, mechanics, materials science, and RF/microwave circuit technology to produce moving structures with feature dimensions on the micron scale (micro-structures). MEMS technology has been used to improve switches, varactors, and inductors to name a few specific examples. Most MEMS devices have been fabricated using planar micro fabrication techniques that are similar to current integrated circuit (IC) fabrication techniques. These techniques limit the thickness of individual layers to a few microns, and restrict the structures to have planar and not vertical features.

One micro fabrication technology that has not seen much application to microwave MEMS devices is LIGA, a German acronym for X-ray lithography, electroforming, and moulding. LIGA uses X-ray lithography to produce very tall structures (hundreds of microns) with excellent structural quality, and with lateral feature sizes smaller than a micron. These unique properties have led to an increased interest in LIGA for the development of high performance microwave devices, particularly as operating frequencies increase and physical device size decreases. Existing work using LIGA for microwave devices has concentrated on statically operating structures such as transmission lines, filters, couplers, and antennas. This research uses these unique fabrication capabilities to develop dynamically operating microwave devices with high frequency performance.

This thesis documents the design, fabrication and testing of LIGA-MEMS variable capacitors that exploit the vertical dimension. Also included are methods to improve both the reliable fabrication and operation of these devices as well as material property characterization. Variable capacitors can be found in systems such as voltage-controlled oscillators, filters, impedance matching networks and phase shifters. Important figures-of-merit for these devices include the quality factor (Q), tuning range and tuning voltage.

Two different types of variable capacitors are presented, a pull-away design and a design

based on the principle of leveraged bending. The pull-away style variable capacitors were found to have high Q-factors, especially the devices fabricated using a thick gold device layer. As an example, the small gold half capacitance electrode design features a Q-factor of 95 at an operating frequency of 5.6 GHz and a tuning ratio of 1.36:1 with a tuning voltage range of 0 to 7.8 V.

The design based on leveraged bending significantly improves the tuning ratio to a value of 1.9:1 while still maintaining a high Q-factor similar to those found in the pull-away style designs. A further increase in tuning ratio to a value of approximately 2.7:1 would be possible, based on simulated results, by simply changing the angle of the capacitance electrode in the layout.

To improve device performance and fabrication reliability, modifications were made to both the fabrication process and the device layout. In the fabrication process the exposure step, electroplating step, and the etching process were modified to improve the quality of the resulting devices. In the layout, anti-stiction measures were introduced that reduce the contact area during collapse.

To improve device characterization as well as the feedback link between simulation and fabrication, a set of test structures called VM-TEST was developed to accurately determine the important mechanical material properties of thick electroplated layers. These structures utilize the measurement of the pull-in voltage in cantilever and fixed-fixed beams, along with measured structure dimensions, to accurately extract the mechanical properties. Both nickel and gold test structures were analyzed with extracted Young's modulus values of 186.2 and 60.8 GPa respectively.

Also presented is a study of the gap shape in cantilever and fixed-fixed beams that significantly reduces the pull-in voltage while still maintaining a required maximum actuator displacement. It was shown that in the case of cantilever beam actuators, an approximately 40% reduction in pull-in voltage is possible, and in the case of fixed-fixed beam actuators, an approximately 30% reduction is possible by simply varying the shape of the gap between the beam and actuator electrode. These results can be used to significantly reduce the pull-in voltage of future designs.

These promising results show that the LIGA fabrication process is capable of produc-

ing high performance dynamically operating RF MEMS devices, by exploiting the vertical dimension, not typically performed in most existing RF MEMS designs.

ACKNOWLEDGEMENTS

I would like to thank my supervisors, Dr. David M. Klymyshyn and Dr. Sven Achenbach for their guidance, assistance, patience and support throughout this project.

I would also like to thank all the personnel at the Institute for Microstructure Technology (IMT) at the Karlsruhe Institute for Technology (KIT) in Karlsruhe, Germany for making possible the fabrication of the devices found in this work and allowing me to spend time there fabricating devices and learning about the LIGA process. In particular, the contributions made by Dr. Martin Börner were invaluable to the project.

Financial assistance for this project was provided by the Natural Sciences and Engineering Research Council of Canada (NSERC), TRLabs and the Canadian Space Agency (CSA), which was greatly appreciated. TRLabs also provided access to the testing equipment used for this work.

I would also like to thank Dr. Jost Goettert and the staff at the Center for Advanced Microstructures and Devices (CAMD) in Baton Rouge, LA for allowing me to visit and providing device fabrication assistance. Also Venkat Subramanian and Garth Wells at the Synchrotron Laboratory for Micro and Nano Devices (SyLMAND) at the Canadian Light Source (CLS) provided device fabrication and testing assistance, which was greatly appreciated.

Last, but not least, I'd like to thank my family and friends. In particular, I'd like to thank my parents, Tony and Linda, for their amazing support and encouragement, the Reiber family, including my sister Jody, Kurt, Mason, Denae and Cohen for being so much fun to spend time with and of course my wonderful family, Glenda, Ariana and Ellisyn for bringing me so much happiness.

TABLE OF CONTENTS

LIST OF FIGURES

LIST OF TABLES

LIST OF ABBREVIATIONS

2-D	two dimensional
3-D	three dimensional
ALD	atomic layer deposition
CAD	computer aided design
CAMD	Center for Advanced Microstructures & Devices
CLS	Canadian Light Source
CPW	coplanar waveguide
CSA	Canadian Space Agency
DC	direct current
DI	de-ionized
DXRL	deep X-ray lithography
EM	electromagnetic
ESSOLV	electrostatic structural solver
FD	finite difference
FE	finite element
FEM	finite element method
FZK	Forschungszentrum Karlsruhe
	(Research Centre Karlsruhe)
GSG	ground-signal-ground
HF	hydrofluoric
HFSS	high frequency structure simulator
IC	integrated circuit
IMT	Institut für Mikrostrukturtechnik
	(Institute for Microstructure Technology)
IPA	isopropyl alcohol; isopropanol
ISS	impedance standard substrate

KIT	Karlsruher Institut für Technologie (Karlsruhe Institute of Technology)
LIGA	a German acronym for a process consisting of LIthografie (lithography), Galvanoformung (electroplating), and Abformung (moulding)
M-TEST	MEMS test structures
MEMS	microelectromechanical systems
MUMPS	multi-user MEMS process
NSERC	Natural Sciences and Engineering Research Council of Canada
PMMA	poly(methyl methacrylate)
RF	radio frequency
SAMs	self assembled monolayers
SEM	scanning electron microscope
SOLT	short-open-load-through
SRF	self resonant frequency
SyLMAND	Synchrotron Laboratory for Micro and Nano Devices
TIM	tunable impedance matching
VCO	voltage-controlled oscillator
VLSI	very large scale integration
VM-TEST	vertical MEMS test structures
VNA	vector network analyzer

LIST OF VARIABLES

a	incident wave matrix
a_n	amplitude of incident wave at the n^{th} port
A	capacitor plate area
b	reflected wave matrix
b_n	amplitude of reflected wave at the n^{th} port
C	capacitance
C_o	capacitance at the operating frequency
C_P	parasitic parallel capacitance
d	distance between plates; air gap distance
d_{flat}	distance from beam to electrode flat
d_{linear}	distance from beam to linear extrapolation point
d_{max}	maximum gap distance
d_{min}	minimum gap distance
E	elastic (Young's) modulus; electric field intensity
$\tilde{E}$	effective elastic (Young's) modulus
f_{R}	mechanical resonant frequency
f	frequency
f_o	operating frequency
F	force
g	acceleration due to gravity [9.81 m/s^2]
h	beam height
H	magnetic field intensity
I	moment of inertia; current; identity matrix
l	beam length
L	inductance
L_S	parasitic series inductance
M	beam mass

n	number of ports; polynomial order
N_{EC}	elastocapillary number
N_P	peel number
P	power
q_T	charge on capacitor top plate
q_B	charge on capacitor bottom plate
Q	quality factor
R	resistance
R_o	resistance at the operating frequency
R_S	equivalent series resistance
S	scattering matrix
U	potential energy
V	voltage
V_n^+	incident voltage wave at port n
V_n^-	reflected voltage wave at port n
V_{PI}	pull-in voltage
w	beam width
X	reactance
X_c	capacitive reactance
Z	impedance
Z_0	characteristic impedance
Z_{0n}	characteristic impedance (real) of the nth port
α	thermal expansion coefficient
γ_l	liquid surface tension
γ_s	adhesion surface energy
δ	skin depth
$\tan\,\delta$	dielectric loss tangent
ϵ	permittivity
ϵ_0	permittivity of free space [8.854×10^{-12} F/m]

ϵ_r	relative permittivity
θ_c	contact angle
μ	permeability; beam mass per unit length
μ_0	permeability of free space [$4\pi \times 10^{-7}$ H/m]
μ_r	relative permeability
ν	Poisson's ratio
π	mathematical constant [≈ 3.14159]
ρ	resistivity [Ω m]
σ	conductivity
σ_0	residual stress
σ_R	residual stress
$\tilde{\sigma}$	effective residual stress
ω	angular frequency [rad/s]

1. Introduction

1.1 Motivation

The significant performance advantages of microwave microelectromechanical systems (MEMS) devices compared to traditional non-MEMS devices has led to an increase in attention in recent years. Examples of these devices used in radio frequency (RF) circuits include switches, variable capacitors, and inductors found in systems such as voltage-controlled oscillators (VCOs), filters, and phase shifters. They have been developed to replace their on-chip solid-state counterparts, and certain off-chip components. RF MEMS devices have been utilized in low volumes since approximately 2005 mainly for instrumentation applications. Recently, RF MEMS devices have started volume shipping in cellphones. An example is the tunable impedance matching network (TIM) device used for antenna impedance matching, which consists of a network of inductors and digitally tunable low-loss MEMS capacitors from the company WiSpry$^{\text{TM}}$. Forecasters predict worldwide sales of RF MEMS devices to be approximately \$300M U.S. dollars in 2012 and expand to approximately \$800M by 2016 [1].

In the case of variable capacitors, conventional solid-state varactors are made in silicon or gallium arsenide using either p-n or Schottky-barrier junction structures. These devices have room for improvement in all figure-of-merit categories. They often suffer from excessive resistive loss caused by large series resistance and, thus, a low quality factor (Q), and a low electrical self-resonance, due to large parasitics, especially when made on silicon substrates [2]. They feature adequate tuning ratios (typically $>$ 2:1) for most applications, but have poor linearity. Specifications often quote the Q-factor at 50 MHz, with values in the hundreds or thousands, which is not valid at higher frequencies. As an example, in [3], the 1 pF varactor diode has a manufacturer specified Q-factor of 4800 at 50 MHz, from which the series resistance can be calculated to be 0.66 Ω. Measurements of the device at 3 GHz show a Q-factor of 33 and series resistance of 1.64 Ω.

The use of MEMS devices promises high integration. This is attractive since it has the

potential to reduce cost, size, and power consumption [2]. In the case of MEMS variable capacitors, a main advantage is the potential for high Q-factors at high frequencies. At frequencies approaching X-band (8 - 12 GHz) the capacitance value required for most applications can become very small (0.1 - 0.3 pF). Passive components such as a tunable capacitor are rarely used at these high frequencies. With current technologies lumped-element approaches are abandoned for distributed-element or microwave approaches. With the miniaturization capabilities of MEMS technologies, MEMS variable capacitors have the potential to appear lumped at frequencies into the X-band and beyond [4, 5].

The LIGA (German acronym for Röntgenlithographie, Galvanoformung, Abformung - in English, X-ray lithography, electroforming and moulding) fabrication process appears to be very well suited for RF MEMS devices. The fine resolution patterning possible using LIGA allows the designer to produce very accurate structures. Combining this with the deep resist penetration of LIGA potentially allows one to design beams and gaps that are very tall and narrow. Aspect ratios on the order of 100:1 have been demonstrated. When designing variable capacitors that are electrostatically actuated, this is beneficial since actuation voltages decrease with a reduction of either the beam width or the gap size. LIGA is also not restricted to thin metal layers, as are most other MEMS processes. The use of thick metal conductors will reduce the resistance, which leads to devices with higher Q. The thick metal layers allow for a potential decrease in lateral (electrical) size due to the use of the vertical dimension for some applications including capacitors. The use of thick metal layers is also expected to improve power handling capability. Many current MEMS processes are based upon the use of a silicon substrate, which is lossy at higher frequencies. Since LIGA is not restricted to silicon substrates, microwave appropriate substrates can be utilized, which leads to a reduction in parasitics and leads to a higher electrical self-resonance. These strengths found in the LIGA process should lead to MEMS variable capacitors with low actuation voltages, high Q-factors, and high self-resonant frequencies.

However, fabricating long, thin, high aspect ratio beams and gaps in the LIGA process is not trivial. The standard process is not optimized for structures such as these and the most commonly used metal, nickel, is not ideal for RF structures due to a relatively poor conductivity and the fact that it is magnetic, which reduces the skin depth at high frequen-

cies. Also, the material properties of many micro-electroplated metals are unknown and can vary significantly from bulk values and are highly dependant on processing parameters. This uncertainty makes simulations difficult since accurate simulations rely on accurate material properties. Therefore, the improvement of processing for high aspect ratio RF MEMS devices as well as material characterization is as equally important as device design and fabrication.

1.2 Introduction to MEMS

MEMS (microelectromechanical systems) is a name given to encompass the emerging field of microsystems. MEMS devices are becoming increasingly important in the development of new products and systems as miniaturization leads to more desirable components that take up less space, consume less power, and are more convenient to use. The "micro" in the name implies that the dimensions of the devices are in the micrometer scale. They typically range in size from approximately 20 micrometers to 1 millimeter and contain components between 1 and 100 micrometers in size. The "electro" infers that there is electricity or electronics involved. This aspect is usually used as a control mechanism. The "mechanical" term is used to convey the notion of movement. Using the "system" term implies the connection of smaller devices to produce a useful organization.

The development of MEMS devices followed naturally from the development of integrated circuit (IC) fabrication technologies. The performance and cost gains achieved by miniaturizing electrical circuits has led to an interest in miniaturizing devices that rely on mechanics, optics, fluidics, etc. This drive has led to the devices and technologies that the acronym MEMS has come to encompass.

One of the major factors that has led the MEMS drive is integration. MEMS technology promises the ability to integrate mechanical devices such as certain types of sensors, with the electronics that are required to control and analyze the information from these devices. This integration of all required components onto the same substrate is beneficial from many perspectives. As with integrated circuit development, the obvious advantages are an increase in performance and a decrease in cost.

These advantages extend beyond the fields of Electrical and Mechanical Engineering. These devices have found promise in such diverse fields as biomedics, microfluidics, and op-

tics. MEMS devices currently find success in many established products. Examples that have found widespread use include inkjet printer heads, microaccelerometers for automotive airbag systems and smart devices, and micromirrors for optical switching and display systems.

MEMS devices have many obstacles to overcome. The major problems are design, fabrication, integration, packaging, and reliability. MEMS design is challenging in that it often encompasses multiple physics domains simultaneously. The designer must find ways to analyze complex interactions between these different domains. For some of these problems computer aided design (CAD) software can be used. In most cases simulation software does not take into account all of the factors that determine the complete operation of the structure at once. Fabrication of MEMS devices is typically expensive and often not standardized. There are many different methods that can be employed to develop a MEMS device. This is also a problem that affects integration. Integration becomes more difficult when there are multiple methods to produce structures. Packaging is an area of ongoing MEMS research due to the diversity of MEMS devices. Since these devices can be used in many different fields the packaging often needs to reflect the unique requirements of the MEMS device. In capacitive devices that include a dielectric layer, dielectric charging has been shown to limit device lifetime [6]. Also, MEMS devices contain moving parts which could also affect reliability. Most MEMS materials were not historically used as structural materials and are therefore receiving increased attention.

All true MEMS devices have one thing in common, actuation. Actuation refers to the act of affecting or transmitting mechanical motion, forces, and work by a device or system on its surroundings in response to the application of a bias voltage or current [7]. The most common types of actuators are electrostatic and thermal and examples are shown in Figure 1.1. Other types such as magnetic, piezoelectric, shape memory alloys, and hydraulic find occasional uses. They are not used more frequently due to the requirement of exotic materials, which cannot easily be incorporated into many MEMS processes.

Electrostatic actuators have found widespread use due to their simplicity, fast response, and low power consumption. In their simplest form they are two metal structures separated by an air gap. A bias voltage is applied between the metal structures, which results in a

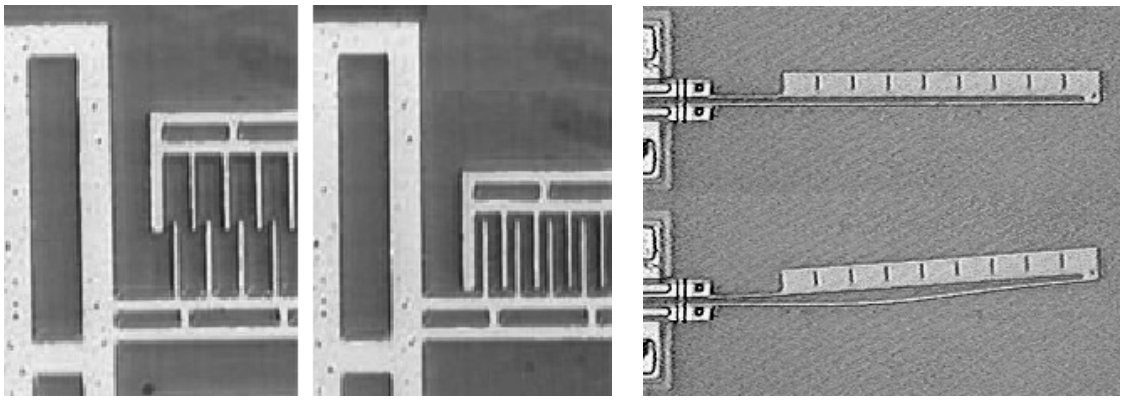

(a) Electrostatic (reproduced from [2])

(b) Thermal (reproduced from [8])

Figure 1.1: Electrostatic and thermal actuators.

separation of charges between them. This produces an electrostatic force that can be used to decrease the gap between the plates. An example of an electrostatic actuator is shown in Figure 1.1(a) [2].

Thermal actuators are often used because they can produce large deflections using a low voltage. The main disadvantages of thermal actuators are that they are power inefficient and react slowly, clearly not desirable qualities for RF MEMS circuits. Thermal actuators often become quite hot, which can be unfavorable from a reliability point of view. They operate on the principle of unequal expansion due to thermal heating. An example of a thermal actuator is shown in Figure 1.1(b) [8]. A current is passed through the thin and thick arms of the actuator. The thin arm will reach a higher temperature than the thick arm, which will cause it to expand more than the thick arm. This results in a displacement of the entire actuator.

1.3 LIGA Fabrication Process

The major steps in the LIGA process are deep X-ray lithography (DXRL) using synchrotron radiation, followed by the electroplating of metals, followed by moulding. The process was developed during the 1980's at the Nuclear Research Centre Karlsruhe (Kernforschungszentrum Karlsruhe), now the Karlsruhe Institute of Technology (Karlsruher Institut für Technologie, KIT) in Karlsruhe, Germany, as a means to produce very small and precise separation nozzles

for uranium isotopes [9, 10]. The institute responsible for the development of the LIGA process at KIT is the Institute for Microstructure Technology (Institut für Mikrostrukturtechnik, IMT).

What distinguishes DXRL from other techniques, is not strictly the small feature size, but the ability to combine "small" structures with "deep" structures that have high accuracies and aspect ratios. Very tall structures can be realized (hundreds of microns) with lateral feature sizes smaller than a micron. Structures with vertical aspect ratios on the order of 100:1 have been demonstrated, which is not currently possible using any other fabrication technique with comparable quality. The sidewalls of these tall structures are typically almost vertical (greater than 89.95°) [11] and very smooth (optical quality roughness) [12]. The entire LIGA process allows the user to create very precise, tall microstructures from a wide range of materials in thick layers such as polymers, metals, and ceramics. These structures can be fabricated on virtually any substrate making the entire process extremely flexible.

These unique properties have led to an interest in LIGA for the development of high performance microwave devices. Existing work using LIGA for microwave devices has concentrated mainly on statically operating structures such as transmission lines, filters, couplers, resonators, inductors and antennas [5, 13–18]. In dynamically operating MEMS devices, certain entities must be free to move during actuation. In many devices using electrostatic actuation, the entity that moves is often a thin beam. If the beam is fixed along one edge it is called a cantilever beam. If it is fixed along two opposite edges it is called a fixed-fixed beam. Two possible ways a beam can be fabricated using the LIGA process are shown in Figure 1.2. In Figure 1.2(a), the cantilever beam is floating above the substrate and is fixed to a large metal piece. This can be accomplished by using the metal electroplating seed layer as a sacrificial layer. The structure shown in Figure 1.2(a) is a cantilever beam, but the sacrificial layer technique can be used to construct fixed-fixed beam structures as well. In Figure 1.2(b) the bottom edge of the cantilever beam is attached to the substrate. This is accomplished by pre-patterning the seed layer. Fixed-fixed type beams cannot be produced simply using this technique as it would require fixing the top edge of the beam. One possible method to accomplish this would be to add a second layer to the process.

The devices discussed in this work were designed to be suitable for fabrication using the

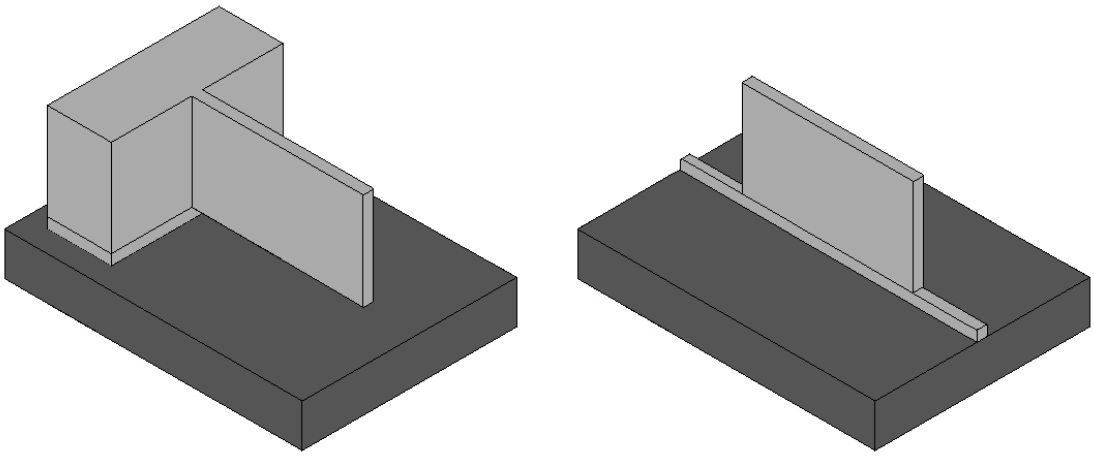

(a) Seed layer as sacrificial layer (b) Pre-patterned seed layer

Figure 1.2: LIGA beam configurations.

seed layer as a sacrificial layer. No devices were designed that could be produced using the patterned seed layer technique. The sacrificial layer technique was chosen for a number of reasons. The first reason is that it requires a single lithography step unlike the patterned seed layer technique, which requires two lithography steps and possibly two masks in different technologies. The second reason is that the patterned seed layer technique requires very precise alignment of the patterned seed layer with the X-ray mask. The precise alignment is necessary since the beam widths and gap sizes are small. Alignment accuracy would depend on the structures, but could be sub-micron which further complicates the process. The third reason is that there are possible problems with the adhesion of the seed layer to the substrate during actuation of the beam. During actuation, if the adhesion of the seed layer and substrate is not strong enough, the seed layer could pull away from the substrate, which would cause a failure of the device. This is not likely a problem with the sacrificial layer technique, since the beam and the connecting region is a continuous metal layer and the connecting area has comparatively large seed layer interface to the substrate. The patterned seed layer technique also does not allow rounding of the connecting edge of the beam, which was shown to be important in [19].

The fabrication steps applicable to the devices in this work are shown in Figure 1.3. The

fabrication process begins with the structure shown in Figure 1.3(a). The bottom layer is the substrate onto which a thin metal film called a seed layer is applied. A wide variety of substrate materials and thicknesses can be used depending on the application. Typically these are 4 inch diameter wafers and range in thickness from 250 - 1000 μm. Examples of common materials include silicon, alumina, and quartz. The thin metal seed layer film is deposited onto the substrate using the sputtering process to a thickness of approximately 3 μm. Typically titanium is used as the seed layer which is then oxidized to form Ti/TiO_x (titanium, oxidized titanium), which will act as a seed layer during electroplating. Titanium is used as it is a compromise between the requirements for good resist adhesion and the ability to initiate electroplating [12]. Next, a photoresist foil of poly(methyl methacrylate) (PMMA) (GS 233) from 100 μm to a few millimetres in thickness is glued to the plating base. Before gluing, the foil is flycut to the predetermined thickness. The glue layer behaves in a similar manner to the PMMA foil during the remaining process steps once it has completely hardened. PMMA is the most common X-ray sensitive resist material that is used and this layer will be patterned to define the MEMS structures.

The next step is to expose the PMMA to X-ray radiation as shown in Figure 1.3(b). An absorber pattern from an X-ray transparent mask is transferred into the PMMA using highly collimated synchrotron hard X-ray radiation with a characteristic wavelength between 0.2 and 0.6 nm. The mask is typically constructed of an absorber pattern on top of a carrier foil. The absorber must have a high atomic weight and therefore a high absorption coefficient. The most common metal used by far is gold, but tantalum and tungsten have also been used [12]. To achieve appropriate absorption the gold layer must be at least 10 μm thick [12]. The carrier foil must have a low absorption coefficient and low thickness so it is as X-ray transparent as possible. Therefore, materials with a low atomic weight are often chosen. The most common materials used are titanium, beryllium, silicon, graphite, and glass. The thickness of the carrier foil must be chosen carefully in order to maintain high transmission levels. Beryllium layers up to 1000 μm can be used, but titanium is limited to a thickness of several micrometers.

The exposed regions of the resist are then dissolved using a suitable developer such as GG developer in the case of PMMA resists as shown in Figure 1.3(c). The dissolved PMMA re-

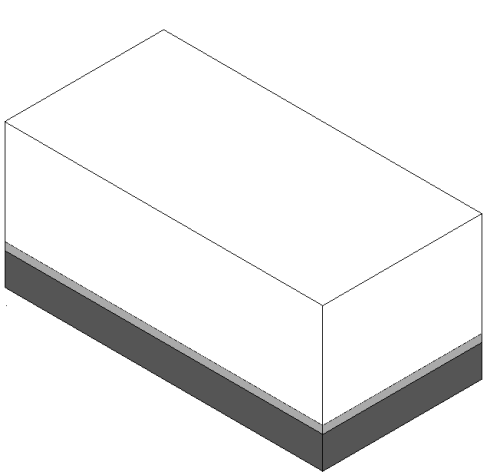

(a) Substrate, seed layer and resist

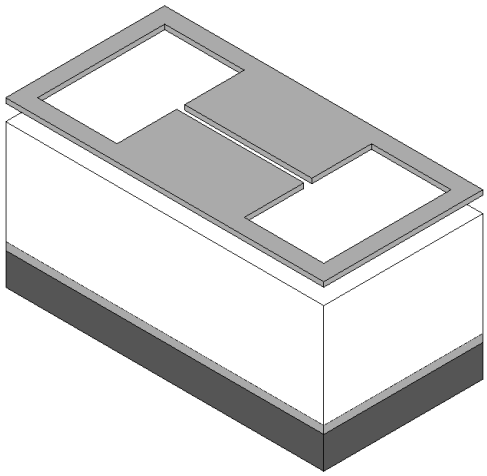

(b) Expose resist using mask

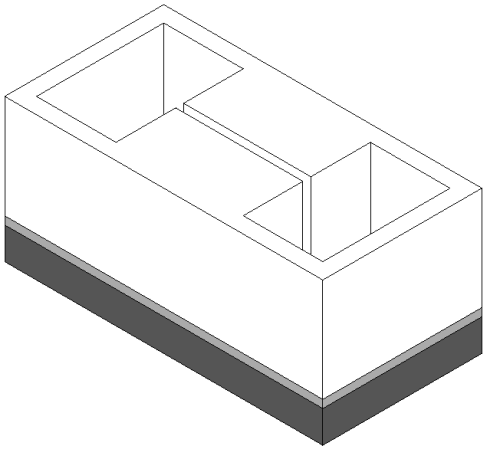

(c) Develop resist

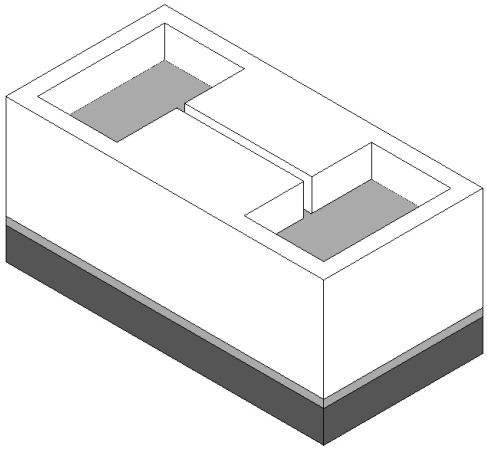

(d) Electroplate

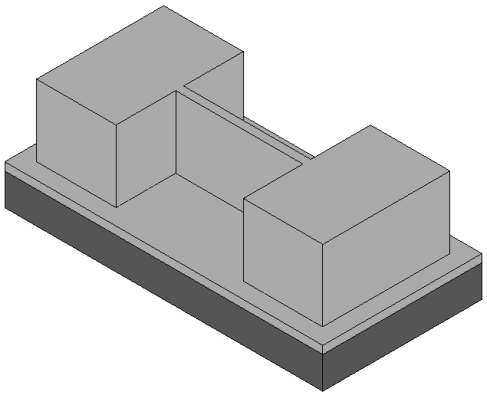

(e) Strip resist

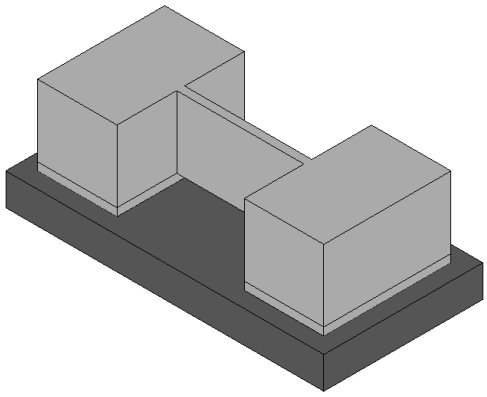

(f) Etch seed layer

Figure 1.3: LIGA fabrication steps using the seed layer as a sacrificial layer.

gions are then filled with metal by micro-electroplating as shown in Figure 1.3(d). The metal deposition starts on the electrically conductive seed layer. The most commonly electroplated metal to date has been nickel due to low internal stresses in the tall metal structures, but copper and gold are finding increased usage. After electroplating, the structure is exposed to X-ray flood irradiation, which allows the remaining PMMA to be removed with developer. The resulting structure is shown in Figure 1.3(e). The titanium seed layer is then selectively etched to release the thin beam and isolate any adjacent metal structures as shown in Figure 1.3(f). Hydrofluoric (HF) acid is commonly used as the etchant because it does not attack the nickel structures [20].

The steps followed if using the patterned seed layer technique are very similar to the previous technique. The main differences include patterning the seed layer using a suitable lithography technique, performing an X-ray exposure that is aligned to the seed layer, and the omission of the HF etching step. During the electroplating process all sections to be plated must be electrically connected. This may require the patterning of temporary sacrificial connections if the structures to be plated require electrical isolation.

1.4 Variable Capacitor Figures-Of-Merit

There are many specifications that are used to evaluate the performance of a variable capacitor. The most important electrical parameters are the unbiased nominal capacitance, tuning ratio, tuning voltage/current, equivalent series resistance or quality factor, and associated inductance or electrical self-resonance.

The unbiased nominal capacitance is the value of capacitance without the application of any tuning signal. This value depends on the requirements of the desired application and the frequency of interest. Required capacitance values for typical impedance values can range from 10 pF for applications around 100 MHz, to 0.1 pF for applications approaching millimeter wave.

The tuning ratio is the ratio of maximum capacitance to minimum capacitance. Some applications require only a small tuning ratio to fine-tune an impedance value, most applications require a ratio of at least 2:1 [2].

For a voltage-controlled capacitor, the tuning voltage is the potential required to tune the

capacitor through its entire range of values. In most cases, this voltage range is required to be as small as possible, so that it is compatible with system control signals. Electrostatically actuated capacitor structures often require voltages well above those typically used in common systems. In this case additional circuitry is required, which can include high-voltage charge pumps and drivers.

A simplified circuit model for the variable capacitor is shown in Figure 1.4. It consists of a variable capacitance (C) and an equivalent series resistance (R_S). For an electrical reactive component, the Q-factor is typically expressed as the ratio of the imaginary portion of the impedance to the real portion ($\mathrm{Im}\{Z\}/\mathrm{Re}\{Z\}$). In this case the Q-factor can be expressed as

$$Q = \frac{1}{\omega C R_S}, \tag{1.1}$$

where ω is the angular frequency ($2\pi f$). Typically in a reactive component a large Q-factor is desirable as it minimizes losses. Another example is in an LC oscillator circuit where phase noise decreases with an increase in the Q-factors of the reactive components.

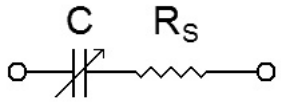

Figure 1.4: Simplified variable capacitor circuit model.

It is important to note that the Q-factor is a function of frequency as the imaginary portion of the impedance varies with frequency. Therefore, the Q-factor could be artificially inflated by operating at an unreasonably low frequency, below the intended operating frequency of the device. Also the equivalent series resistance is not necessarily constant with frequency due to skin depth and other effects. Therefore the Q-factor should be specified at a certain frequency as well as a certain tuning voltage or current.

A more realistic microwave circuit model for a variable capacitor is shown in Figure 1.5. This model includes the parasitic series inductance (L_S) as well as the parasitic parallel

capacitance (C_P). This parasitic inductance in series with the tunable capacitance will resonate at a frequency known as the self-resonant frequency (SRF). At this frequency, the capacitor will appear as a small resistor. At frequencies greater than this the capacitor behaves inductively. The inductance must be kept as low as possible so that the self-resonant frequency is much higher than the frequency the capacitor is intended for. As a general rule of thumb, the self-resonant frequency should be at least double the operational frequency [2]. Beyond the SRF, parallel resonance (the second resonance) occurs when the reactance of the series inductor equals the parallel capacitor.

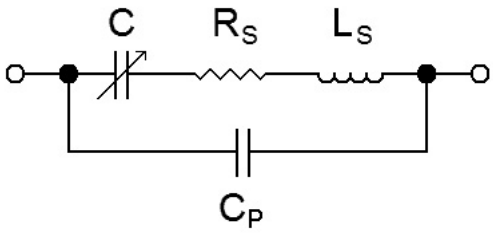

Figure 1.5: Variable capacitor microwave equivalent circuit.

1.5 Existing MEMS Variable Capacitor Designs

Most existing MEMS capacitor designs feature parallel plates, where the capacitance is varied by changing the gap between the plates [21–25]. Traditionally, these plates are limited to planar geometries and lie parallel to the substrate. These devices are constructed from layers that are typically thinner than 5 μm. They are actuated electrostatically, or thermally. Many of these devices have been fabricated using silicon-based thin film processes such as the multi-user MEMS process (MUMPS). Most planar parallel plate designs have focused on the lower end of the microwave frequency range (1 - 3 GHz) with capacitance values between approximately 1 and 4 pF.

An alternate configuration is a lateral comb structure [26–28]. In this geometry, adjusting the overlap of the capacitor fingers changes the capacitance. The direction of actuation is perpendicular to the actuation in parallel plate type capacitors. Device layers as thick as

80 μm have been reported [27]. These layers were constructed using a highly refined deep silicon etch. Lateral comb capacitors have generally been targeted for frequencies in the 100 MHz to 1 GHz frequency range with capacitance values between approximately 1 and 10 pF.

MEMS parallel plate and lateral comb capacitors are designed to operate at the lower end of the microwave frequency range. A variation of the parallel plate configuration called a shunt mounted design is capable of operation at higher frequencies [29–33]. These capacitors are capable of high Q (greater than 100) operation and are typically designed for the 10 - 40 GHz frequency range with capacitance values between 0.1 and 0.3 pF. These shunt mounted devices take more of a distributed approach, relying on coplanar waveguide (CPW) transmission line architecture, rather than a lumped approach, as in the parallel plate and the lateral comb capacitor configurations. A bridge is created over the centre conductor and the two air gaps. A change in air gap between the bridge and the centre conductor changes the capacitance.

To the author's knowledge there are no existing MEMS parallel plate or lateral comb capacitors that are designed for the 3 - 10 GHz frequency region with Q-factors greater than 100. It is believed that the use of thick metal layers and fine resolution patterning capable using the LIGA process will allow the development of capacitors to fill this void. The use of thick metal layers should also significantly increase power handling capabilities compared to a device fabricated using a thin planar fabrication technique. Vertically oriented beams and gaps also have the potential to reduce device area, as this allows the capacitor to sit on edge, rather than lie flat against the substrate. These vertically oriented capacitors can also be used for novel reactive lumped element circuits that occupy considerably less area than their distributed counterparts [5].

The following sections give examples of capacitors that are typical of the different styles mentioned above. These examples are commonly referenced devices in their style category.

1.5.1 Parallel Plate Configurations

In [21], the authors present an aluminum micromachined parallel-plate variable capacitor. The device is shown in Figure 1.6(a). A 1 μm thick sheet of aluminum is suspended in

air approximately 1.5 μm above a bottom aluminum layer, which is situated on top of a silicon substrate. The top plate is held by four mechanical folded-beam suspensions acting as springs. The size of the plate is 200 μm by 200 μm, with a 1.5 μm air gap, which results in a gap capacitance of approximately 200 fF. A DC bias voltage across the capacitor results in an electrostatic force, which reduces the air gap. The suspended plate can be pulled down by at most 1/3 of the original gap size before the top plate collapses onto the bottom plate. This happens because the pull-down force exceeds the mechanical restoring force. This corresponds to a theoretical 50% increase in capacitance or a 1.5:1 tuning range. Four

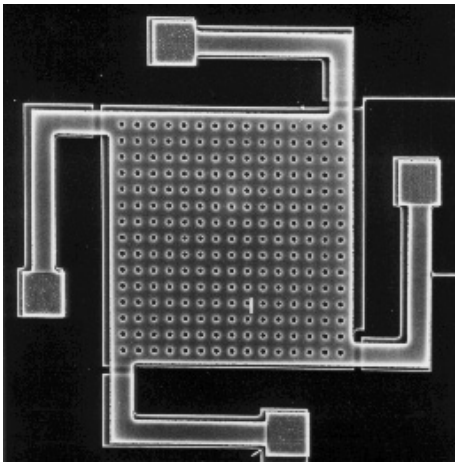

(a) Young et al. (reproduced from [21])

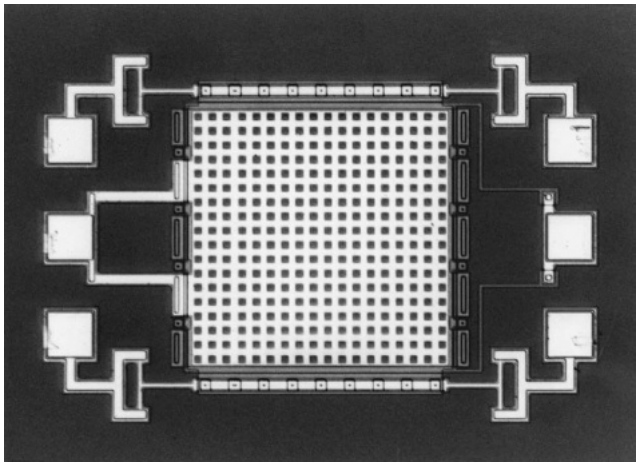

(b) Dec et al. (reproduced from [22])

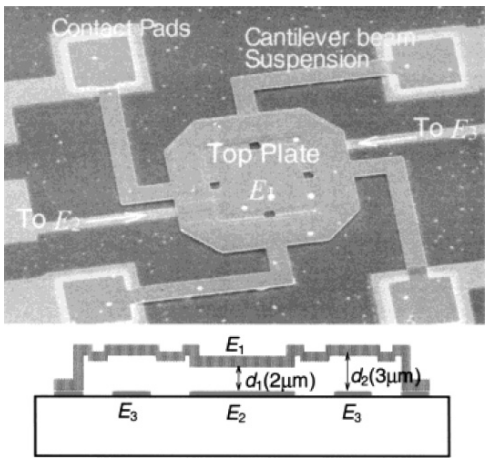

(c) Jou et al. (reproduced from [23])

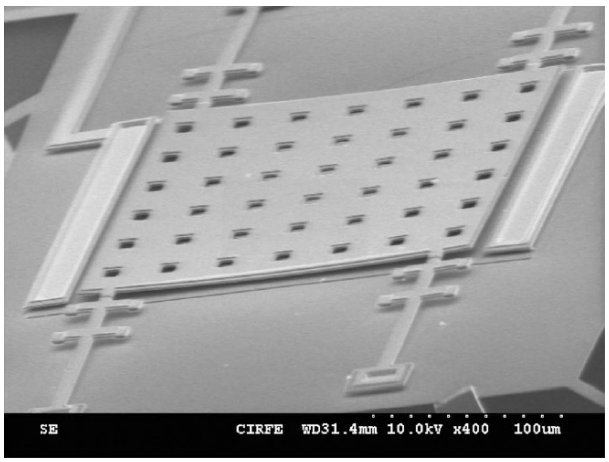

(d) Bakri-Kassem et al. (reproduced from [25])

Figure 1.6: Parallel plate capacitor configurations.

variable capacitors were wired in parallel to achieve an 800 fF gap capacitance. The nominal capacitance is substantially larger due to fixed parasitics. With a 5.5 V tuning voltage, the capacitance can be varied between 2.11 pF and 2.46 pF. This corresponds to a tuning range of 16% or 1.16:1. At 1 GHz the series resistance is 1.2 Ω, which corresponds to a Q-factor of 62 at 1 GHz.

In [22], the authors present a three-plate tunable capacitor that has been designed using MUMPS, which is a standard polysilicon surface micromachining process as shown in Figure 1.6(b). The use of three parallel plates allows the capacitor to achieve a larger tuning range. The plate in the middle is grounded and can be pulled toward the top or bottom plate. With equal air gaps the theoretical tuning range is 2:1. The middle plate can be pulled 1/3 of the distance to the top or bottom plate. This corresponds to a maximum capacitance of 1.5 times nominal and a minimum capacitance of 0.75 times nominal. The actual air gaps used in the design are 0.75 μm for the upper gap and 1.5 μm for the lower gap. The capacitor has a plate size of 398 μm by 398 μm. With an air gap of 0.75 μm, this corresponds to a gap capacitance of 1.9 pF. With no bias voltage the measured nominal capacitance is 4.0 pF, which is due to the contribution of fixed parasitics. With a bias applied between the top plate and the middle plate the maximum achievable capacitance is 6.4 pF. With a bias between the middle plate and the bottom plate the minimum achievable capacitance is 3.4 pF. This corresponds to a measured tuning range of 87% or 1.87:1. The capacitor has a Q-factor of 15.4 at 1 GHz and 7.1 at 2 GHz, with a self-resonant frequency of approximately 6 GHz.

In [23], the authors present a variable capacitor capable of wide tuning range operation, shown in Figure 1.6(c). In this design the top plate is suspended as usual, but the bottom plate consists of two separate plates. One of the bottom plates and the top plate form the variable capacitor, where as the other bottom plate and the top plate provide electrostatic actuation for capacitance tuning. If the capacitance gap is made smaller than the electrostatic actuation gap, the theoretical tuning range will be greater than a conventional parallel plate capacitor's tuning range of 50% or 1.5:1. A capacitor of this design can theoretically have an arbitrarily large capacitive tuning range if the capacitance gap is 1/3 or less the size of the electrostatic actuation gap. In reality the maximum achievable tuning range depends

on other factors such as surface roughness and the curvature of the capacitor plates. The capacitor has a tuning range of 70% or 1.70:1, with a pull-in voltage of approximately 18 V. The difference between the measured and the theoretical value is due to parasitic capacitance. The measured Q-factor is 30 at 5 GHz and the self-resonant frequency is beyond 5 GHz.

In [25], the authors present a two plate variable capacitor, with plate dimensions of approximately 200 by 250 μm, fabricated using the PolyMUMPs process, which is shown in Figure 1.6(d). This device features a top plate that is curled up due to a difference in residual stress in the two layers that compose the top plate, namely polysilicon and gold. The center of the top plate relaxes on the bottom plate and the maximum curl-up amount above the bottom plate is approximately 3 μm. A 100 nm layer of alumina is deposited onto the structure using an atomic layer deposition (ALD) technique to electrically isolate the top and bottom plates. The lossy substrate beneath the varactor plates is etched to reduce the amount of parasitic capacitance. An almost linear capacitance versus voltage response is obtained as the top plate un-curls towards the bottom plate with as increase in actuation voltage. The capacitance changes from approxiamtely 0.7 to 3.4 pF over a voltage range of 0 to 60 V, resulting in a tuning ratio of approximately 5:1. The measured Q-factor of the device is 29 at 1 GHz.

1.5.2 Lateral Comb Configurations

In [26] the authors present a variable capacitor that is based on a lateral comb configuration and is shown in Figure 1.7(a). The device contains a central moveable structure that is electrically grounded. Fixed to this movable structure are electrodes on either side that contain comb fingers. These comb fingers on both sides mesh into a set of stationary fingers. These fingers form two tunable capacitors that are mechanically joined together. One capacitor is for tuning and the other is for RF signals. When a bias voltage is applied between the movable comb fingers and the stationary fingers of the tuning capacitor, the movable fingers are pulled towards the stationary fingers. This causes the movable fingers to be pulled away from the stationary fingers that form the RF capacitor, which leads to a decrease in capacitance. This configuration is preferred when one terminal is to be grounded, because RF

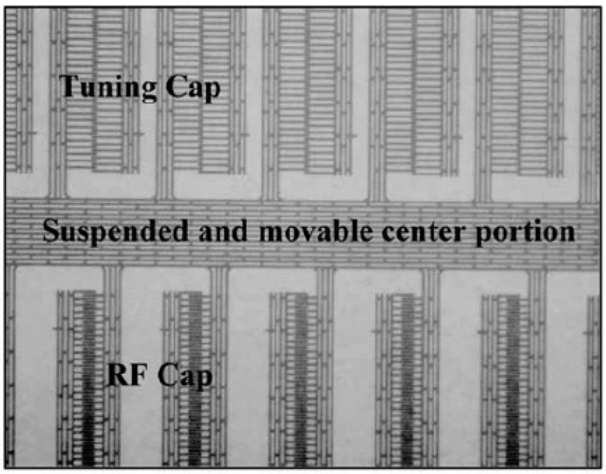

(a) Yao et al. (reproduced from [26])

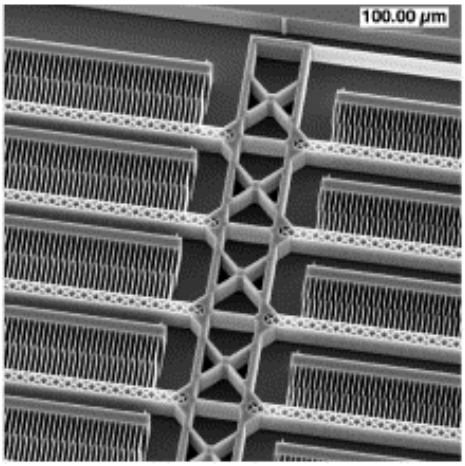

(b) Borwick et al. (reproduced from [27])

Figure 1.7: Lateral comb capacitor configurations.

chokes can be eliminated, since the tuning mechanism is electrically isolated from the RF path. The device consists of a single-crystal silicon device layer held onto a glass substrate using an epoxy adhesive layer. The silicon layer is between 20 and 30 µm thick, and the adhesive layer is 20 µm thick. A coating of aluminum on top of the silicon is used to reduce the equivalent series resistance. The capacitance of the device with no actuation voltage is 5.19 pF and the self resonance is 5 GHz. At 500 MHz the equivalent series resistance is 1.8 Ω, which corresponds to a Q-factor of 34. The minimum capacitance is 2.48 pF with a tuning voltage of 5 V. This corresponds to a tuning ratio of about 100% or 2:1. Interdigitated comb structure based capacitors do not have a theoretical tuning range limit.

In [27] the authors present a device that is very similar in operation to the device in [26] and is shown in Figure 1.7(b). Similar to [26] this capacitor features a thick, aluminum coated, single crystal silicon device layer suspended over a glass substrate. The previous process was improved to allow the production of thicker device layers. The device layer shown in Figure 1.7(b) is 40 µm, but layers as thick as 80 µm have been produced with finger widths of 2 µm. The geometry of the device in [26] was changed to achieve a larger tuning range. In addition, both sets of stationary comb fingers are on the same side of the movable comb fingers. This results in an increase in capacitance as the bias voltage is

increased. The capacitor is capable of a 740% or 8.4:1 tuning range. Although theoretically the device thickness should not affect the tuning range, the ratio of parasitic capacitance to base capacitance of the device is greatly improved with a thicker device layer. This effect has allowed the tuning ratio to be greatly increased [27]. The thicker device layer also reduced the series resistance to less than 1 Ω. This increased the Q of the device to above 100 for frequencies up to 700 MHz and above 30 for frequencies up to 2.25 GHz.

1.5.3 Distributed Shunt Mounted Configurations

A capacitor that makes use of a parallel plate design, shunt mounted over a coplanar waveguide transmission line, is presented in [29] and is shown in Figure 1.8(a). The capacitors were developed using the silicon-MEMS foundry MUMPS process. These structures on a lossy host silicon substrate were transferred to RF circuits designed on a low-loss ceramic substrate. Such a flip-chip assembly and transfer process is the key technology to assure the low-loss microwave and millimeter-wave performance [29]. The capacitor uses electrothermal actuators to move the plate vertically to change the air gap between the plate and the CPW. The moving plate crosses over the centre conductor and gaps. The centre conductor of the 50 Ω CPW is 103 μm wide and the gaps are 48 μm. The size of the plate is 300 μm by 200 μm. The top plate is grounded through the cold arms of the actuator. The

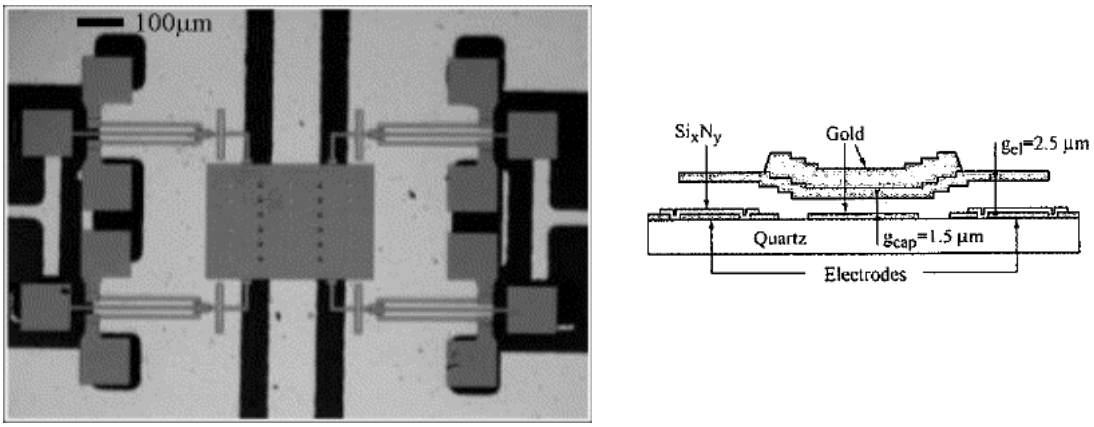

(a) Feng et al. (reproduced from [29]) (b) Dussopt et al. (reproduced from [30])

Figure 1.8: Shunt mounted capacitor configurations.

total capacitance value of the device is about 0.272 pF and the resonance frequency is above 40 GHz. The minimum Q-factor at 10 GHz was measured to be 197.

The capacitor presented in [30] also makes use of a shunt mounted design and is shown in Figure 1.8(b). Unlike the thermally actuated capacitor in [29], this capacitor makes use of an electrostatic actuation mechanism very similar to the actuator used in [23]. It uses the principle of the actuation gap being larger than the capacitance gap to achieve an increased tuning range. In this design the capacitance area is the centre of the bridge, between the bridge and the CPW centre conductor. The two electrodes in the ground plane are used to actuate the device. The area of the plate is 140 μm by 140 μm and the gap is 1.5 μm, which leads to a gap capacitance of 116 fF. The capacitor was fabricated on a quartz substrate using an 88 Ω CPW line with dimensions of 83/133/83 μm. The capacitance values are smaller than expected due to a stress gradient in the electroplated gold which bows up the bridge, resulting in a larger air gap than expected. The capacitor has a tuning ratio of 1.46:1 over a tuning voltage of 24 V. The self-resonant frequency is 83 GHz and the Q-factor is 95-100 at 34 GHz.

1.6 Extracting Material Properties in Thick Metal Layers

Accurate mechanical property parameters are extremely important in MEMS design, since the purpose of many MEMS devices is to deflect accurately given a stimulating force. The most important mechanical parameters required during a design are the elastic (Young's) modulus [E], and residual stress [σ_0]. The adhesion surface energy [γ_s] is also very important from an anti-stiction point of view. The importance is seen in the feedback loop between simulation and fabrication. If accurate mechanical property parameters cannot be extracted from fabricated devices, it is difficult to build accurate simulation models to predict behaviour. Macromechanical data cannot normally be extrapolated to the dimensions of microsystems without experimental confirmation. Hence, materials properties must be tested in specimens on a micrometer scale if microcomponents are to be developed [34].

The majority of existing approaches to determine the mechanical properties of thick electroplated layers involve tensile tests on prestructured specimens [35–43]. Compression tests have also been performed [44], as well as beam bending tests [34, 45, 46] on microbeams

and microposts. The vibration frequency of the structure has also been used to determine the Young's modulus [35, 47]. The majority of these experiments have been focused on nickel, but nickel-iron [35, 37, 38] and copper [34, 44] have also been investigated. Except for the vibration analysis, these tests involve applying a known force (usually with specialized test equipment developed in-house), measuring displacement, and then calculating material properties.

An example of a structure fabricated for a tensile test is shown in Figure 1.9 [48]. This sample is an electroplated then polished nickel tensile specimen mounted on a silicon die. The structure is released from the copper seed layer by wet chemical etching. It is then tensile tested using a test machine having grips that match the wedge shaped ends of the structure. A motorized translation stage pulls the specimen and the load is measured using a load cell. The size of the structure is 200 μm tall by 200 μm wide and has an overall length of 3 mm [36].

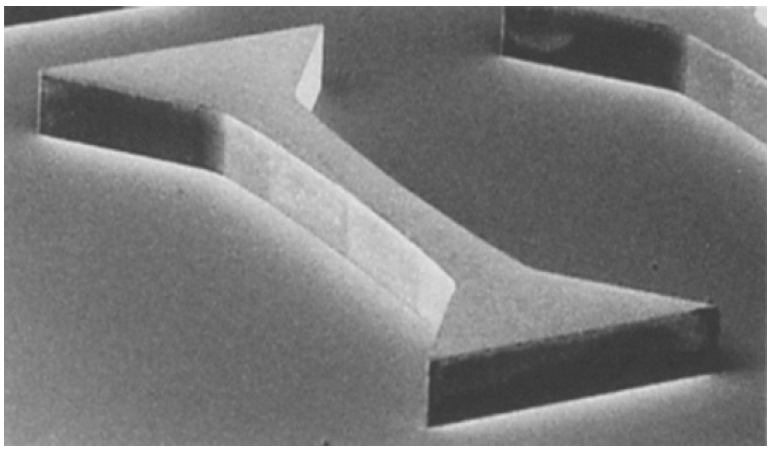

Figure 1.9: Electroplated and polished 200 μm tall LIGA nickel tensile specimen on a silicon substrate (reproduced from [48]).

In [46] a grid of 1 mm tall square posts with dimensions of 160 μm by 160 μm are overplated and then released from the substrate. The overplating yields a set of posts that have a continuous metal attachment so that there are no material or process discontinuities.

Figure 1.10(a) shows untested nickel posts, and Figure 1.10(b) shows deformed posts tested past the failure point. The load is applied horizontally to the post with a loading pointer attached to a force sensor (load cell) and the mechanical properties are extracted from the force versus displacement curve.

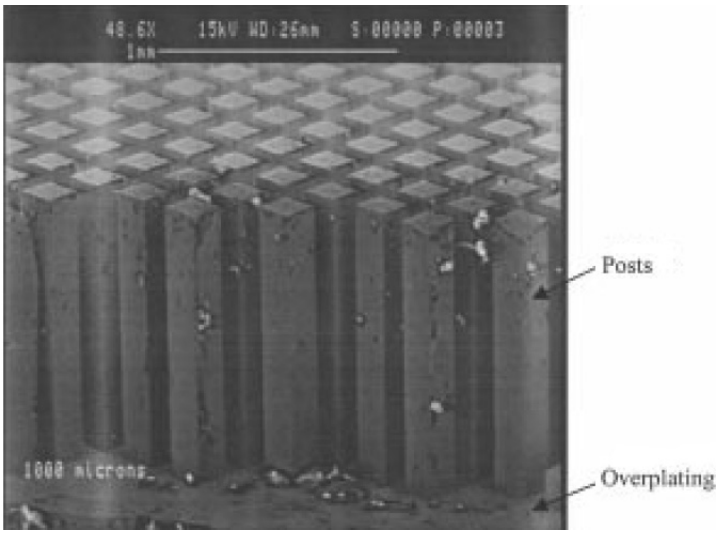

(a) Untested cantilevered microposts

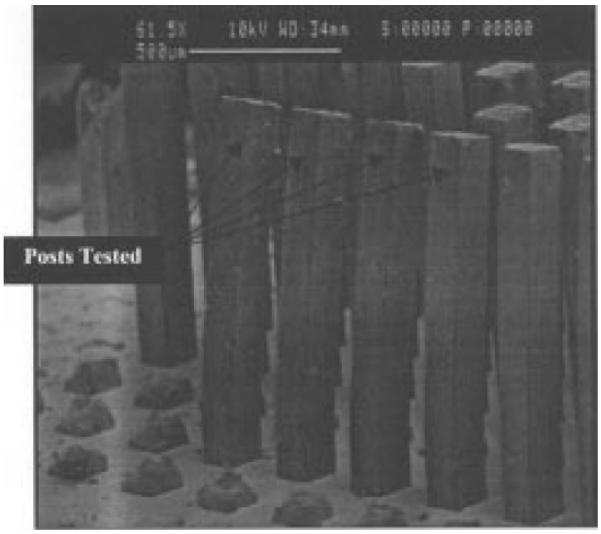

(b) Microposts tested past the failure point

Figure 1.10: Over-electroplated 1 mm tall LIGA nickel cantilevered posts (reproduced from [46]).

Table 1.1 lists experimental Young's modulus values, test type, and electroplating thicknesses for thick samples electroplated from a nickel sulfamate bath. Young's modulus values range from 125 - 231 GPa, but show a general trend of being below the bulk value of 207 GPa. The average of the values reported is 179 GPa. The values reported for copper samples include 120 GPa in [34] and 133 GPa in [44]. For nickel-iron samples, in [35], a value of 115 GPa is given for 50%Ni - 50%Fe and in [38], a value of 155 GPa is given for 72%Ni - 28%Fe. To the author's knowledge, no experimental data has been reported for thick electroplated gold layers.

Table 1.1: Comparison of LIGA nickel properties.

Study	Test Type	Thickness [μm]	Young's Modulus [GPa]
Mazza et al. [35]	Tensile	120 to 200	202
Sharpe et al. [36]	Tensile	200	176
Christenson et al. [37]	Tensile	—	160
Greek and Ericson [38]	Tensile	6	231
Xie et al. [39]	Tensile	200	175
Hemker and Last [40]	Tensile	100 to 200	180
Cho et al. [41]	Tensile	300	163
Lou et al. [42]	Tensile	50	189
Yang et al. [43]	Tensile	270	170
Buchheit et al. [44]	Compression	1600	160
Stephens et al. [46]	Bending	1000	125
Mazza et al. [35]	Vibration	120 to 200	205
Majjad et al. [47]	Vibration	400	195
Bulk [49]	—	—	207

A common conclusion of these works is that the elastic properties of small, electroplated structures may differ from those of bulk structures, and are dependant upon electroplating parameters. Also, the properties of seemingly identically fabricated specimens have a fairly wide range of scatter [46]. Process parameters such as bath types, temperatures, currents, plating areas, etc. potentially affect the properties. These variations highlight the difficulty in measuring material properties using microstructures and the inaccuracies in drawing conclusions based on these findings.

It is very common during development to change certain process parameters based on the structural quality of the resulting devices. An example of this is shown in Figure 1.11 [50]. These are similar nickel devices, but electroplated at two different temperatures. The device in Figure 1.11(a) is electroplated at 24 °C, and the device in Figure 1.11(b) is electroplated at 52 °C. The PMMA surface is shown in focus and the electroplated nickel is beneath it. The improvement in structure quality can be easily observed at lower electroplating temperatures. This change in temperature is very likely to affect the mechanical properties of the devices as well. The problem lies in the fact that there is no simple method to determine how the mechanical properties have changed between these sets of process parameters. This mechanical property data would be extremely useful when doing a redesign or a new design based on an already developed process sequence.

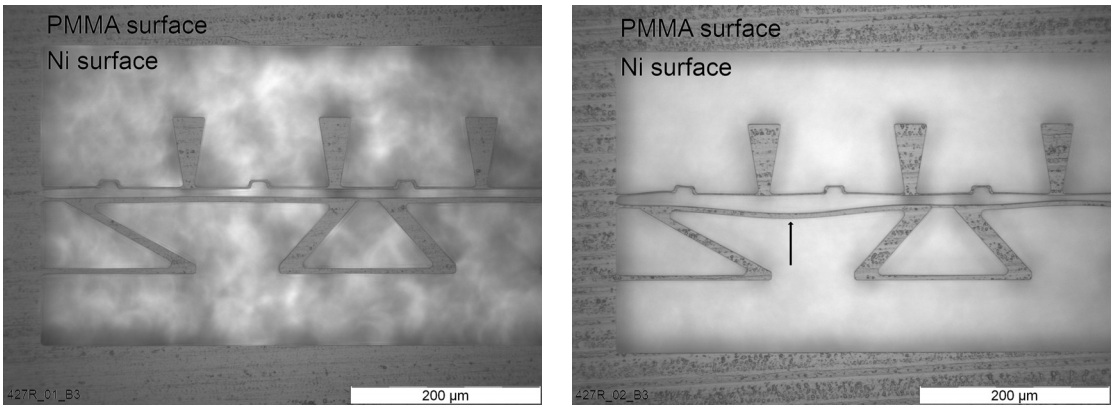

(a) Sample electroplated at 24 °C (b) Sample electroplated at 52 °C

Figure 1.11: Effects of electroplating temperature on sample quality [50].

What is required is a simple, accurate, and relatively quick method to determine the mechanical properties of thick electroplated layers. A standard set of structures is needed that can be easily tested and accurately determine the most relevant mechanical property parameters. This would make it possible for use between various institutes so that the results could be compared. These structures could reside on a standard mask or added to a new mask along with other functional devices. Since the standards would go through the same process as the functional structures, an accurate assessment of the material properties in the functional devices could be made.

1.7 Author's Background Work

A set of electrostatically actuated LIGA-MEMS variable capacitors was designed, simulated, fabricated and partially tested [19]. These three plate, pull-away, variable capacitors were fabricated in nickel to an electroplated height of approximately 100 µm. The static performance of a single capacitor was tested, but the structure was not actuatable due to the incomplete release of the beams, therefore the tuning characteristics of the device could not be determined. The structure tested is shown in Figure 1.12(a). This set of structures had severe deformations present in all devices except the largest, making them unusable. Even the large structures have minor deformations as can be seen in Figure 1.12(a). An example

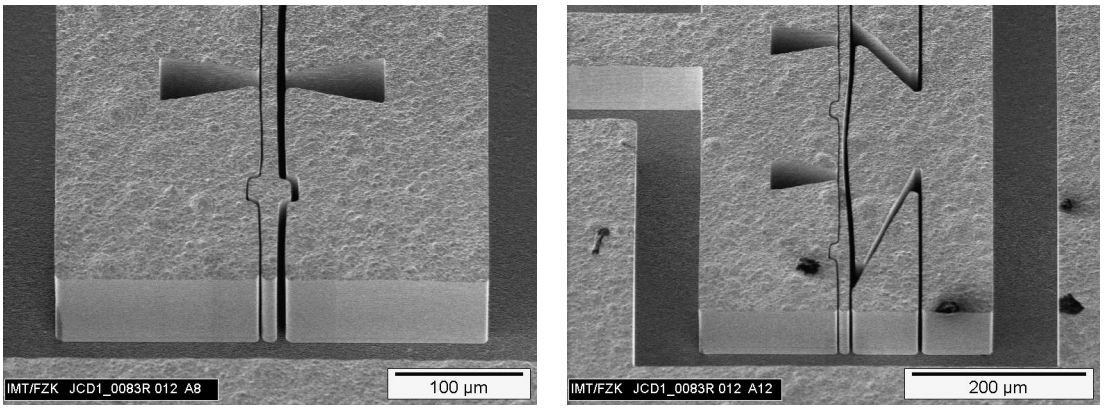

(a) SEM of capacitor f10 (b) SEM of capacitor c10

Figure 1.12: Examples of previously fabricated capacitors [19].

of a device with significant deformations is presented in Figure 1.12(b). Some devices were lost during X-ray lithography due to resist breaking and loss of resist adhesion. Additional devices were deformed during the electroplating process, which can be attributed to resist swelling, thermal expansion and evacuation effects. The only devices without deformations were the devices with periodic widening of the beam and triangular voids in the actuator and capacitance electrodes.

1.8 Objectives

The purpose of this thesis is to design, simulate and fabricate high quality, variable capacitors using the LIGA process that can be used at frequencies up to and including X-band (8 - 12 GHz). This includes investigating processing improvements as well as device characterization to improve the functionality and performance of the structures. To the authors knowledge, these are the only moving microwave MEMS devices that utilize the fabrication strengths of the LIGA process, as previous and current RF LIGA-MEMS research has concentrated on static structures. The specific objectives of this research are:

1. Fully realize the LIGA-MEMS pull-away style variable capacitors. This includes the ability to actuate and test the tuning characteristics of the devices, which was not possible in [19]. Investigate areas of the fabrication process that can be optimized to eliminate or minimize the deformations that are present in the structures so that smaller designs can be fabricated and tested. Also, investigate other materials that can be utilized to increase the performance of the capacitors.

2. Investigate and implement a technique that can be used to realize LIGA-MEMS variable capacitor structures with a larger tuning range. This includes the design of the structure as well as the simulation, fabrication and testing of the device. Also investigate a method to reduce the actuation voltage required by these high aspect ratio beam structures.

3. Develop a set of test standards that can accurately determine the important mechanical material properties from an arbitrary electroplating process, which will improve the feedback loop between simulation and fabrication.

1.9 Thesis Organization

This thesis is organized into eight chapters. Chapter 2 focuses on electrostatic-structural background and theory, which is the underlying mechanism for the actuation of the devices found in this work. Also included is a discussion and verification of the finite element analysis software ANSYS Multiphysics^{TM}, which is used to analyze this class of problem. A background of high frequency electromagnetics is also presented including a discussion of the electrical material properties used in simulations. A description and verification of the 3-D high frequency electromagnetic simulator Ansoft HFSS^{TM}is given, which is used to simulate the high frequency performance characteristics of the devices.

In Chapter 3, LIGA-MEMS pull-away variable capacitors are presented. This includes device layout, theory of operation, fabrication, simulation and test results.

Chapter 4 is a discussion of some of the design challenges encountered including the stiction phenomena, which causes adjacent surfaces to unintentionally adhere to each other when restoring forces are unable to overcome surface forces.

Chapter 5 is a description of the layout and some of the challenges encountered when fabricating devices based on this layout.

In Chapter 6, LIGA-MEMS leveraged bending variable capacitors are presented with considerably increased tuning range compared to the pull-away variable capacitor designs. Theory, design, fabrication and test results are discussed. Also presented is a method to reduce the pull-in voltage by adjusting the gap shape in electrostatically actuated cantilever and fixed-fixed beams, which can be used in future designs to decrease the required tuning voltage.

In Chapter 7, a test system for determining the important mechanical parameters of thick electroplated metal layers called VM-TEST is presented.

In Chapter 8, the conclusions and contributions from the research are presented along with suggestions for future work.

2. Theory and Software Verification

2.1 Electrostatic-Structural Background

Electrostatic beams and plates are used as actuators in a wide variety of MEMS applications [51]. One application, RF MEMS variable capacitors, was discussed in Chapter 1. The main principle behind their operation is deflection caused by an electrostatic force. In the case of variable capacitors, they are often used as one of the capacitor plates. This plate moves under the application of a bias voltage, which causes a change in capacitance. Electrostatic actuation is not the only actuation mechanism suitable for MEMS variable capacitors. It is definitely the most common, but other mechanisms, such as thermal actuation, see limited application as was shown in Chapter 1.

There are four reasons that electrostatic actuation has become so popular in MEMS design. The first reason is that it is inherently easier to design these types of actuators. Other more complicated mechanisms rely on heat transfer or magnetic interaction. The second reason is that they have comparably fast actuation rates. The actuator responds rapidly to a change in the control signal. This is a disadvantage for thermal actuators that generally have longer actuation times due to the time needed for current induced heating [51]. The third and possibly most important reason is that this actuator type has very low, if not zero, power consumption. This is very important from an RF MEMS point of view, where battery lifetime is a very important concern. Unlike most other actuation mechanisms, there is no current flow in an electrostatic actuator. Thermal actuators rely on current induced heating which makes them less power efficient. Thermal actuators can become quite hot, which can be unfavourable from a reliability point of view [52]. The final reason is that electrostatic actuators do not have any special material requirements. This is the major problem with electromagnetic actuators requiring magnetic components not found in most standard manufacturing processes. Taking the above points into account, electrostatic actuation is the main candidate in the field of microwave MEMS systems.

2.2 Electrostatic-Structural Theory

MEMS cantilever and fixed-fixed beam structures are shown in Figure 2.1. These structures exemplify the more typical planar approach and feature thin beams suspended over a ground plane. The ground plane and the beam are electrically isolated and anchored by a dielectric layer, which also determines the gap distance between the beam and the ground plane. The beam is pulled toward the ground plane by applying a bias voltage between the two. This bias voltage creates a separation of charges on the two surfaces, which results in an electrostatic force. As the voltage is increased, the beam bends stably toward the ground plane until a voltage called the "pull-in" voltage is reached. At this point, the beam collapses onto the ground plane.

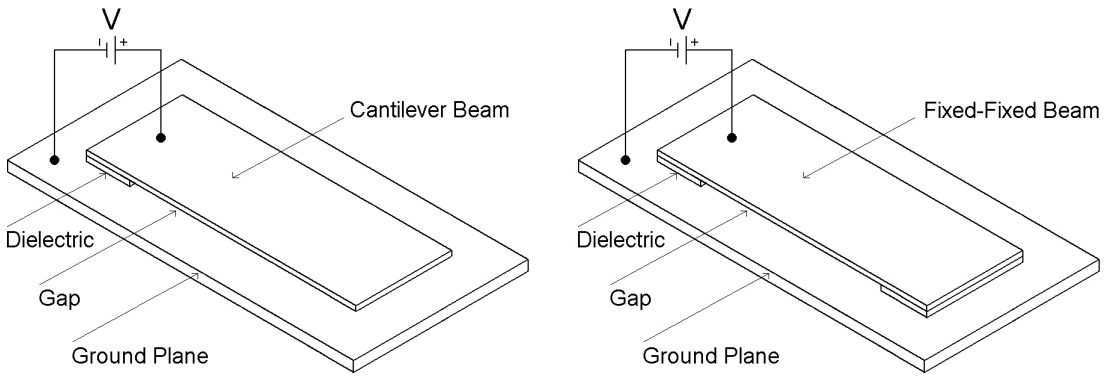

(a) Cantilever Beam (b) Fixed-Fixed Beam

Figure 2.1: Planar beam configurations.

As discussed in Chapter 1, a unique feature of this work is that the beam orientation is perpendicular to the substrate. These vertically oriented (lateral) beams with high aspect ratios, as shown in Figure 2.2, can be fabricated using various micromachining technologies, but are particularly well suited for realization using DXRL and the LIGA process. These vertical beam structures operate under the same principles as the planar structures. Figure 2.2(a) is a high aspect ratio cantilever beam and Figure 2.2(b) is a high aspect ratio fixed-fixed beam. The movable beams of width (w), length (l) and height (h) are connected

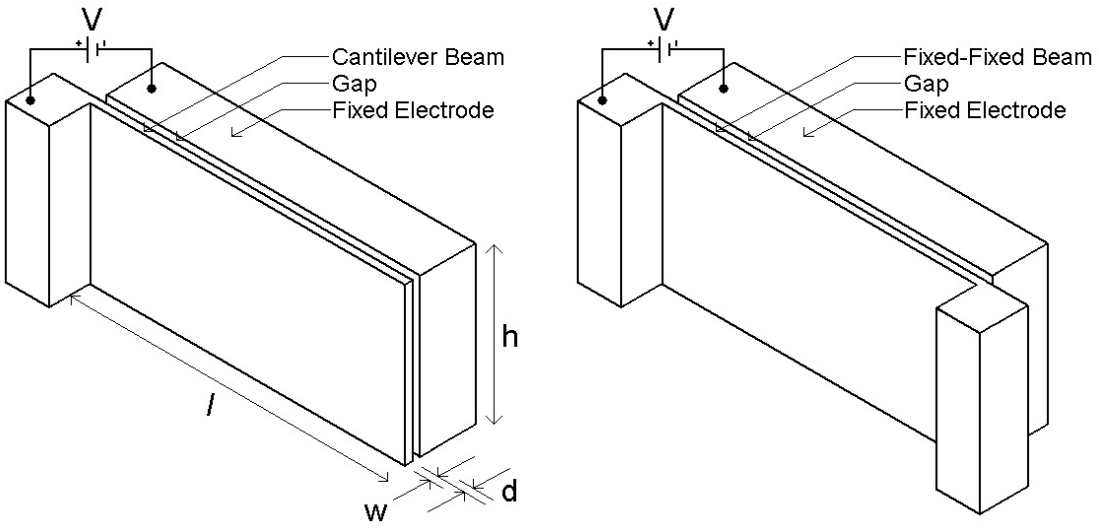

(a) Cantilever Beam (b) Fixed-Fixed Beam

Figure 2.2: Vertical high aspect ratio beam configurations.

to larger stationary pieces. They are also situated next to a fixed electrode, separated by an air gap (d), and are actuated by placing a voltage (V) between the two.

Shown in Figure 2.3 are two-dimensional (2-D) top views of the beam configurations. This figure shows the beam above the fixed electrode, opposite from Figure 2.2, but the operating principles are the same for both configurations. The beam in Figure 2.3(a) is a cantilever beam configuration fixed along one end and Figure 2.3(b) is a fixed-fixed configuration fixed on both opposite ends. A third possibility that is sometimes seen in MEMS devices is called a membrane or diaphragm configuration [53]. In this configuration all four edges of the top plate are fixed and the electrostatic force causes the maximum deflection to occur in the centre of the membrane. This method is not considered because this would require a multilevel LIGA process. It is also not desirable because actuation voltages become quite large.

Electrostatic beams are essentially parallel plate capacitors. Assuming the plates are constrained from moving, as in classic capacitors, fringing is neglected, and the dielectric is

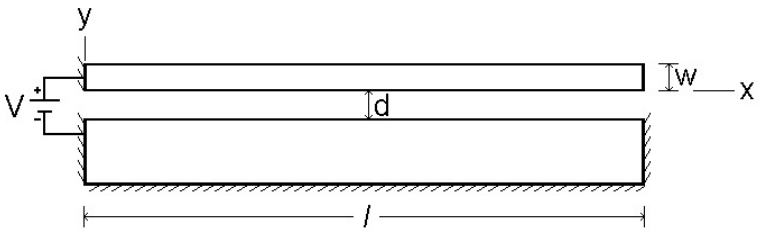

(a) Cantilever Beam

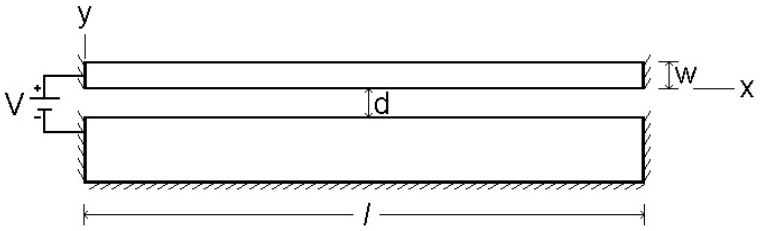

(b) Fixed-Fixed Beam

Figure 2.3: Electrostatic beam configurations (top view).

free space or air with relative permittivity ($\epsilon_r \approx 1$), the capacitance is given by

$$C = \frac{\epsilon_o A}{d}, \tag{2.1}$$

where ϵ_o is the permittivity of free space, A is the area of the plates, and d is the separation between the plates. If a voltage (V) is applied between the capacitor plates, the potential energy of the capacitor (U) is

$$U = \frac{1}{2} C V^2. \tag{2.2}$$

This potential energy is the energy required to prevent the oppositely charged parallel plates from collapsing into each other as a result of the Coulomb force of attraction (F) between point charges [7], given by

$$F = \frac{1}{4\pi\epsilon_o} \frac{q_T q_B}{d^2}, \tag{2.3}$$

where q_T and q_B are the equal but opposite point charges on the top and bottom plates respectively. This force may also be expressed as the negative of the gradient in the potential

energy between the parallel plates

$$F = -\nabla U. \tag{2.4}$$

Substituting Equation 2.1 into Equation 2.2 gives

$$U = \frac{\epsilon_o A V^2}{2d}. \tag{2.5}$$

If Equation 2.5 is now substituted into Equation 2.4, the result is

$$F = \frac{\epsilon_o A V^2}{2d^2}. \tag{2.6}$$

This force is the force on either plate that is trying to pull the plates together as a result of the Coulomb force of attraction due to the separation of charges. An increase in area will cause a linear increase in force, an increase in voltage will cause a quadratic increase in force and an increase in separation distance will cause a quadratic decrease in force.

If one of the plates is configured such that it is free to move when the above force is applied, then the initial gap will decrease as the applied voltage is increased. This is shown in Figure 2.4 for the two configurations mentioned previously. As the voltage is increased, the force increases, which decreases the air gap, further increasing the force. In the case of the cantilever beam, Figure 2.4(a), the force causes a maximum deflection at the tip of the cantilever. In Figure 2.4(b), the fixed-fixed beam has a maximum deflection in the middle of the beam.

For a given voltage, the deflection of the beam can be determined by solving an elastic beam equation [53, 54]. This equation balances the electrostatic force of attraction with the mechanical restoring force. Equations 2.7 and 2.8 [53, 54] are the governing 2-D differential equations for cantilever beams and fixed-fixed beams respectively. These equations assume that the beams are situated above an infinite ground plane, as in Figure 2.1. These equations are shown in Chapter 7 to be also valid for non-infinite ground plane configurations, as in Figure 2.2, with a difference of less that 1% for tall beams with small gaps. These equations have been modified from the versions given in [53, 54] to represent the vertical rather than

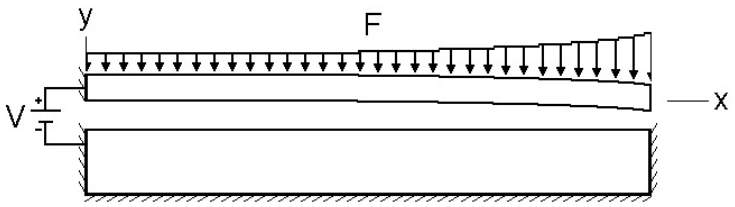

(a) Cantilever Beam

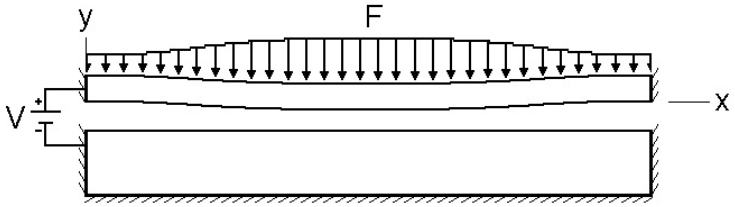

(b) Fixed-Fixed Beam

Figure 2.4: Electrostatic beam configurations during actuation.

planar orientation of the beams.

The left-hand side of the equations represents the mechanical restoring force and comes from well-known Euler-Bernoulli beam and plate theory [55]. The additional term in Equation 2.8, for the fixed-fixed beam configuration, accounts for residual stress effects in the beam and is the force from the residual stress. The right-hand side of the equations is the electrostatic force per unit length with a fringing field correction, which is represented by the factor in parenthesis.

$$\tilde{E}I\frac{d^4d}{dx^4} = -\frac{\epsilon_o V^2 h}{2d^2}\left(1 + 0.65\frac{d}{h}\right) \tag{2.7}$$

$$\tilde{E}I\frac{d^4d}{dx^4} - \tilde{\sigma}hw\frac{d^2d}{dx^2} = -\frac{\epsilon_o V^2 h}{2d^2}\left(1 + 0.65\frac{d}{h}\right) \tag{2.8}$$

The moment of inertia (I) is given by $(1/12)hw^3$, where w is the width of the beam, h is the height of the beam, $d = d(x)$ is the air gap, ν is Poisson's ratio, σ_0 is the residual stress and V is the voltage. From [56], for short beams ($h < 5w$), the effective modulus $\tilde{E}$, is equal to Young's modulus, E, and the effective residual stress, $\tilde{\sigma}$, is equal to the residual

stress, σ_0. For tall beams, ($h \geq 5w$), the effective modulus becomes the plate modulus, $E/(1-\nu^2)$, and the effective residual stress becomes $\sigma_0(1-\nu)$ [53,54]. All beams featured in this work are considered tall. These equations can be solved using a finite difference method, as was done in [53, 54], which is suitable for simple structure geometries such as these. For more complicated structures, finite element analysis using a software package is likely more efficient.

Solving Equations 2.7 and 2.8 can result in a stable or unstable solution depending on the value of the applied voltage. As the voltage is increased, the beam deflects towards the bottom plate. Stable solutions are possible until the beam deflection is approximately 40% of the original gap. If the voltage is increased any further instability occurs and the beam deflects the remaining distance. This is known as pull-in, and the voltage it occurs at is the pull-in voltage V_{PI}. As the beam bends downward, the electrostatic forces become increasingly concentrated in the portion of the beam experiencing the maximum deflection. This is the tip for the cantilever beam and the centre for the fixed-fixed beam, as shown in Figure 2.4. At a particular voltage, this concentrated load causes the beam position to become unstable and it undergoes a spontaneous deflection the rest of the way [57].

By solving for beams of various sizes using a finite difference method, a database of pull-in voltages was created, which was used to develop expressions for pull-in voltages [53, 54]. Simplified pull-in voltage equations for cantilever and fixed-fixed beams are given in Equations 2.9 and 2.10 respectively, with variables modified from [53, 54] to represent the vertical rather than planar orientation of the beams. These equations assume no residual stress is present in the beams and the air gap is much smaller than the beam height ($d << h$), which is normally the case for tall LIGA structures. In addition, the equations are only valid in the small deflection regime (linear elastic mechanics) which is valid for $d/w \leq 1$ [58]. The general case including residual stress is given in [53,54]. From these equations we can see that an increase in elastic modulus, beam width, or air gap will increase the pull-in voltage, while an increase in beam length will decrease the pull-in voltage. For a given set of geometries, a fixed-fixed beam will have a pull-in voltage that is 6.5 times larger than a cantilever beam that is fixed on only one end.

$$V_{\mathrm{PI}_{\mathrm{cantilever}}} \approx 0.529 \sqrt{\frac{\tilde{E} w^3 d^3}{\epsilon_0 l^4 \left(1 + 0.42 \frac{d}{h}\right)}} \tag{2.9}$$

$$V_{\mathrm{PI}_{\mathrm{fixed-fixed}}} \approx 3.444 \sqrt{\frac{\tilde{E} w^3 d^3}{\epsilon_0 l^4 \left(1 + 0.42 \frac{d}{h}\right)}} \tag{2.10}$$

In [59, 60] the authors have developed pull-in voltage equations for both cantilever and fixed-fixed beams using a VLSI on-chip interconnect capacitance model. The author claims the accuracy of these equations is better when compared to other published models including the equations described above. The beam equations, with variables adapted from [59, 60] to represent vertical structures, are given in (2.11) (cantilever) and (2.12) (fixed-fixed). Here residual stress is included and there is no limitation to small deflections. These equations apply to all structures encountered in this work. For cases with extreme fringing fields or gaps much larger than beam width, the general equations are given in [59, 60].

$$V_{\mathrm{PI}_{\mathrm{cantilever}}} \approx \sqrt{\frac{2\tilde{E} w^3 d}{8.37 \epsilon_0 l^4 \left(\frac{5}{6d^2} + \frac{0.19}{d^{1.25} h^{0.75}} + \frac{0.19}{d^{1.25} l^{0.75}} + \frac{0.4 w^{0.5}}{d^{1.5} h}\right)}} \tag{2.11}$$

$$V_{\mathrm{PI}_{\mathrm{fixed-fixed}}} \approx \sqrt{\frac{\left\{9.35 \left[\frac{\tilde{\sigma} w}{l^2}\right] + 32.36 \left[\frac{\tilde{E} w^3}{l^4}\right]\right\} \frac{d}{3} + 24.35 \left[\frac{\tilde{E} w}{l^4}\right] \left(\frac{d}{3}\right)^3}{1.09 \epsilon_0 \left(\frac{5}{6d^2} + \frac{0.19}{d^{1.25} h^{0.75}} + \frac{0.4 w^{0.5}}{d^{1.5} h}\right)}} \tag{2.12}$$

If the MEMS variable capacitor operating frequency is the same as the mechanical resonance frequency, then the variable capacitor is capable of introducing unwanted distortion at that frequency. The first mechanical resonance frequency f_{R} of a cantilever beam for bending oscillations is given in Equation 2.13. For a fixed-fixed beam the equation is given in 2.14 [61].

In the above equations μ is the mass per unit length of the beam. For typical RF MEMS variable capacitor designs, the mechanical resonant frequencies are normally at 10-100 kHz. Since the operating frequencies are at least 10,000 times the mechanical bandwidth, these devices are unlikely to produce a significant amount of harmonic content [22]. This implies

the RF signals will not affect the movement of the beam.

$$f_{\mathrm{R}_{\mathrm{cantilever}}} = \frac{3.52}{2\pi}\sqrt{\frac{\tilde{E}I}{\mu l^4}} \tag{2.13}$$

$$f_{\mathrm{R}_{\mathrm{fixed-fixed}}} = \frac{22.37}{2\pi}\sqrt{\frac{\tilde{E}I}{\mu l^4}} \tag{2.14}$$

2.3 Finite Element Analysis using ANSYS

2.3.1 Motivation

MEMS devices typically fall into one of four categories [62]. The category of MEMS device to be analyzed determines what features the analysis tools require and how complex the model needs to be. Class 1 MEMS devices have no movement. Examples include micromachined static inductors and microcontainers found in MEMS fluidics devices. Strictly, these devices are not MEMS devices since they do not move, but they are micromachined and are often labeled as MEMS devices. Class 2 MEMS have movement but no contact. Examples of these types of devices are capacitors that operate in the region before pull-in, and certain thermal actuators. They can be modeled without the existence of contact surfaces, which makes analysis simpler. Class 3 MEMS have movement with contact, but no shear between surfaces. Typical devices that fall into this category are microwave MEMS switches, and capacitors that operate in the region after pull-in. These devices require contact surfaces in their models and are more complex than the previous classes. Class 4 MEMS devices require the most complex models. They have movement with contact and rubbing. An example is microgears found in gear driven MEMS systems. These devices require models that account for contact and friction. MEMS variable capacitors typically fall into classes 2 or 3 depending on their mode of operation. Therefore an analysis tool that can handle these classes of problems is required for this work.

The most accurate method to analyze coupled electrostatic-structural problems is to use full 3-D finite element (FE) simulations [63]. These solutions produce greater accuracy, but are computationally expensive. In most cases a 2-D approximation of the problem is

sufficiently accurate. A 2-D approximation can only be applied if the model has constant features in one dimension. For vertical beams fabricated using LIGA, the beams must have a constant height and have features that do not vary with height. By analyzing beams with a range of geometries, it was found that the difference between the pull-in voltages from 2-D and 3-D simulations was no larger than 1.5% [53, 54]. For this research this level of error is acceptable and therefore 2-D finite element analysis is used when possible.

There are multiple FE simulators available that are capable of performing coupled electrostatic-structural simulations. Examples include CoventorWare™ [64], ANSYS Multiphysics™ [65], COMSOL Multiphysics™ [66] and MSC Nastran™ [67]. CoventorWare uses a coupled simulator called CoSolve-EM that was developed at the M.I.T. Microsystems Technology Laboratory. CoSolve-EM is the original coupled domain solver with published results appearing in 1995 [68]. It was created by coupling structural (ABAQUS) and electrostatic (FASTCAP) solvers that were already available. ANSYS uses a macro called ESSOLV (electrostatic structural solver) that allows the coupling of existing separate structural and electrostatic solvers. This was first implemented in ANSYS 5.6, which was released in 1999.

ANSYS was chosen since it was readily available and is a proven and popular tool for analyzing coupled physics domain FE problems. Its validity for solving these types of problems will be investigated in the following sections. In addition to electrostatic-structural analysis, the capacitors also require full 3-D high frequency electromagnetic (EM) analysis. Both ANSYS Multiphysics and COMSOL Multiphysics have high frequency EM analysis capabilities, but another commercially available software package (Ansoft HFSS™ [69], now ANSYS HFSS™ [70]) was chosen for this analysis due to its availability and performance. A description and verification of this software is also presented in the following sections. The theory of the finite element method (FEM), is not the focus of this research and therefore will not be discussed in detail. A description of the method is presented in [71, 72]. For this research commercially available software packages are used and assumed valid after a verification test is performed.

2.3.2 Description

ANSYS is a FE software package that can solve problems requiring the analysis of multiple physics domains. In the case of electrostatically actuated MEMS beams, the two physics domains in question are the electrostatic domain and the structural domain. In order to solve a coupled electrostatic-structural problem using ANSYS and the ESSOLV macro, the following steps must be performed:

1. create model geometry
2. mesh the model
3. apply structural constraints and write the structural physics file
4. apply electrostatic constraints and write the electrostatics physics file
5. invoke ESSOLV macro to solve the structure
6. invoke CMATRIX macro to determine capacitance of the displaced structures

The first step is to draw the model. This includes all conductors as well as an air box that surrounds the conductors. All structural and electrostatic objects are meshed with elements. Typically, the only areas that are not meshed are non-movable conductors. Following this, structural constraints are applied. This involves constraining certain areas of the structure from moving. One end of the beam is constrained for a cantilever and both ends in the case of a fixed-fixed beam. The structural elements and constraints are then written to a structural physics file. The next step is to apply electrostatic constraints. This involves applying voltages to conductors. The electrostatic elements and constraints are then written to an electrostatic physics file. The ESSOLV macro is then called to solve the coupled physics problem. This macro automates a sequential solution process. It first solves the electrostatics problem. The forces from the electrostatics problem are then applied to the structural model. The structural problem is then solved. The electrostatic mesh is then adjusted to comply with the structural solution. The macro then checks for convergence. If convergence is not met, the process repeats. Convergence of the coupled problem can be controlled via

the difference in the maximum displacement and/or the difference in electrostatic energy between iterations. Following convergence the CMATRIX macro can be used to determine the capacitance between any number of conductors in the system. CMATRIX computes the capacitance by analyzing the geometry of electrostatic (dielectric) elements.

2.3.3 Verification

To verify the accuracy of the ANSYS finite element simulation platform, ANSYS models were created and compared to the results presented by Osterberg [53,54] and Chowdhury [59,60]. The results of the comparison will be presented as well as a detailed description of the simulation of a single beam type. In [53, 54], multiple simulations using a 2-D distributed model were performed and a database of pull-in voltages was created. These results were used to create closed-form equations for the pull-in voltage of cantilever beams, fixed-fixed beams and diaphragms. Simplified versions of the equations, which neglect residual stress, are given in (2.9) (cantilever) and 2.10 (fixed-fixed). In addition, for a select subset of structures, the 2-D results were compared to full 3-D finite element simulations using CoSolve-EM. ANSYS simulation results are compared to this subset in order to verify the accuracy of the simulator. In [59, 60], closed form equations for the pull-in voltages of cantilever and fixed-fixed beams were created using a VLSI on-chip interconnect capacitance model given in (2.11) (cantilever) and 2.12 (fixed-fixed). The author claims the accuracy of these equations is better when compared to other published models. ANSYS results are also compared to the results predicted by these closed-form equations.

To implement this in ANSYS, the beam is created and meshed with 0.25 μm rectangular structural elements of type 82 with the plane strain option turned on since the beam is tall and the plate modulus should be used. The beam and stationary electrode are surrounded by an air box which is meshed with 0.25 μm rectangular electrostatic elements of type 121. The stationary electrode does not receive mesh since the interior of it is neither a structural element nor an electrostatic element. The material properties are defined and the beam is fixed on one end for cantilevers or both ends for fixed-fixed beams. Nonlinear geometry effects are turned on using the NLGEOM command. The beam has the input voltage applied to it and the stationary electrode has 0 V applied to it. Structural and electrostatic physics

files are written and a coupled analysis is performed using the ESSOLV macro. The results of the comparison are given in Table 2.1. This data set includes both cantilever and fixed-fixed beams of varying lengths (l), Poisson's ratio (ν), and residual stress (σ_0). For all beams $E = 169$ GPa, $\nu = 0.06$ (unless specified), $h = 50$ μm, $w = 3$ μm and $d = 1$ μm. Table 2.1 shows that excellent agreement exists between all methods to better than 1% on average. The CoSolve-EM full 3-D results are expected to be the most accurate and 2-D ANSYS results agree to within 0.76% on average. This verifies that 2-D simulations are sufficiently accurate for this work. In 2-D simulations, the fringing effects at the ends of the beam are included, but the effects along the length of the beam are neglected. This makes 2-D FEM analysis valid for tall beams where fringing fields are negligible. For short beams, 3-D FEM analysis would likely be more accurate.

The 2-D cross-section model for the $l = 150$ μm cantilever beam case is shown in Figure 2.5. The cross-section is assumed uniform for the entire height of the structure. The top narrow rectangle is the cantilever beam and the rectangle below the beam is the fixed electrode. Both conductors are enclosed in an air box.

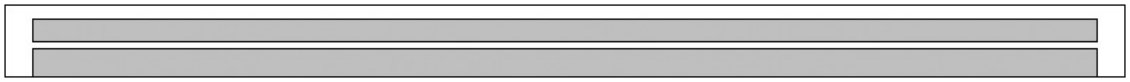

Figure 2.5: Verification model geometry for the $l = 150$ μm cantilever beam case.

In electrostatic analyses, unlike structural analyses, electric fields are typically unbounded. To accurately calculate the electric field, the effect of the open domain must be included in the electrostatic model. The model cannot extend to infinity and therefore must be limited in practice, while still maintaining solution accuracy. ANSYS has two methods, for 2-D models, that can be used to model the effect of open field decay. The first method is to extend the free space region, and the second is to use infinite elements. Extending the free space region is efficient in small gap models with minimal fringing. Infinite elements are efficient for large gap models with significant fringing. For 2-D models, the fringing occurs at the ends of the parallel plates. ANSYS defines a small gap to be 20 times smaller than

Table 2.1: Comparison of ANSYS 2-D finite element analysis with previously published results.

Beam Description	V_{PI} [V] 3-D FEM [53]	V_{PI} [V] closed-form [53]	V_{PI} [V] closed-form [59, 60]	V_{PI} [V] 2-D FEM ANSYS	$\Delta\%$ between 2-D FEM and 3-D FEM [53]	$\Delta\%$ between 2-D FEM and closed-form [53]	$\Delta\%$ between 2-D FEM and closed-form [59, 60]
Cantilever Beams							
$l = 100$ μm	38.2	37.9	37.84	37.85	0.92	0.13	0.03
$l = 100$ μm, $\nu = 0.32$	39.8	39.9	39.86	39.90	0.25	0.00	0.10
$l = 150$ μm	16.9	16.8	16.83	16.85	0.30	0.30	0.12
Cantilever Average					0.49	0.14	0.08
Fixed-Fixed Beams							
$l = 250$ μm, $\sigma_0 = 0$	40.1	39.5	39.60	39.56	1.35	0.15	0.10
$l = 250$ μm, $\sigma_0 = 0$, $\nu = 0.32$	41.2	41.5	41.72	41.70	1.21	0.48	0.05
$l = 250$ μm, $\sigma_0 = 100$ MPa	57.6	56.9	57.40	57.35	0.43	0.79	0.09
$l = 250$ μm, $\sigma_0 = -25$ MPa	33.6	33.7	33.71	33.50	0.30	0.59	0.62
$l = 350$ μm, $\sigma_0 = 0$	20.3	20.2	20.20	20.19	0.54	0.05	0.05
$l = 350$ μm, $\sigma_0 = 100$ MPa	35.8	35.4	35.91	35.71	0.25	0.88	0.56
$l = 350$ μm, $\sigma_0 = -25$ MPa	13.7	13.8	13.71	13.42	2.04	2.75	2.12
Fixed-Fixed Average					0.88	0.81	0.51
Overall Average					0.76	0.61	0.38

the beam length. Since the structures encountered in this work are small gap problems, the method used is to extend the free space region. ANSYS suggests that for small gap models the free space needs to be extended approximately 2 - 4 times the gap size. In the above model the free space region is extended 4 times the gap size (4 μm) on the sides of the beam and 2 times the gap size (2 μm) on the top of the beam. The outer box is given a Neumann boundary condition. This enforces that the electric field is parallel to the outer surface and equipotential lines are normal to the outer surface. The conductors within the outer box are given a Dirichlet boundary condition. This enforces that the electric field is normal to the conductor surface and equipotential lines are parallel to the conductor surface.

An enlarged view of the right side of the cantilever is shown in Figure 2.6(a). The meshed structure is shown in Figure 2.6(b). The cantilever beam is meshed using 2-D, 8-node, structural solid elements. The air region is meshed using 2-D, 8-node electrostatic elements. The elements have nodes at the vertices as well as midside nodes in between the vertices. The size of the elements is specified to be 0.25 μm. ANSYS recommends using gap/2 for a coarse mesh, gap/4 for a medium mesh, and gap/6 for a fine mesh. A medium mesh is used because the results are sufficiently accurate for verification.

The model is solved for a series of input voltages from 0 V until the solution becomes unstable which indicates pull-in. The voltage is applied to the cantilever beam and the bottom fixed plane is grounded. In this model no contact surfaces are specified, therefore the cantilever can pull right through the fixed ground plane. This is not a problem since the simulator cannot find a stable solution unless the voltage is less than the pull-in voltage. If contact is required then contact elements need to be added. The results from a single voltage (16 V) simulation are presented followed by the results from the voltage sweep. This voltage is chosen since it shows large deflection because it is very close to the pull-in voltage of 16.85 V.

Figure 2.7 shows the deflection of the cantilever upon application of a 16 V potential. The upper box shows the geometry of the undeformed cantilever. The deformed cantilever is shown directly below. The displacement of the cantilever tip is 0.30 μm. The deflection of the cantilever is magnified by a factor of 100 in Figure 2.7 so that the shape of the displacement can be easily observed.

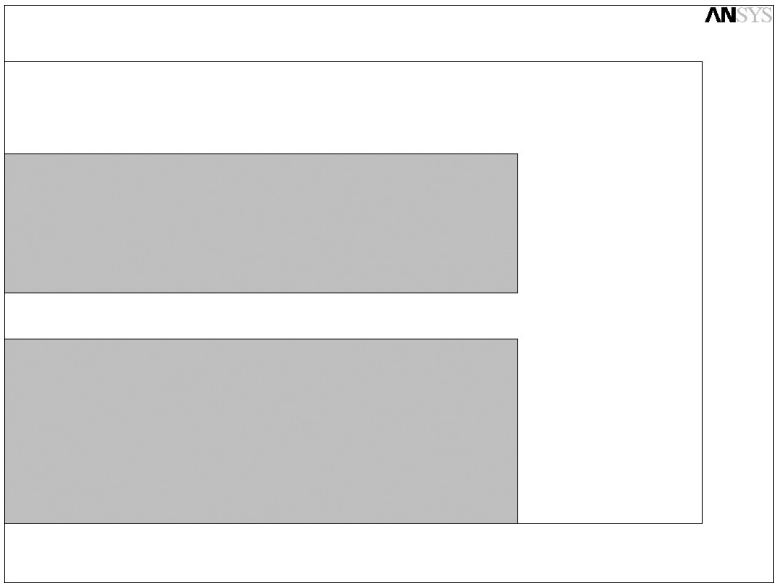

(a) Without mesh

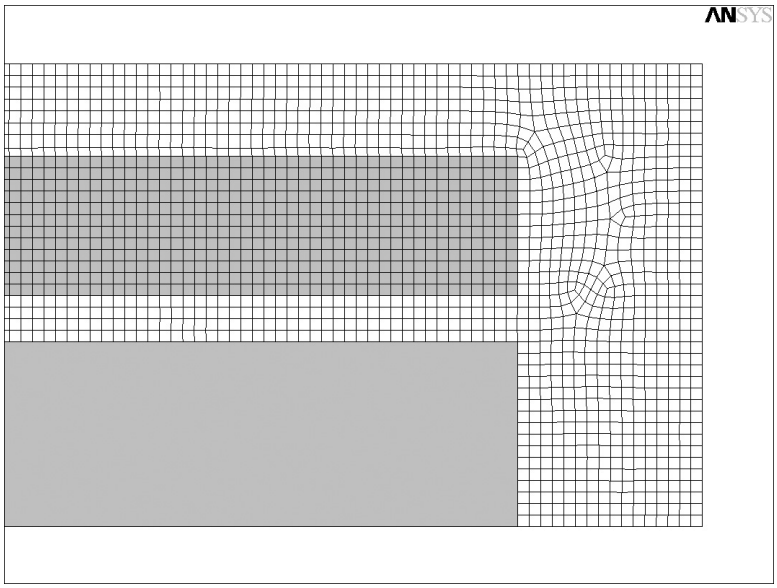

(b) With mesh

Figure 2.6: Enlarged model view of cantilever tip.

Figure 2.8 shows the deflection of the cantilever tip, where the electrostatic mesh has been remeshed to coincide with the deflection of the cantilever. The mesh on the cantilever beam has been omitted for clarity. The number of elements between the plates have been reduced as the gap between the plates has decreased.

Figure 2.7: Cantilever displacement scaled by a factor of 100 with 16 V applied.

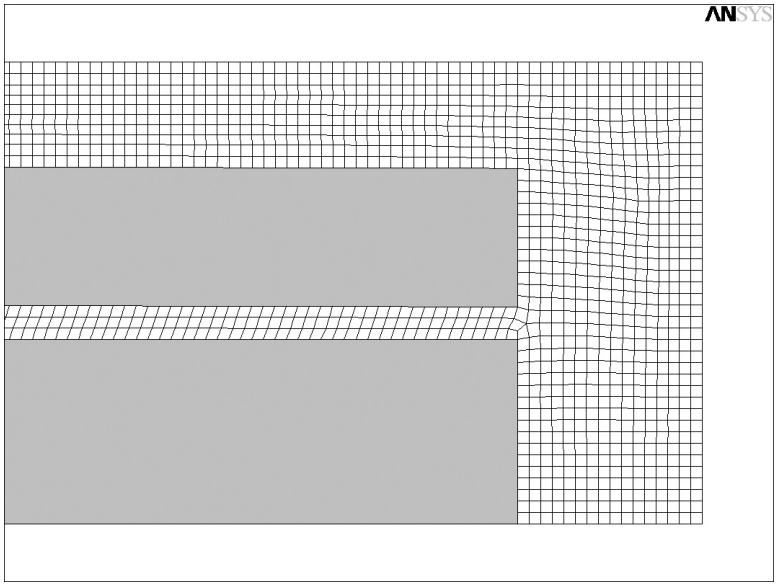

Figure 2.8: Morphed electrostatic mesh at cantilever tip with 16 V applied.

Figure 2.9 shows the voltage contours surrounding the deformed cantilever. The cantilever is at a potential of 16 V as expected and the fixed ground plane is at a potential of 0 V. Figure 2.10(a) is a contour plot of the electric field intensity. As expected the magnitude is the largest in the gap with fringing fields having increasingly smaller magnitudes. The magnitude of the field in the gap is in the range of 20.148 to 23.026 V/μm, which is consistent for a 0.70 μm gap with 16 V across it. Figure 2.10(b) is a vector plot of the electric field. The vector magnitude is a linear function. The direction of the field is from the top plate (16 V) to the bottom plate (0 V).

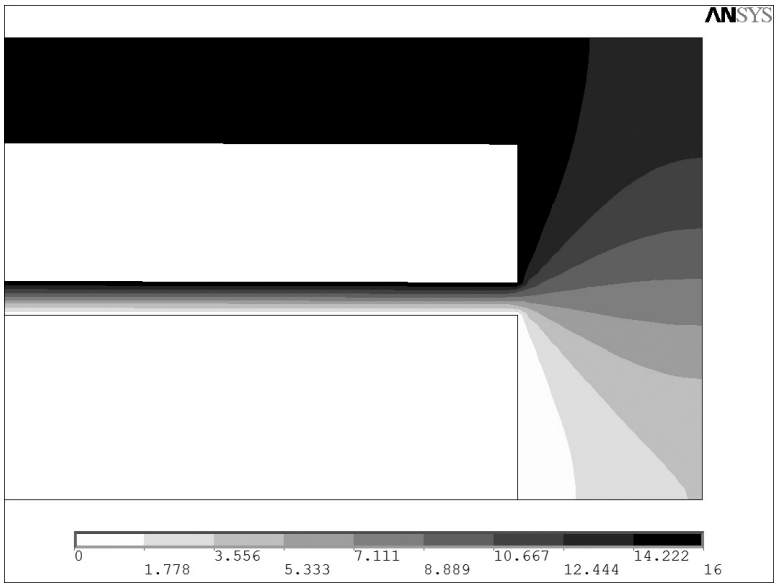

Figure 2.9: Voltage contours with 16 V applied.

The voltage is varied from 0 V until the pull-in voltage is obtained. At pull-in the solution becomes unstable and the simulator cannot produce a solution. Figure 2.11 is a plot of the tip deflection versus the applied voltage and Figure 2.12 is a plot of the capacitance versus the applied voltage. The capacitance values given by ANSYS have units of pF/μm. This is equivalent to having a beam with a height of 1 μm, therefore they have been multiplied by 50 for a beam with a 50 μm height as required here.

The maximum deflection of the cantilever tip was 0.4383 μm at a voltage of 16.85 V. This corresponds to an approximately 44% tip deflection of the original gap. The simulator found a solution for the beam with an applied voltage of 16.85 V, but could not converge on a solution with an applied voltage of 16.86 V. This indicates that the pull-in voltage of the beam is between these two voltages. The initial capacitance of the beam is 0.06725 pF with an applied voltage of 0 V. The maximum capacitance is 0.08363 pF with a voltage of 16.85 V. This corresponds to a capacitance ratio of 1.24:1. Using the simple parallel plate capacitor formula, Equation 2.1, the capacitance for this structure is 0.06641 pF. This is very close (1.27% difference) to the initial capacitance calculated by the simulator. The theoretical value is slightly smaller because it neglects fringing, which the simulator takes into account.

However, the values are close enough to give confidence in the validity of the simulator. The pull-in voltage for this case was found to be within 0.3% of 3-D FEM simulations as well as both closed-form equations as shown in Table 2.1.

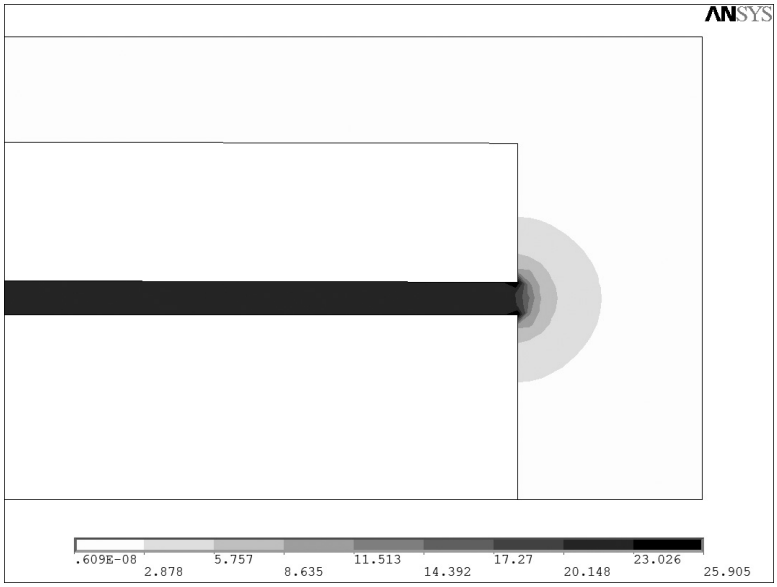

(a) Intensity contours

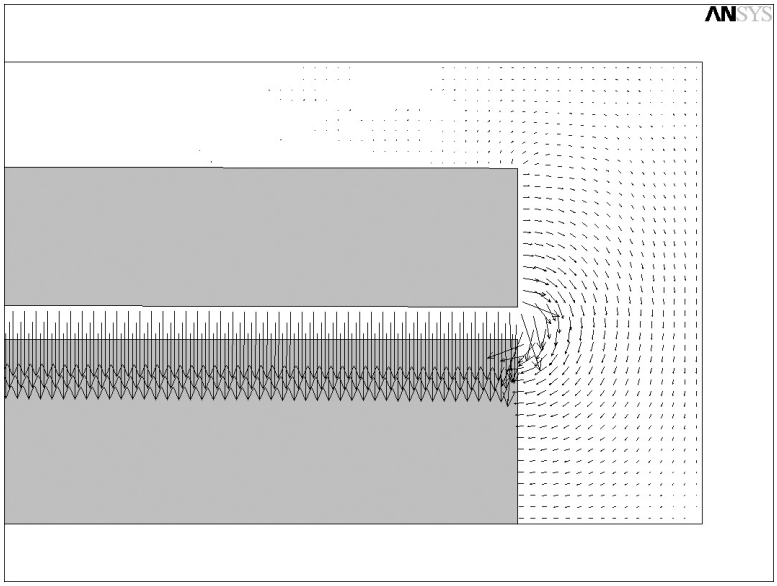

(b) Vector plot

Figure 2.10: Electric field with 16 V applied.

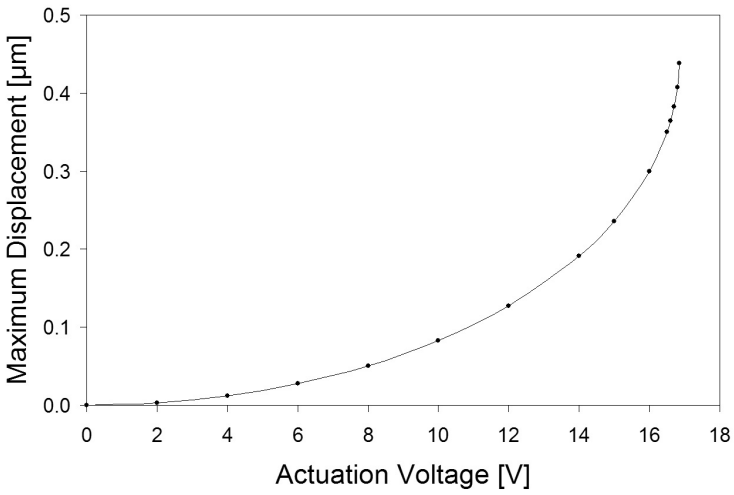

Figure 2.11: Tip deflection of verification beam.

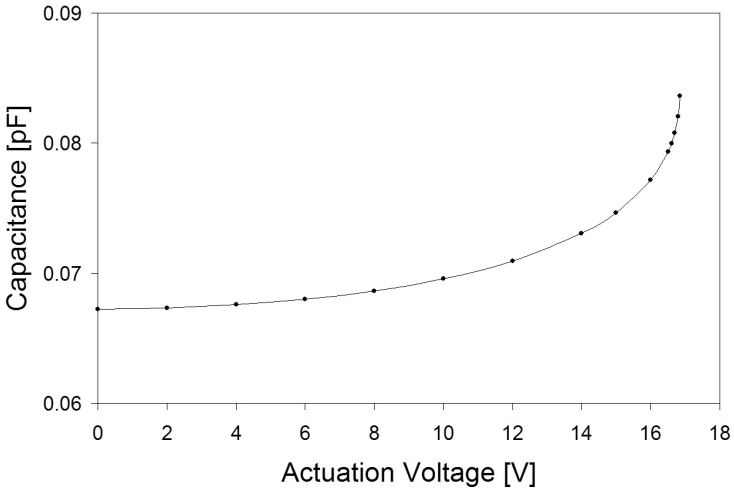

Figure 2.12: Capacitance of verification beam.

2.4 High Frequency Electromagnetic Background

A method to obtain an estimate of the important electrical parameters of the capacitors is required. The electromagnetic performance is governed by Maxwell's equations [73], a set of partial differential equations relating the electric and magnetic fields to each other and to the electric charges and currents. These equations are often very difficult to directly solve

for all but the simplest of structure geometries. For most practical problems, the solution to Maxwell's equations requires an approximate solution using a rigorous approach such as the finite element method. A finite element simulator is able to solve a problem with arbitrary geometry by discretizing it. It then represents Maxwell's equations as a set of matrix equations and solves them using conventional numerical methods, usually requiring a computer.

2.4.1 Material Properties

In order to perform accurate simulations, accurate material properties are required. Materials encountered in this work include nickel, gold, titanium, alumina, quartz glass and air. For metals, the electrical properties usually required include conductivity (σ) and relative permeability (μ_r) and for dielectrics the properties are relative permittivity (ϵ_r) and dielectric loss tangent (tan δ). The exact electrical properties of fabricated materials is unknown since they vary significantly between different processes especially in the case of micro-electroplated metals.

Accurate material properties seem to exist for all materials required in this work with the exception of the relative permeability of nickel at high frequencies. In [74], the author states that RF engineers are currently faced with the problem that there is insufficient data available to undertake simulation designs with a high level of confidence at microwave frequencies. Also stated is that surprisingly, very little has been reported on the magnetic permeability of nickel. A survey of relative permeability values for nickel in [74] lists values from 1 to 600 with the author stating that no information is given as to whether the values represent DC values, or how the nickel was deposited or its level of purity. Also mentioned is that the relative permeability is expected to decrease to unity as frequency increases and the largest variation occurs in the 0.1 to 10 GHz range.

A collection of measured data [75], shown in Figure 2.13, verifies this trend of decreasing permeability with an increase in frequency. The plot shows a relative permeability of approximately 10 at 1 GHz, which decreases to approximately 1 at 10 GHz. Significant variation exists within the data, but the general trend is followed. Relative permeability values for nickel used in this work are listed in Table 2.2. These values were measured by Hodsman et

al. [76] and were chosen since they are similar to the frequencies of interest in this work.

The electrical properties of all materials used in simulations in this work are listed in Table 2.3. The conductivity of nickel was obtained from [79] (1.266 $\times$ 10^7 S/m). This value was chosen since it is a measured value from an electroplated sulfamate bath for LIGA applications, similar to the nickel electroplated structures described here. This value agrees well with conductivity values listed for deposits from sulfamate baths [80] (average of 1.19 $\times$ 10^7 S/m). These are slightly lower than the values found for bulk nickel in the Ansoft HFSS materials database (1.45 $\times$ 10^7 S/m), or found in the literature (1.46 $\times$ 10^7 S/m) [49]. For gold the default values from the HFSS materials library were used. This conductivity (4.1 $\times$ 10^7 S/m), agrees well with the range of values listed for electroplated gold [80] (average of 4.11 $\times$ 10^7 S/m), as well as data for bulk gold [49] (4.26 $\times$ 10^7 S/m). For titanium a conductivity value of 2.38 $\times$ 10^6 S/m [49] was used, which is slightly larger than the value found in the HFSS material properties database (1.82 $\times$ 10^6 S/m). The dielectric properties of 96% alumina, quartz glass and air are listed in Table 2.3. Default values were

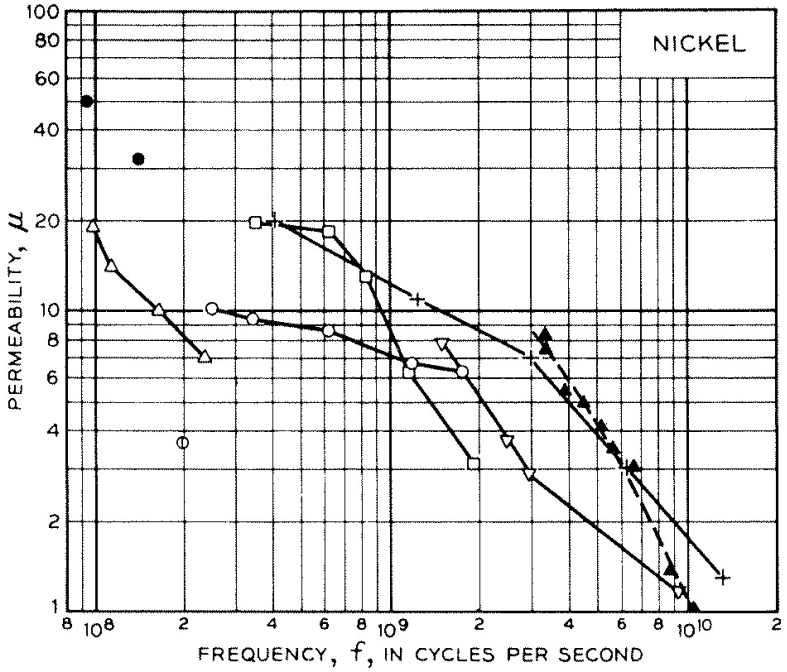

Figure 2.13: Nickel permeability as a function of frequency (reproduced from [75]) (+ Arkadiew [77], $\triangledown$ Simon [78], $\blacktriangle$ Hodsman et al. [76]).

used except in the quartz glass case where a relative permittivity of 3.81 was used instead of the 3.78 listed in the HFSS database. This was done so that the material properties would match for a verification of the HFSS simulator in a later section.

Table 2.2: Measured relative permeability of nickel [76].

Frequency [GHz]	Relative Permeability (μ_r)
dc	17.0
3.356	8.30
3.374	7.50
3.956	5.60
4.545	5.00
5.062	4.10
5.564	3.40
6.522	3.00
8.772	1.50
9.615	1.03
10.084	1.00

Table 2.3: Electrical material properties used in simulations. Values are from Ansoft HFSS materials database unless specified.

Material	Relative Permittivity (ϵ_r)	Relative Permeability (μ_r)	Bulk Conductivity (σ) [S/m]	Dielectric Loss Tangent $\tan\delta$
Nickel	1	Table 2.2 [76]	1.266×10^7 [79]	0
Gold	1	0.9996	4.1×10^7	0
Titanium	1	1.00018	2.38×10^6 [49]	0
Alumina 96%	9.4	1	0	0.006
Quartz Glass	3.81 [13]	1	0	0
Air	1.0006	1.0000004	0	0

2.5 Finite Element Analysis using Ansoft HFSS

2.5.1 Motivation

A method to obtain an estimate of the important electrical parameters of the capacitors is required. In order to perform this, the system must be capable of determining the impedance parameters of an arbitrary passive 3-D structure at microwave frequencies. This can be accomplished using the software package Ansoft HFSS (High Frequency Structure Simulator) [69]. HFSS uses the finite element method (FEM) to solve Maxwell's equations. The solved wave equation is derived from the differential form of Maxwell's equations. The primary advantage of the FEM for solving partial differential equations lies in the ability of the basic building blocks used to discretize the model to conform to arbitrary geometry [81].

With this software package, the first step is to draw the structure, then material characteristics for each object are specified. Next excitation sources (ports) are defined, which allow energy into and out of the structure. Following this, boundary conditions are specified as necessary. The solution frequency is specified and HFSS then generates the necessary field solutions and associated port characteristics and S-parameters (scattering parameters). The

problem can be solved at one specific frequency or at several frequencies within a range if a frequency sweep is specified. The S-parameters obtained using HFSS can be converted to Z-parameters (impedance parameters) which can then be used to determine the important electrical parameters of the capacitor. Parameters of interest include the nominal capacitance, associated inductance or electrical self-resonance and equivalent series resistance or Q-factor. The nominal capacitance at low frequencies can also be used to determine the parasitic capacitance.

Like ANSYS described in the previous chapter, HFSS is a finite element solver, but with EM field boundary conditions. The software divides the geometric model into a large number of tetrahedra, where a single tetrahedron is a four-sided pyramid. This collection of tetrahedra is referred to as the finite element mesh. This discretization method allows HFSS to represent Maxwell's equations as a set of matrix equations and solve the equations using traditional numerical methods.

Structures with high aspect ratios, such as the devices presented here, require a dense mesh for high accuracy, which results in large computation times. This is complicated by the meshing of metals at high frequencies, since most of the current flow in a conductor occurs in a thin region near the surface of the conductor. The skin depth (δ_s) is defined as the depth at which the amplitude of the fields in the conductor decay to an amount $1/e$ or 36.8% of the value at the surface [73] and is shown in Equation 2.15. In this equation, σ is the conductivity, ω is the angular frequency ($2\pi f$) and μ is the permeability ($\mu_0\mu_r$). Since the skin depth is very small at high frequencies, a large mesh results if the interior of the conductors is to be accurately meshed. The element size required for accurate modeling would be a fraction of the skin depth and these elements would have to extend a few skin depths into the metal. This leads to prohibitive computation times. For this reason HFSS, by default, only solves inside objects with a bulk conductivity less than 10^5 S/m. Since most metals have a conductivity greater than this, they are solved using a surface impedance approximation, which is based on the skin depth.

$$\delta_s = \sqrt{\frac{2}{\sigma\omega\mu}} \tag{2.15}$$

2.5.2 Description

HFSS represents the model with a mesh of tetrahedra. At the vertex of each tetrahedron, HFSS stores the components of the field that are tangential to the three edges of the tetrahedron. By representing field quantities in this way, the system can transform Maxwell's Equations into matrix equations that are solved using traditional numerical methods.

HFSS is capable of multiple solution types. The type of interest for this application is a driven solution. This solution type is used for calculating the S-parameters of passive, high frequency structures such as microstrips, waveguides, and transmission lines, which are driven by a source. The source used to excite the model is called a wave port. Wave ports represent places in the geometry through which excitation signals enter and leave the structure. They are used when modeling strip lines and other waveguide structures.

HFSS starts the analysis by creating an initial mesh of the ports, the metal surfaces, and the non-metal objects. HFSS generates a solution by exciting each wave port individually. Port 1 is excited by a signal of one watt, and the other ports are set to zero watts. After a solution is generated, port 2 is set to one watt, and the other ports to zero watts and so forth. The ports must be perfectly matched to the characteristic impedance of the waveguide that each port faces in order not to allow reflection of power back into the model. This is realized by HFSS automatically by assuming that each port is virtually connected to a semi-infinitely long waveguide having the same cross-section and material properties as the part of the model exposed to the port. The two-dimensional field distributions generated for each port are used as the boundary conditions for the three-dimensional model [82].

The generalized S-matrix is then computed from the amount of reflection and transmission that occurs. This is the first step in an adaptive analysis process. HFSS automatically refines the mesh in regions where the error is high, which increases the solution's precision. A new set of generalized S-parameters is computed based on the refined mesh. This process is repeated until the change in the magnitude of the S-parameters between iterations is smaller than a user specified value.

A generalized S-matrix describes what fraction of power associated with a given field excitation is transmitted or reflected at each port. The following discussion is valid for a

network with an arbitrary number of ports n. Z_{0n} is the (real) characteristic impedance of the nth port, and V_n^+ and V_n^-, respectively, represent the incident and reflected voltage waves at port n. The wave amplitudes are defined as

$$a_n = \frac{V_n^+}{\sqrt{Z_{0n}}} \tag{2.16}$$

$$b_n = \frac{V_n^-}{\sqrt{Z_{0n}}} \tag{2.17}$$

where a_n represents a normalized incident wave at the nth port, and b_n represents a normalized reflected wave from that port [73]. The generalized scattering matrix is defined as

$$[b] = [S][a] \tag{2.18}$$

where the i, jth element is given by

$$S_{ij} = \left.\frac{b_i}{a_j}\right|_{a_k=0 \text{ for } k\neq j} \tag{2.19}$$

Therefore S_{ij} is the S-parameter describing how much of the excitation signal at port j is reflected back or transmitted to port i. For example, S_{21} is used to compute the amount of power from the port 1 excitation field that is transmitted to port 2. The phase of S_{21} specifies the phase shift that occurs as the signal travels from port 1 to port 2.

HFSS determines the characteristic impedance (Z_0) of each port from the values of power (P) and current (I) [82].

$$Z_{0n} = \frac{P}{I \cdot I} \tag{2.20}$$

The power and current are computed directly from the simulated fields. The power passing through a port is equal to [82]

$$P = \oint_s E \times H ds \tag{2.21}$$

where the surface integral is over the surface of the port. The current is computed by

applying Ampere's law to a path around the port [82]

$$I = \oint_{l} H \bullet dl \tag{2.22}$$

While the net current computed in this way will be near zero, the current of interest is that flowing into the structure, I^+, or that flowing out of the structure, I^-. In integrating around the port, HFSS keeps a running total of the contributions to each and uses the average of the two in the computation of impedances [82].

The Z-parameters of the structure can be computed from the generalized S-parameters and the characteristic impedances of the ports. The Z-matrix is calculated from the S-matrix as follows [82]

$$Z = \sqrt{Z_0}(I - S)^{-1}(I + S)\sqrt{Z_0} \tag{2.23}$$

where S is the $n \times n$ generalized S-matrix, I is an $n \times n$ identity matrix, and Z_0 is a diagonal matrix having the characteristic impedance (Z_{0n}) of each port as a diagonal value. These impedance parameters will be used to determine the important electrical parameters of the capacitor.

2.5.3 Verification

To verify the simulation platform, the transmission characteristics of a LIGA microstrip stepped impedance low-pass filter are determined using HFSS. This filter was simulated, fabricated, and tested by Willke and Gearhart [13]. The results obtained using HFSS are compared to the results obtained in [13] to give confidence in the validity of the HFSS simulator for tall LIGA structures.

The layout of the stepped impedance filter [13], is shown in Figure 2.14, the relevant dimensions are shown in Table 2.4 and a scanning electron microscope (SEM) micrograph of the fabricated filter is shown in Figure 2.15.

The microstrip filter was constructed using 220 μm thick electroplated nickel, on top of a 420 μm thick quartz substrate ($\epsilon_r = 3.81$ at 30 GHz). The ground plane was 0.75 μm thick gold. The filter was designed to have a 0.5 dB Chebyshev response. From presented simu-

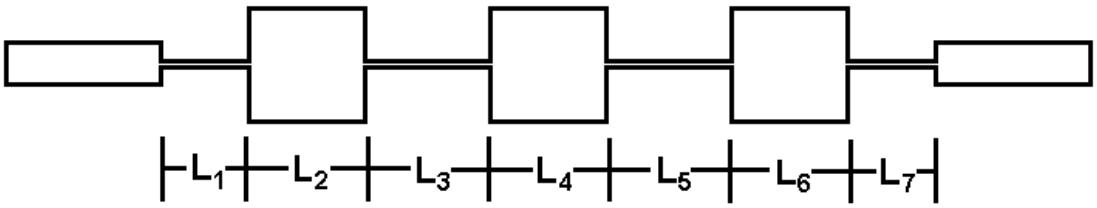

Figure 2.14: Verification model layout (reproduced from [13]).

Table 2.4: Verification model dimensions [13].

Section	Width	Z_0	Length
1 and 7	100 μm	106 Ω	$L_1 = L_7 = 2.52$ mm
2 and 6	1.5 mm	35 Ω	$L_2 = L_6 = 2.7$ mm
3 and 5	100 μm	106 Ω	$L_3 = L_5 = 3.825$ mm
4	1.5 mm	35 Ω	$L_4 = 2.885$ mm

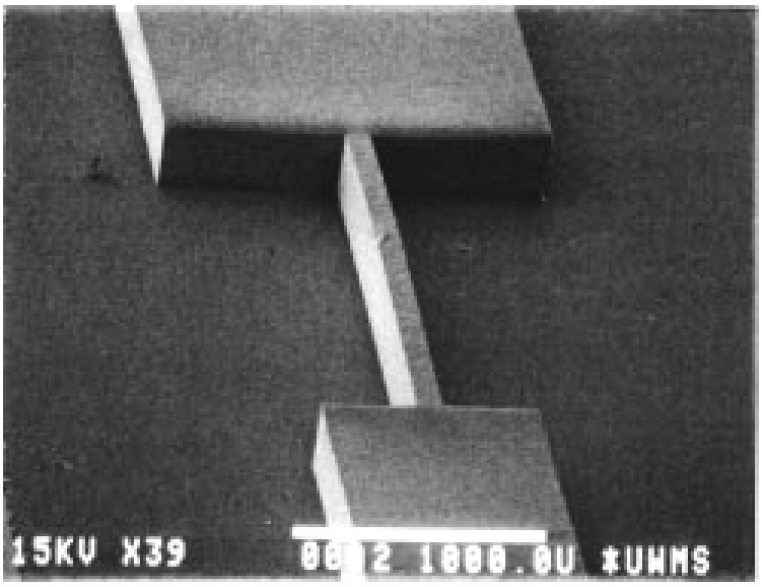

Figure 2.15: SEM micrograph of LIGA microstrip filter (reproduced from [13]).

lation results [13], the filter has a 3 dB cutoff frequency of 9.6 GHz and 20 dB attenuation at 12.2 GHz. The characteristic impedance of the filter sections was determined by Willke and Gearhart using a 2-D finite-difference (FD) analysis of the LIGA microstrip lines. The obtained characteristic impedances were used as input for the simulation of the filter using PUFF [83], which is a subnetwork calculation-based circuit analysis program for laying out and analyzing planar microstrip and stripline circuits. The transmission coefficient simulation and test results obtained by Willke et al. are shown in Figure 2.16. The measured filter response is -3 dB at 9.22 GHz and reaches -20 dB at 11.4 GHz. The difference between simulated and measured results obtained by Willke et al. are 4.8% for the -3 dB point and 7.0% for the -20 dB point.

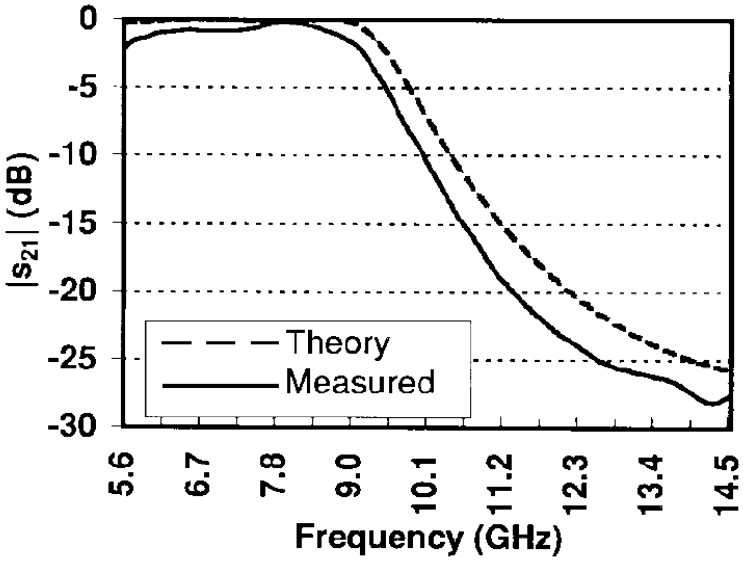

Figure 2.16: Simulation and test results for LIGA microstrip filter (reproduced from [13]).

A full 3-D simulation of the filter was performed using HFSS. The HFSS model is shown in Figure 2.17. Figure 2.17(a) is an overview of all elements in the model including the nickel conductor, quartz glass substrate, surrounding air box and two wave ports. Figure 2.17(b) shows the generated tetrahedra mesh on only the conductor and the substrate. The mesh for the other elements is not shown for clarity. The material properties used in the simulation

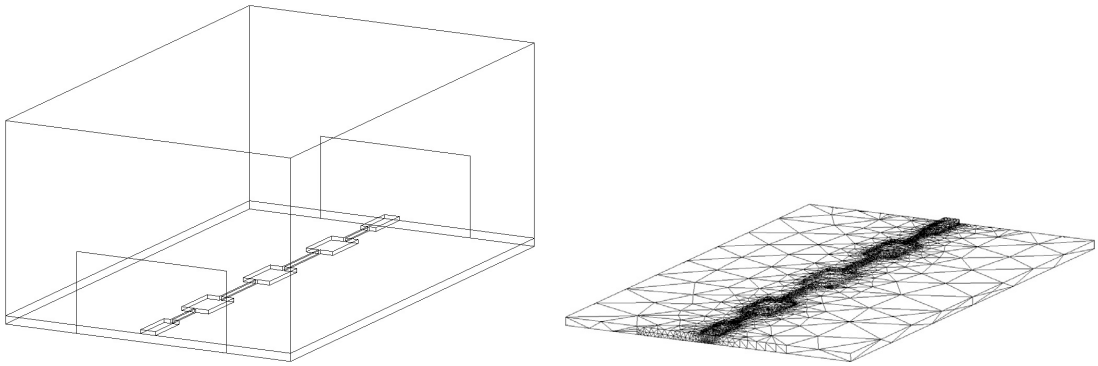

(a) HFSS model (b) Meshed conductor and substrate

Figure 2.17: HFSS simulation model for LIGA microstrip filter.

are listed in Table 2.3. In the model, the nickel conductors were placed on top of the quartz substrate. A large air box extends upwards from the substrate and surrounds the conductors. All outer surfaces of the model interfacing the background are by default assumed perfect E boundaries (tangential component of the electric field is zero), which does not permit any energy to enter or leave. This includes the bottom surface of the substrate which is the ground plane. The ports enclose the nickel conductors and the bottom of the ports touch the ground plane. The size of the ports and air box follows the rules listed in the HFSS documentation [81].

A 15 iteration adaptive solution at 10 GHz was performed, resulting in approximately 33000 tetrahedra. Following this, a discrete frequency sweep from 5 GHz to 15 GHz, in steps of 0.1 GHz, was performed. A top view of the mesh on the conductor and substrate is shown in Figure 2.18(a). The electric field magnitude in the substrate is shown in Figures 2.18(b) and 2.18(c) at 6 and 14 GHz respectively. From the electric field plots, it can be observed that at 6 GHz there are strong electric field components on all sections of the filter indicating that a large portion of the input signal is being transmitted to the output. At 14 GHz the electric field magnitude is large around the input port (left side), but the signal magnitude at the output (right side) is minimal. The transmission coefficient is shown in Figure 2.19 for the filter using the relative permeability values reported by Hodsman et al. [76] and with a constant value of 600, which is the default value in the HFSS material properties

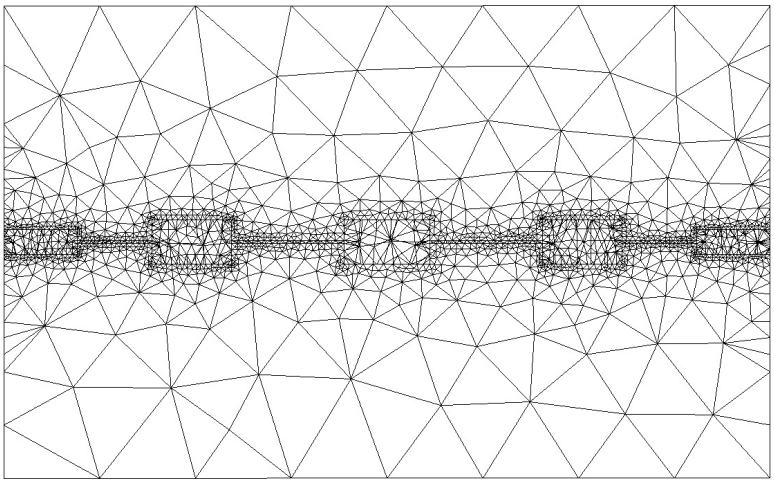

(a) Meshed conductor and substrate (top view)

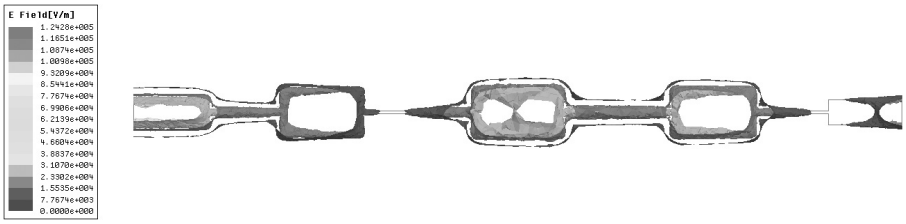

(b) Electric field magnitude in substrate at 6 GHz (bottom view)

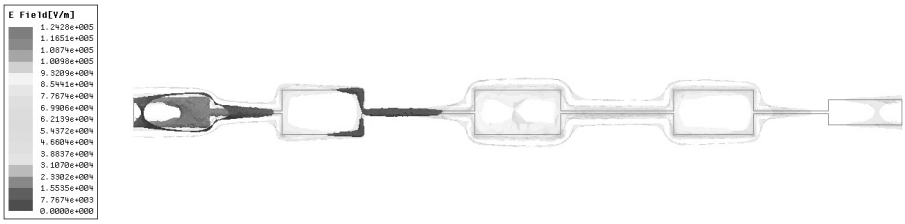

(c) Electric field magnitude in substrate at 14 GHz (bottom view)

Figure 2.18: Finite element mesh and the electric field magnitude in the substrate at 6 GHz and 14 GHz for the HFSS simulation model.

database. The simulated filter response with μ_r from [76] matches well with the simulated and measured results presented in [13]. However the results with $\mu_r = 600$ show that this value of relative permeability is not valid for this range of frequencies.

To test the surface impedance approximation used by HFSS, the filter resistance was approximated as a series of seven hollow rectangles with metal thickness determined by the skin depth (δ_s), which is shown in Equation 2.15. This was compared against the real

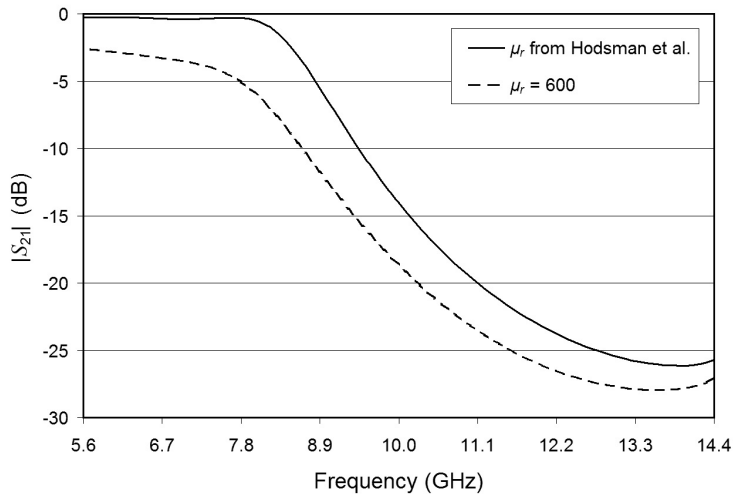

Figure 2.19: HFSS simulation results for LIGA microstrip filter.

component of the impedance parameter Z_{21} obtained from HFSS simulations. At 5 GHz, with μ_r from [76] (Table 2.2), the approximated resistance is 1.82 Ω and the HFSS value is 1.32 Ω. With $\mu_r = 600$, the approximated resistance is 21.52 Ω and the HFSS value is 24.15 Ω. Although crude, this approximation gives confidence in the surface approximation used by HFSS. This is also demonstrated in Figure 2.19 by the downward shift of the transmission curve with an increase in the relative permeability of nickel.

With μ_r from [76], the simulation results show -3 dB at 8.58 GHz and -20 dB at 11.10 GHz. The test results obtained by Willke et al. show -3 dB at 9.22 GHz and -20 dB at 11.4 GHz. This results in a 6.9% difference for the -3 dB point and a 2.6% difference for the -20 dB point. The simulation results obtained using Ansoft HFSS are close enough to give confidence in the validity of the simulator for analyzing tall metal LIGA structures.

It should be noted that in the simulation results discussed here, the effects of the seed layer were neglected for simplicity, as they were in [13]. The actual seed layer was a tri-layer metal film of titanium, copper, titanium sputtered to a thickness of 600 Å/3600 Å/600 Å (0.06 μm/0.36 μm/0.06 μm) [13]. A model with only the copper seed layer was simulated using HFSS for μ_r from [76], which resulted in a slight upward shift (average of 0.07 dB) of the transmission coefficient curve. The default material properties for copper from the HFSS

database were used with $\mu_r = 0.999991$ and $\sigma = 5.8 \times 10^7$ S/m. This resulted in -3 dB at 8.59 GHz and -20 dB at 11.11 GHz, which shows that in this case, the inclusion of the seed layer has a minor effect on the transmission characteristics. A simulation of the actual tri-layer seed layer was attempted, but not successful due to a prohibitively large number of tetrahedra required for an accurate simulation.

3. Pull-away Variable Capacitors

3.1 Theory of Operation and Layout

A simplified 2-D top-view of a three-plate cantilever beam variable capacitor suitable for fabrication using DXRL is shown in Figure 3.1. The capacitor is composed of four structures, an actuator electrode, a capacitance electrode, and two ground structures, configured to facilitate testing with standard ground-signal-ground (GSG) wafer probes. The most unusual feature of this device is the thin vertical cantilever situated between the two electrodes as opposed to traditional planar parallel plate variable capacitor structures which are parallel to the substrate. This implies that the bulk of the electric field is parallel to and largely unaffected by the supporting, and potentially lossy, substrate. The capabilities of DXRL allow tall structures with very small capacitance gaps and almost unlimited control of cantilever and gap geometries. The cantilever is anchored to one ground structure and is the only portion of the device that is released from the substrate and is free to move. The

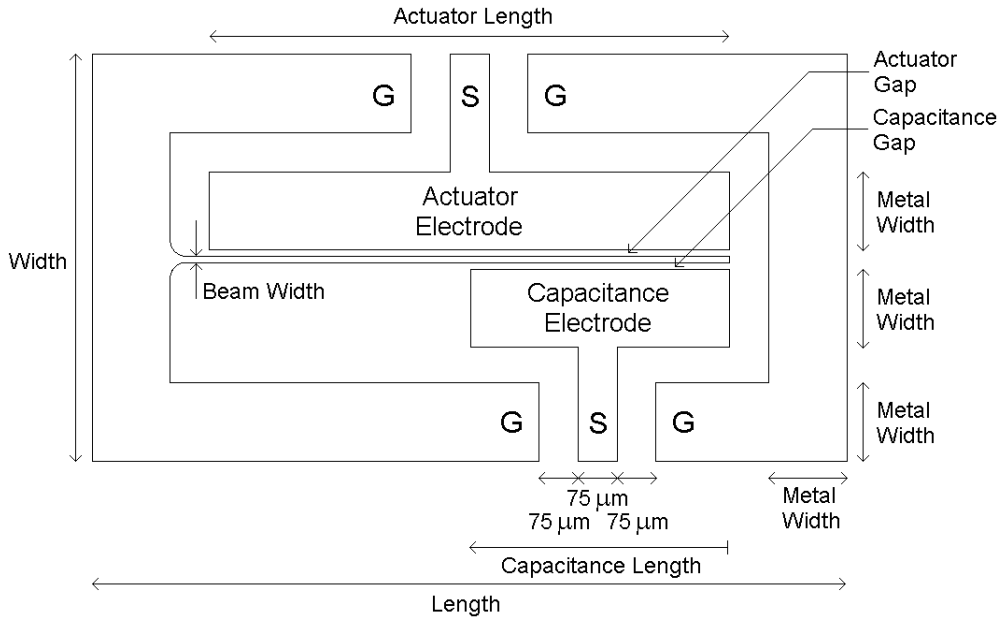

Figure 3.1: Top view of three-plate cantilever beam capacitor.

attachment point between the cantilever and the ground structure is rounded significantly, which was shown to be important in [19].

Applying a DC bias voltage between the actuator electrode and the grounded cantilever causes an electrostatic force between the two, which results in a deflection of the cantilever toward the actuator electrode. This decreases the capacitance between the cantilever and the capacitance electrode. The beam deflects stably until the pull-in voltage where the beam collapses onto the actuation electrode. As shown in [19], this three-plate method can be used to increase the tuning range of the capacitor over a simple two-plate design. This is only valid if the actuator gap is at least 1.24 times larger than the capacitance gap. The tuning range can be made larger by increasing the actuator gap at the expense of an increase in actuation voltage. With the given design, the cantilever could be actuated toward either electrode to further increase the capacitance tuning range, as was done in [22], but in this scenario RF and control signals must be combined.

A picture of the overall mask layout is shown in Figure 3.2. The overall layout size of standard masks used at IMT is approximately 20 mm by 60 mm. This is the size of the outer rectangle in Figure 3.2. The area allotted for the capacitors was approximately 40% of the overall mask, which was shared with another user.

The mask layout includes 60 capacitors with varied sizes and feature geometries. A larger view of all the capacitors is shown in Figure 3.3. The capacitors are composed of 2 identical grids (A - F, a - f) of 6 rows and 10 columns to ensure redundancy for every individual

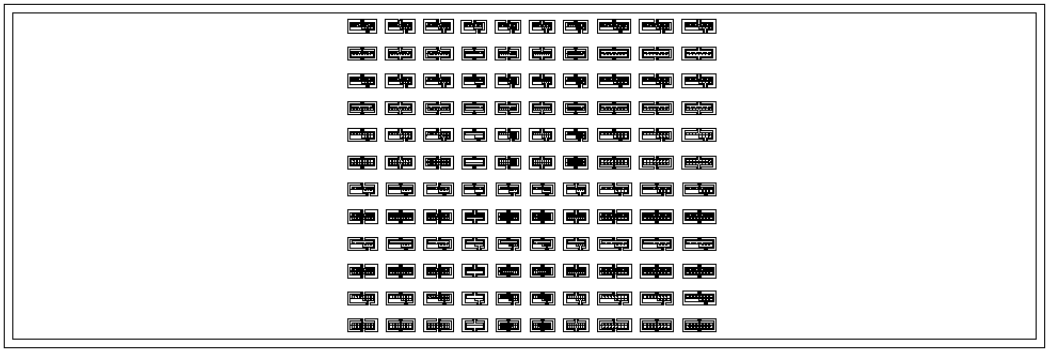

Figure 3.2: Mask layout.

device.

All capacitors were designed with both full and half-length capacitance electrodes, to allow for two different capacitance values. The full electrode designs are in rows B, D, and F and the half electrode designs are in rows A, C, and E. The capacitor pairs (A - B, C - D, and E - F), in the same column, have identical layouts except for capacitance electrode lengths.

Three sizes of capacitors were developed. The smallest capacitors are in columns 4 - 7, columns 1 - 3 contain larger devices, and the largest capacitors are in columns 8 - 10. A summary of specific capacitor dimensions from the layout, is listed in Table 3.1. The labels are consistent with the labels shown in Figure 3.1. The metal width (Figure 3.1) for all devices is 150 μm .

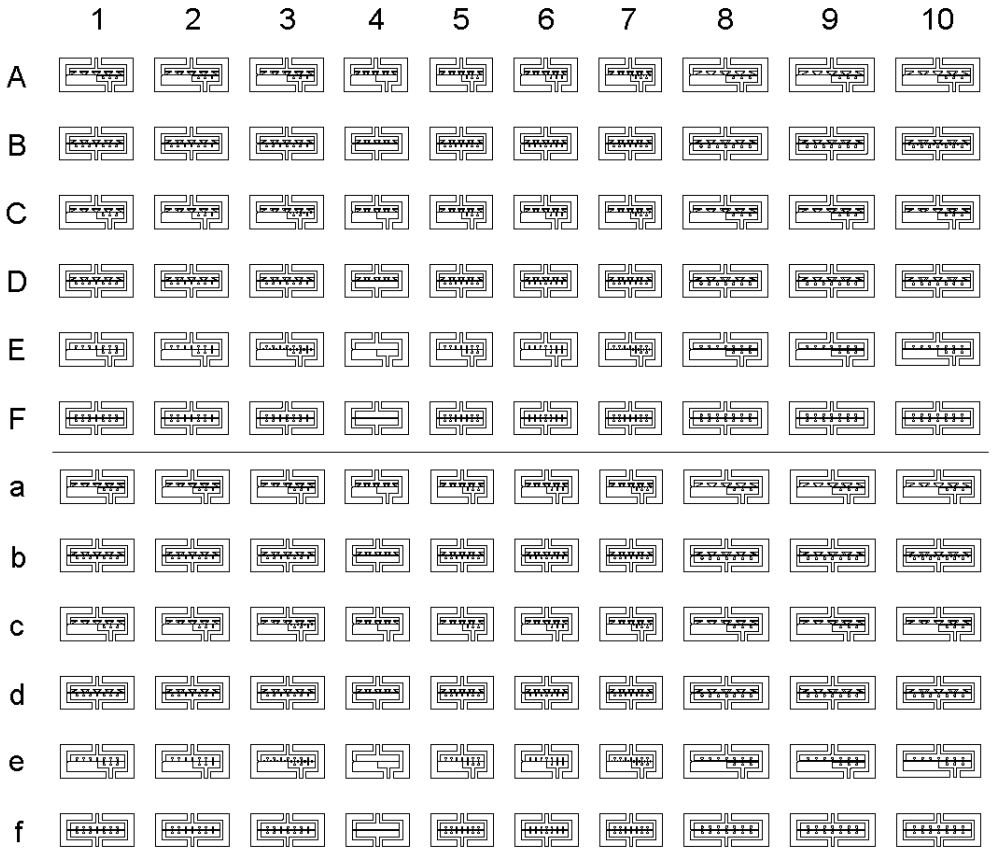

Figure 3.3: Capacitor grid from mask layout.

Table 3.1: Capacitor dimensions from layout.

Columns	1-3	4-7	8-10
Length [μm]	1700	1450	1950
Width [μm]	768.75	765	772.5
Actuator Length [μm]	1250	1000	1500
Beam Width [μm]	7.5	6	9
Actuator Gap Width [μm]	7.5	6	9
Capacitance Gap Width [μm]	3.75	3	4.5

Stoppers limiting the beam deflection were added to some of the capacitors in the layout to ensure no electrical short can occur during actuation. Capacitors in rows E and F have no stoppers. Capacitors in rows A and B have stoppers that are placed far from the beam. Capacitors in rows C and D have stoppers that are placed close to the beam. For the devices with stoppers placed far from the beam, the stopper gap is 2/3 of the actuator gap. For stoppers placed close to the beam, the stopper gap is 1/3 of the actuator gap. The two different stopper gap locations were chosen to test devices with and without hysteresis [19].

The layout and desired structure height requires extremely high aspect ratios (structure height / minimum feature size). This is very challenging for any microfabrication process. In order to improve the probability of successfully fabricated devices as given in Figure 3.1 some modifications were made to the general layout of the capacitors as shown in Figure 3.4 (capacitor E7). Capacitor E7 is a half capacitance electrode design and has no stoppers.

Two changes were made to improve the probability of successful fabrication. The first change is that periodic widening was added to the beam. This takes the form of periodic "bumps" on the beam. This increases the mechanical stability of the long and high, but narrow PMMA/metal walls by raising the geometrical moment of inertia. It also slightly increases the diffusion of developer into the resist. The adjacent electrodes follow the profile of the beam to minimize the effects on the capacitance by maintaining the gap width. The second change is the triangular voids in the actuator and capacitance electrodes (resist relief),

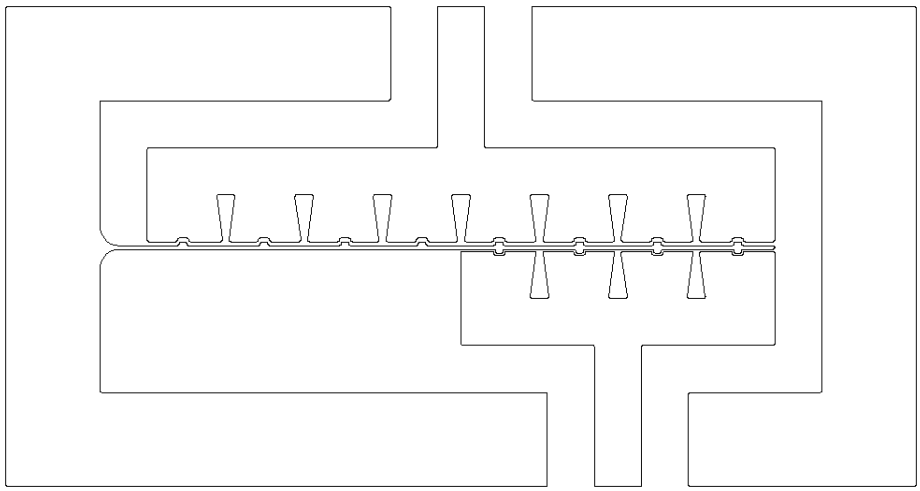

Figure 3.4: Layout of capacitors E7 and e7.

which relates to triangularly supported PMMA walls. This is done for two reasons. First, it will tend to anchor the small gap resist so it is not broken off or deformed during development and electroplating. Second, it will allow the HF acid to get into the small gap while etching the seed layer.

Figure 3.5 is the layout of capacitor C7. This is a half capacitance electrode capacitor with stoppers close to the beam. The stoppers are the large triangles that are embedded within the actuator electrode. These triangles are electrically isolated from the actuator electrode. The triangle tips lie between the beam and the actuator. This prevents the beam from deflecting further than the tips of the triangles.

For the smallest capacitors (columns 4 - 7), column 4 is the originally designed capacitors without resist relief or periodic widening of the beam. Columns 5 and 6 are identical and contain resist relief. Column 7 contains resist relief and periodic widening of the beam. For the next larger capacitors (columns 1 - 3), columns 1 and 2 are identical and contain resist relief. Column 3 contains resist relief and periodic widening of the beam. For the largest capacitors (columns 8 - 10), columns 8 and 9 are identical and contain resist relief. Column 10 contains resist relief and periodic widening of the beam.

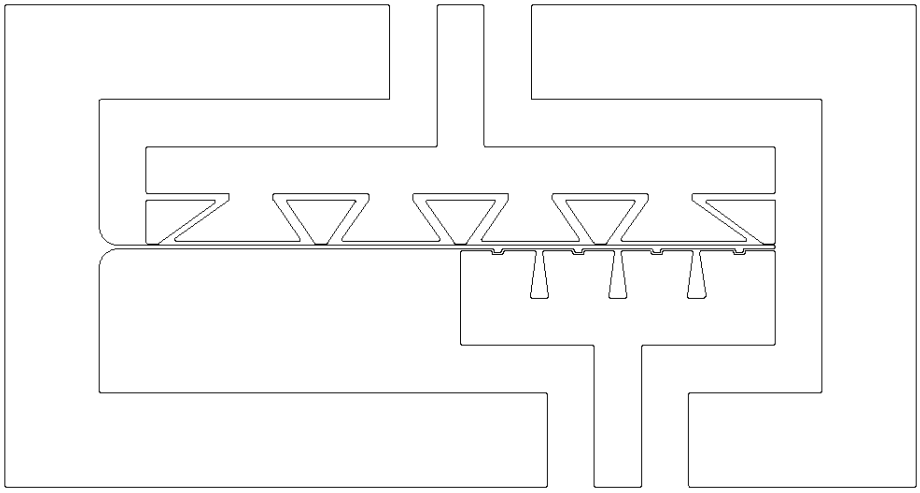

Figure 3.5: Layout of capacitors C7 and c7.

3.2 Fabrication

X-ray exposures were done using the 2.5-GeV electron storage ring ANKA and beamline Litho 2 (mirror angle = 8.65 mrad, $\varepsilon_{\mathrm{cut-off}} = 6.9$ keV) at the Karlsruhe Institute of Technology. PMMA (GS 233) photoresist foils of either 100 or 150 µm thickness were glued on a 1 mm thick alumina wafer coated with a 3 µm thick oxidized titanium (Ti/TiO_x) seed layer. This sample was exposed to X-rays through a titanium membrane (2.7 µm) mask with 20 µm thick gold absorbers. The bottom dose deposition was 3.5 kJ/cm^3. Following irradiation, megasonic-supported development was performed for 150 min in GG developer at room temperature. The Ti/TiO_x coating on the wafer was used as a plating base for either 70 or 100 µm thick nickel or gold electroplating. The structure was then exposed to X-ray flood irradiation, allowing the remaining PMMA to be removed with another step of development. The structure was then descummed in oxygen plasma and wet etched with 5% HF acid for 2 min to remove the seed layer, electrically isolating the capacitor structures. This isotropic etching also selectively released the thin beam, while still providing good adhesion of the larger metal parts. This allows the plating base to function as a time-controlled etch sacrificial layer, releasing the cantilever beam without requiring an additional lithographic process.

Figure 3.6 shows capacitor e4 in 100 μm thick resist. This image is flipped both vertically and horizontally from Figure 3.1 so that the capacitance electrode is in the top left instead of the bottom right. The severe deformation of the thin PMMA walls that are meant to define the capacitance and actuator gaps in the subsequent electroplating step can be clearly seen. These long and thin walls lose adhesion to the substrate during the development process and stick together.

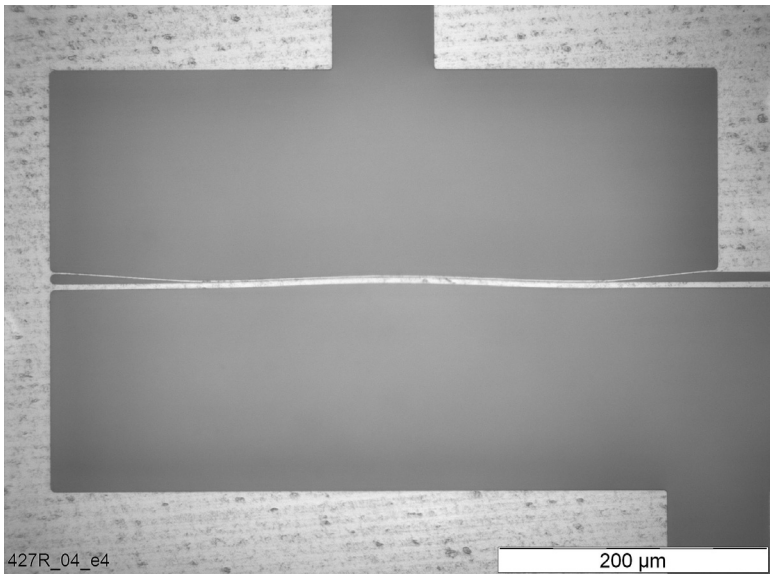

Figure 3.6: Capacitor e4 in 100 μm developed resist.

Only structures that were equipped with both periodic widening of the beam and triangular electrode voids for resist relief, as shown in Figure 3.4, were processed safely. Figure 3.7 [50] shows how these auxiliary structures help to strengthen the thin PMMA walls so that deformations are avoided during the fabrication process. Figure 3.7(a) is capacitor A2 and Figure 3.7(b) is capacitor A3 in 150 μm PMMA. The difference between the two devices is that A3 has periodic beam widening as highlighted by the arrow in Figure 3.7(b). These two figures show that both devices are free from deformations after the development step.

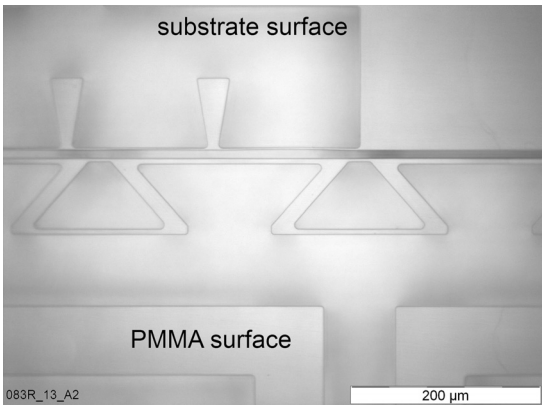

(a) Developed resist without aux. structures

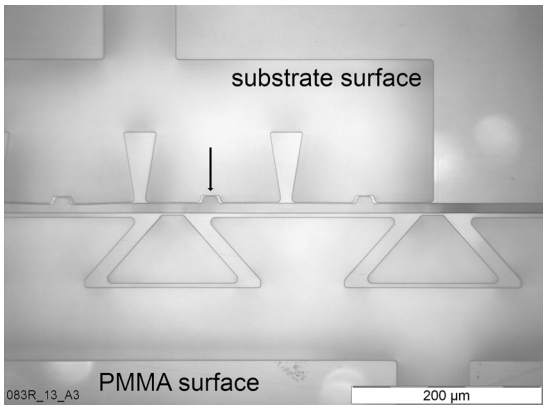

(b) Developed resist with aux. structures

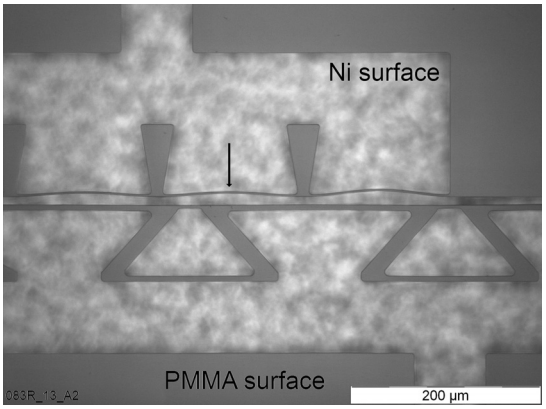

(c) Electroplated without aux. structures

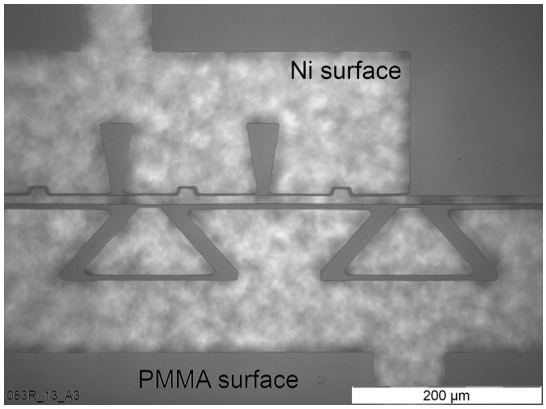

(d) Electroplated with aux. structures

Figure 3.7: Variable capacitors with and without auxiliary structures. Structures shown after development and after nickel electroplating with evacuation at 27 °C.

Figures 3.7(c) and 3.7(d) are the same structures after nickel electroplating to a height of 100 µm from a nickel sulfamate bath with evacuation at 27 °C. The device without periodic widening of the beam (A2) is clearly distorted as highlighted by the arrow, where as the device with the auxiliary structures (A3) is free from deformations. The deformations during the electroplating process are due to PMMA swelling in the aqueous electroplating bath [84] and possible lack of adhesion of the thin beams to the substrate during the development process.

Figure 3.8 [50] shows the effects that electroplating conditions can have on structure quality. All three figures show device B3 in 150 µm of PMMA electroplated from a nickel sulfamate bath. Figure 3.8(a) was plated at 27 °C with evacuation, Figure 3.8(b) was plated

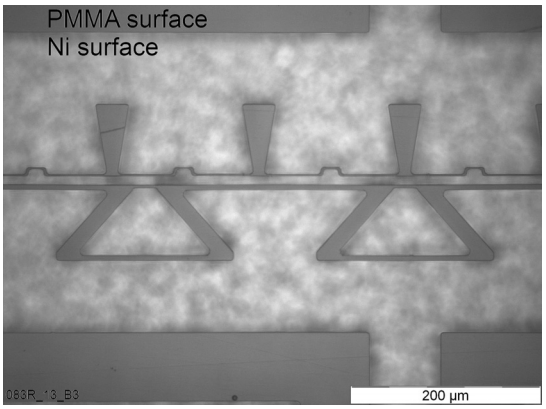

(a) $T_{plating}$ = 27 °C with evacuation

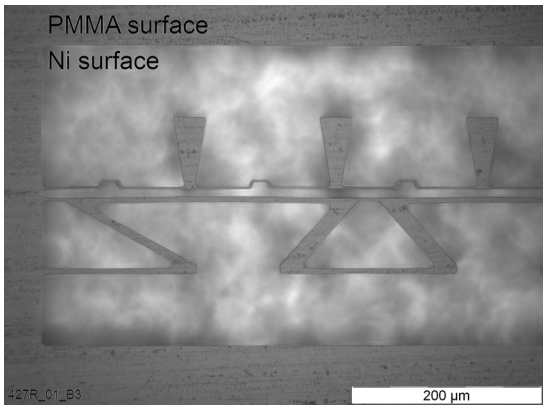

(b) $T_{plating}$ = 24 °C without evacuation

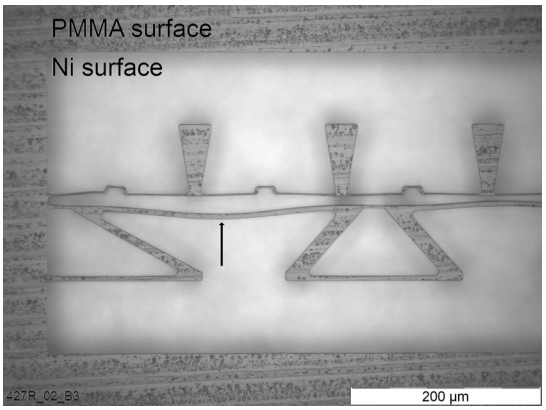

(c) $T_{plating}$ = 52 °C without evacuation

Figure 3.8: Effects of electroplating conditions on structure quality.

at 24 °C without evacuation and Figure 3.8(c) was plated at 52 °C without evacuation, which is the standard nickel sulfamate bath electroplating temperature. It can be seen that the baths operating around room temperature have significantly reduced deformations compared to the high temperature electroplating bath. The deformations are indicated by the arrow in Figure 3.8(c). These images show that the stress during the plating process can be significantly reduced if the plating temperature is reduced to near ambient temperatures. This eliminates thermal distortions stemming from the higher thermal expansion coefficient of PMMA compared to the substrate ($\alpha_{\text{PMMA}} \approx 70 \times 10^{-6}$ K^{-1}, $\alpha_{\text{alumina}} \approx 5 \times 10^{-6}$ K^{-1}) and also reduces the resist swelling in the electrolyte [84].

Figures 3.9(a) and 3.9(b) show capacitor b5 in 100 μm thick PMMA and capacitor B5 in 150 μm thick PMMA respectively. Significant deformations can be seen in both the actuator and capacitance gaps in Figure 3.9(b) as indicated by the arrows. These images show that thinner samples are less prone to deformations and device yield increases as the structure height is reduced.

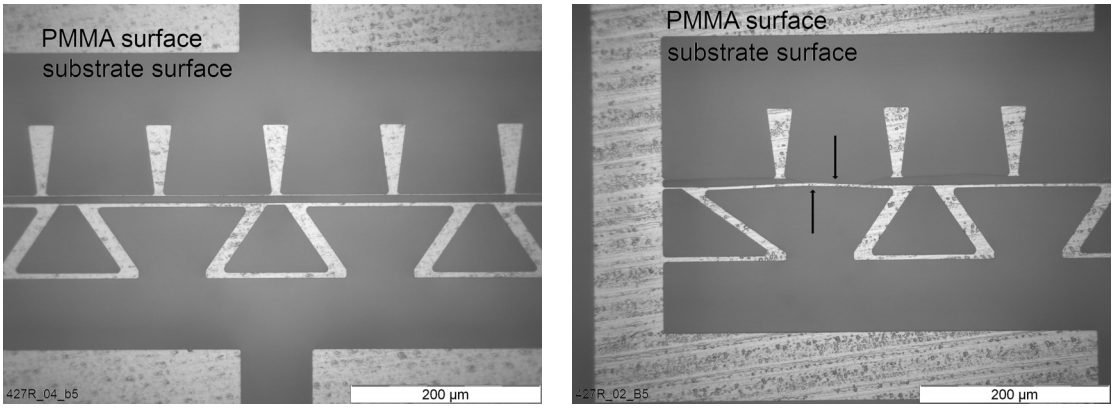

(a) 100 μm PMMA (b) 150 μm PMMA

Figure 3.9: Effects of structure height on structure quality.

Figure 3.10 is a collection of SEM images of 100 μm tall nickel capacitor structures. Figures 3.10(a) and 3.10(b) are overview images of devices f10 and e10 respectively. These are the largest capacitors in the layout. Figures 3.10(c) and 3.10(d) are magnified views of the tip portion of the cantilever beam of device f7, the smallest devices in the layout. Auxiliary structures including the periodic widening of the cantilever beam and the triangular electrode voids for resist relief can be clearly seen. Slight rounding of sharp corners can also be observed, which was done to prevent photoresist cracking during processing. Figure 3.10(e) is an inclined close-up view of the tip of the cantilever beam and the capacitance and actuator gaps of device f7. This figure demonstrates not only the large aspect ratios of the cantilever and gaps, but also the excellent verticality and precise feature geometry obtained using DXRL and metal electroforming. For this particular device, the beam width is 7.8 μm, the actuator gap is 4.7 μm and the capactitance gap is 1.6 μm. The aspect ratio of the small

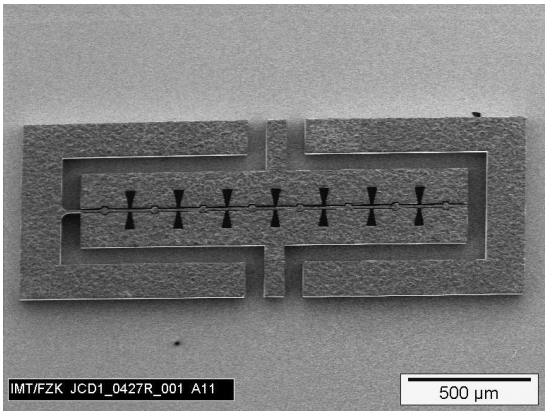

(a) f10 top-view overview

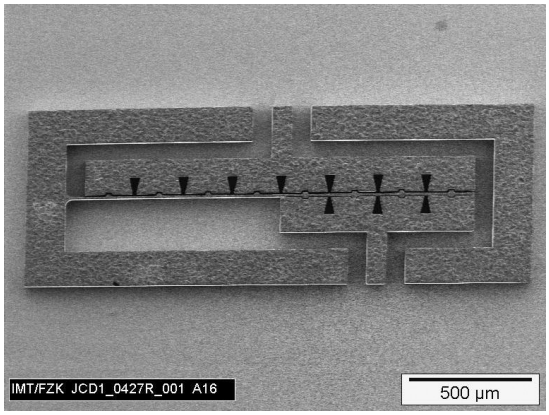

(b) e10 top-view overview

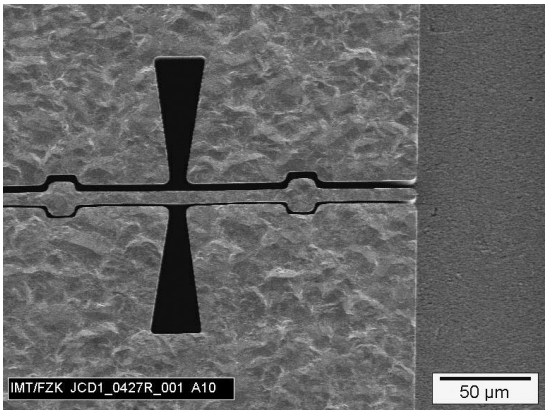

(c) f7 top-view beam tip overview

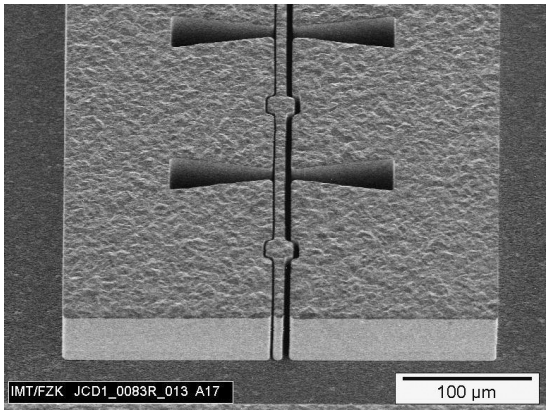

(d) f7 incline-view beam tip overview

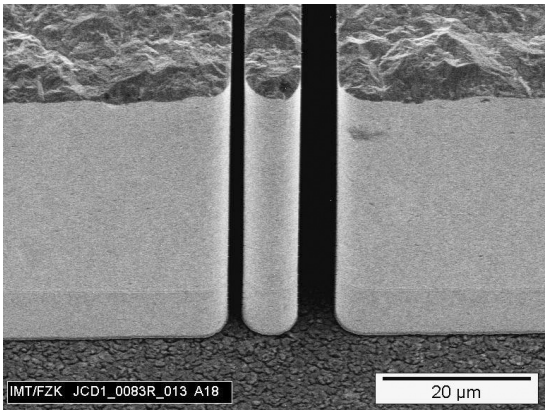

(e) f7 incline-view beam tip and air gaps

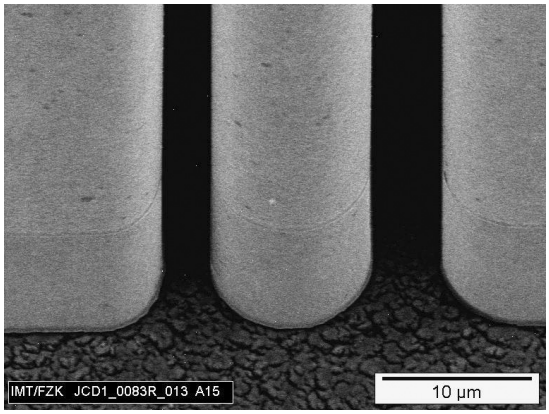

(f) a10 incline-view base of beam tip

Figure 3.10: SEM images of 100 µm tall nickel variable capacitors.

capacitance gap is approximately 60:1 in 100 μm nickel and 90:1 in 150 μm PMMA. The electrodes for this device are 1 mm long. These extremely thin, vertical walls of PMMA run laterally for hundreds of micrometers on the substrate. These walls support the thick metal microelectroplating without breaking or excessive deformation. Figure 3.10(f) is a highly magnified view of the base of the cantilever tip and air gaps of device a10. The roughened Ti/TiO_x electroplating seed layer can be observed as well as a faint horizontal line in the nickel depicting the separation of the glue layer and the resist foil that sits above it. Also visible are the very smooth sidewalls of the electroplated nickel.

Figure 3.11 is a collection of SEM images of 100 μm tall gold capacitor structures. Figures 3.11(a) and 3.11(b) are overview images of devices f7 and e7 respectively, which

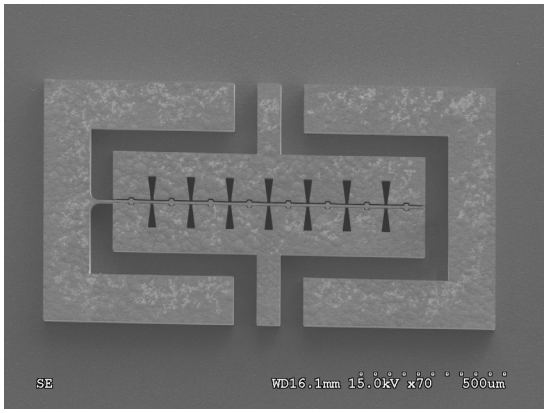

(a) f7 top-view overview

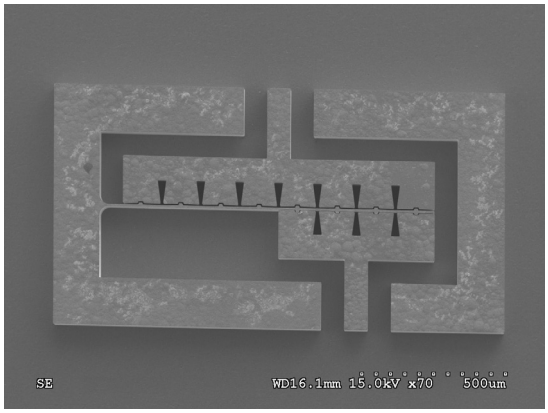

(b) e7 top-view overview

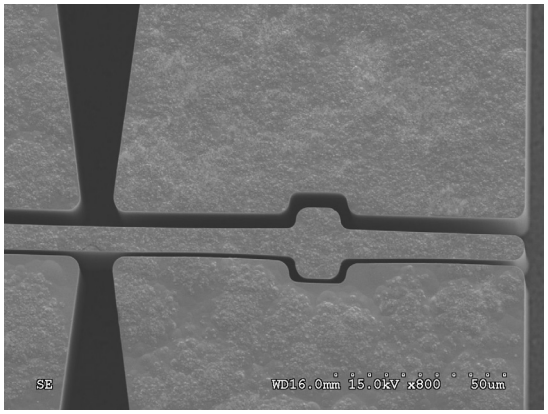

(c) f7 top-view beam tip

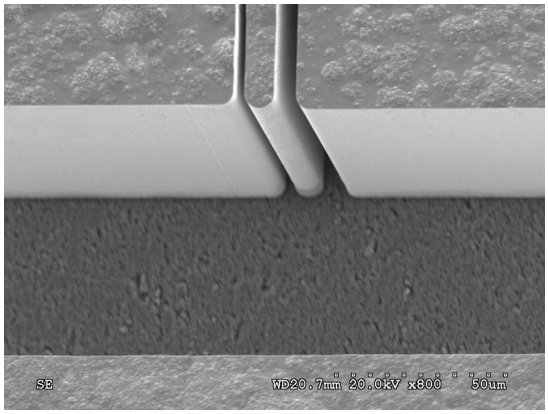

(d) f3 incline-view beam tip and air gaps

Figure 3.11: SEM images of 100 μm tall gold variable capacitors.

are the smallest capacitors in the layout. Figure 3.11(c) is a magnified view of the tip portion of capacitor f7 and Figure 3.11(d) is an inclined view of the cantilever tip and air gaps of device f3.

Devices containing stopper bumps (columns A - D and a - d) were unsuccessfully processed in the etching step as significant underetching of the stopper bumps created a loss of adhesion with the substrate. This could likely be remedied with improved etching techniques developed later, including the dilution of HF acid with isopropyl alcohol (isopropanol, IPA) instead of deionized water to reduce the surface tension, which helps the etchant to more quickly and uniformly penetrate into the high aspect ratio gaps.

3.3 Simulation and Test Results

Full-length and half-length capacitance electrode variable capacitors in two sizes (large and small) were measured. The large devices (e10, f10) were fabricated in 100 μm thick nickel on alumina, and the small devices (e7, f7) were fabricated in 100 μm thick gold on alumina [5,85]. The measured width dimensions of the four variable capacitors are summarized in Table 3.2. The length dimensions are listed in Table 3.1. These values were not measured, but are expected to be within a few microns of the values given in Table 3.1.

Table 3.2: Dimensions of measured and simulated vertical RF MEMS variable capacitors.

Device Type	Beam Width [μm]	Actuator Gap Width [μm]	Capacitance Gap Width [μm]
large (nickel) (e10, f10)	11.0	7.3	2.5
small (gold) (e7, f7)	7.5	4.3	1.3

The capacitors were tested using an Agilent 8722ES vector network analyzer (VNA) connected to the devices using coaxial cables terminated with Cascade ACP40-W-GSG-150 microprobes. These are tungsten ground-signal-ground (GSG) probes with a pitch (centre-to-centre spacing of adjacent probe fingers) of 150 μm and a maximum operating frequency of 40 GHz. Tungsten probes were used because the nickel surface was found to be too hard for the standard beryllium copper (BeCu) probes. The microprobe is attached to a micropositioner, providing fine motion for positioning the probe onto the capacitor.

Calibration of the test setup must be performed to eliminate the influence of the test setup on the measurement results. The calibration procedure used is a common procedure called a short-open-load-thru (SOLT) calibration. By measuring known impedance standards, the effects of the test setup can be automatically removed by the VNA. To perform this, a Cascade 101-190 calibration impedance standard substrate (ISS) was used. This substrate provides the short, load, and thru standards. The open standard is implemented with the probes in the air. Since the measurements to be made are 1-port measurements, the thru standard is not used, as it is only relevant to 2-port measurements. These 3 known impedances, short-open-load, are used to eliminate the effects of the test setup from the measurement results.

Impedance measurements were calculated directly from calibrated one-port reflection measurements. To actuate the capacitors, DC control voltage was provided through a second microprobe connected to the actuation electrode. Measurements were performed over 2 frequency bands, 1 - 6 GHz for the full capacitance electrode devices and 2 - 8 GHz for the half capacitance electrode devices.

Static 3-D high frequency electromagnetic simulations were performed using HFSS modelling a structure geometry with no applied bias voltage (0 V). The devices were simulated using a 3 μm titanium seed layer on a 1 mm alumina substrate and 100 μm of electroplated metal (nickel or gold) above the seed layer. The electrical material properties used are the same as the ones discussed previously. The devices were simulated over the same frequency range as the measurement results in steps of 0.5 μm.

Beam bending simulations (2-D) were performed using ANSYS to determine the change in gap capacitance with actuation voltage. These simulations are DC simulations and do

not consider high frequency effects as the HFSS simulations do. Bulk mechanical material properties were used for the simulations with values for Young's modulus and Poisson's ratio of ($E = 207$ GPa, $\nu = 0.31$) for nickel and ($E = 78$ GPa, $\nu = 0.45$) for gold respectively [49].

Measured and simulated results for the four capacitors are shown in Figures 3.12 to 3.19 [5, 85]. For each device, three static (0 V) impedance results including the resistance (R), reactance (X) and Q-factor as a function of frequency and two tuning characteristics including the capacitance (C) and the Q-factor as a function of tuning voltage are given. The tuning characteristics are determined at 4.0 GHz for the full capacitance electrode devices and 6.0 GHz for the half capacitance electrode devices.

A summary of the important measured [and simulated] performance parameters for the variable capacitors are given in Table 3.3. The simulated results are interpolated from the analyzed frequency points. Results are listed at nominal values corresponding to reactances of approximately 50 Ω ($X_c = 50$ Ω) at the nominal operating frequency (f_o) to allow for consistent comparison. Devices are also compared at frequencies corresponding to a reactance range of 25 - 100 Ω ($X_c = 25$ - 100 Ω) to get an appreciation of the performance over a typical range that is suitable for lumped-element circuit applications.

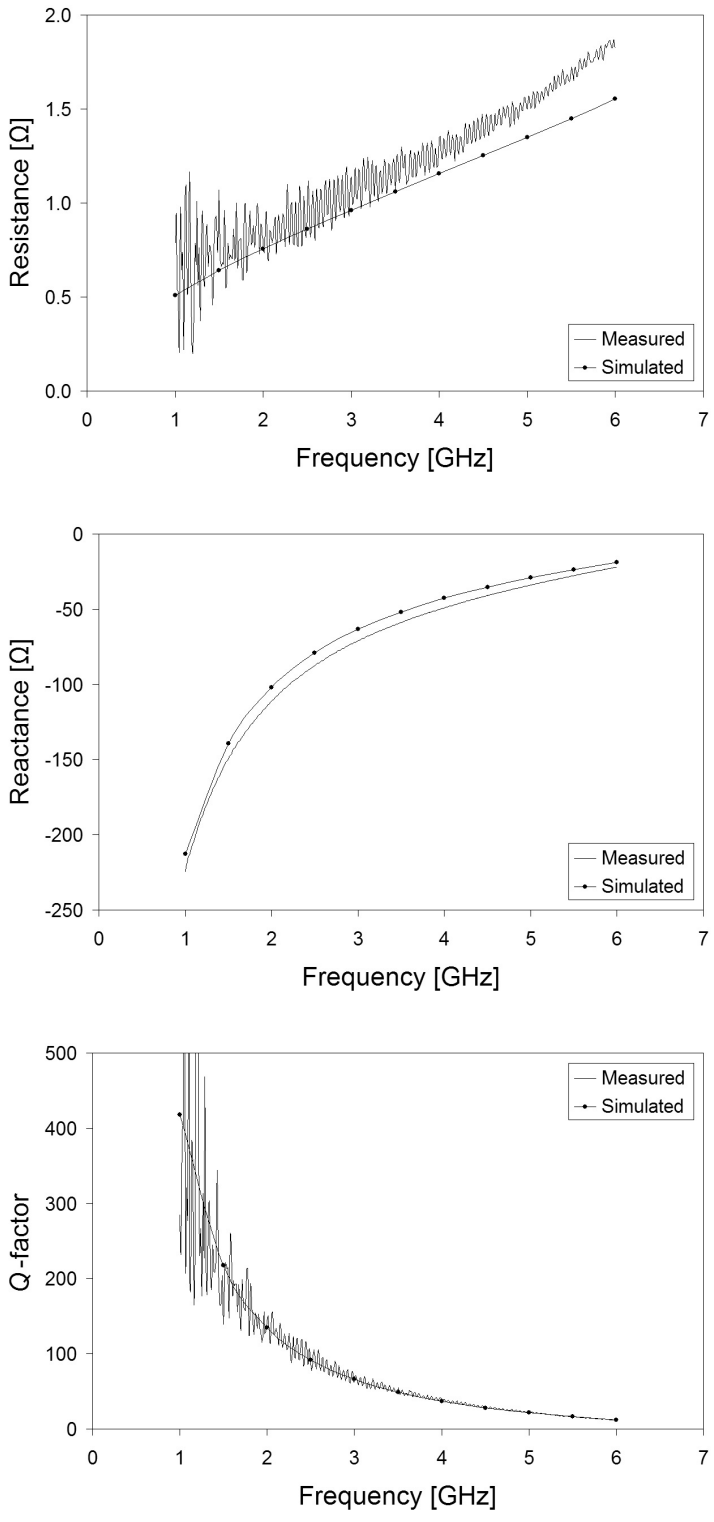

Figure 3.12: Measured and simulated static impedance results for a large full capacitance electrode nickel capacitor (f10) with no applied actuation voltage (0 V).

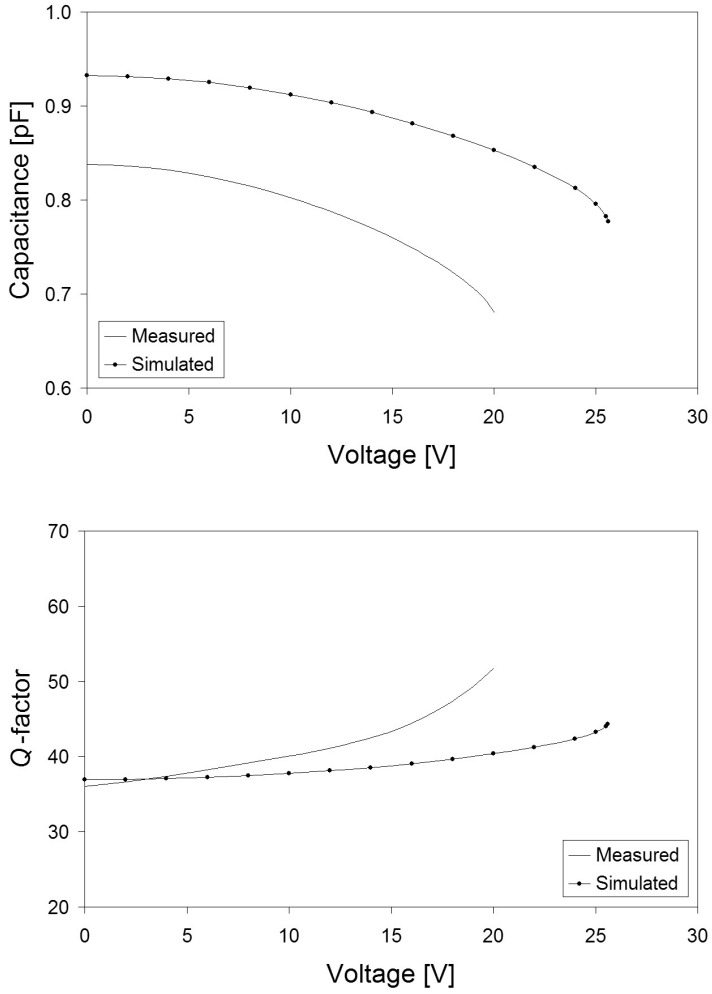

Figure 3.13: Measured and simulated tuning characteristics for a large full capacitance electrode nickel capacitor (f10) at 4.0 GHz.

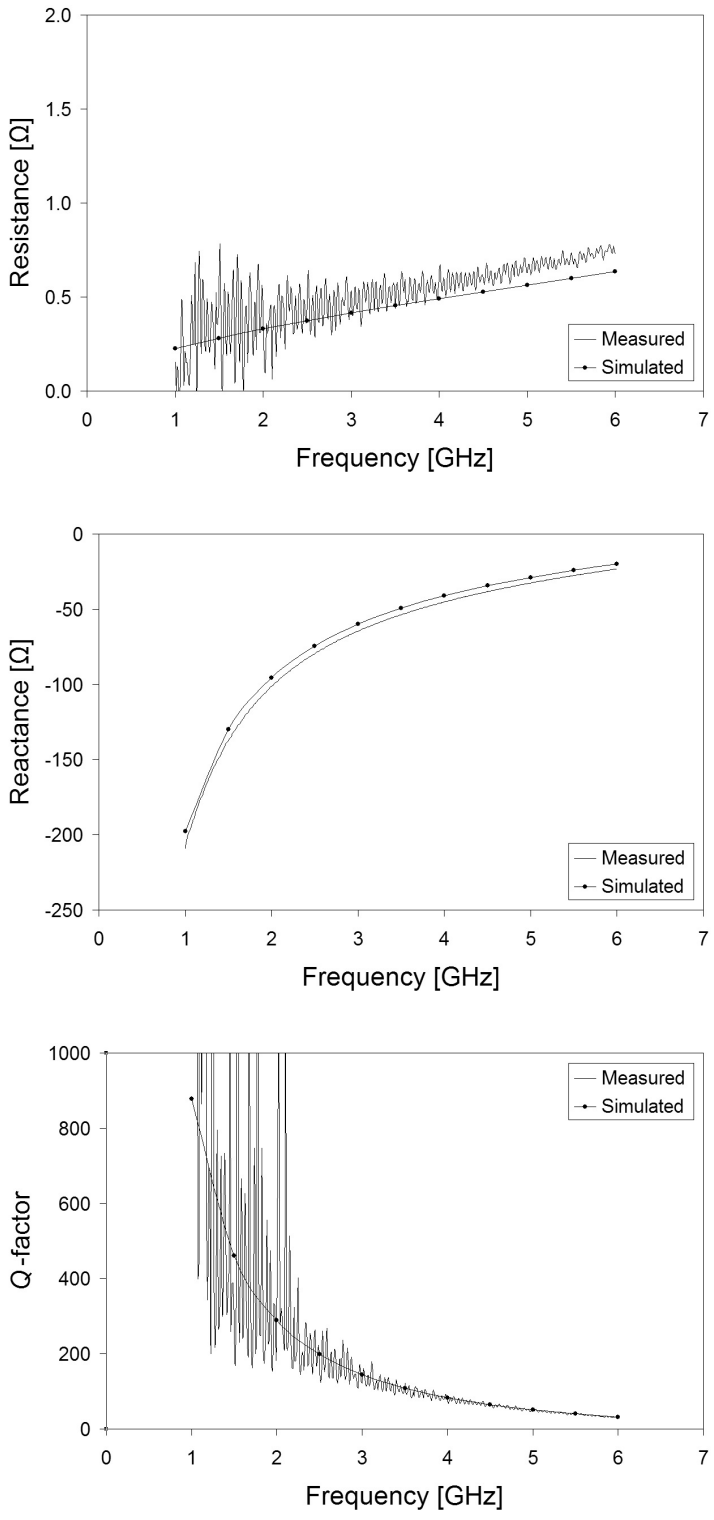

Figure 3.14: Measured and simulated static impedance results for a small full capacitance electrode gold capacitor (f7) with no applied actuation voltage (0 V).

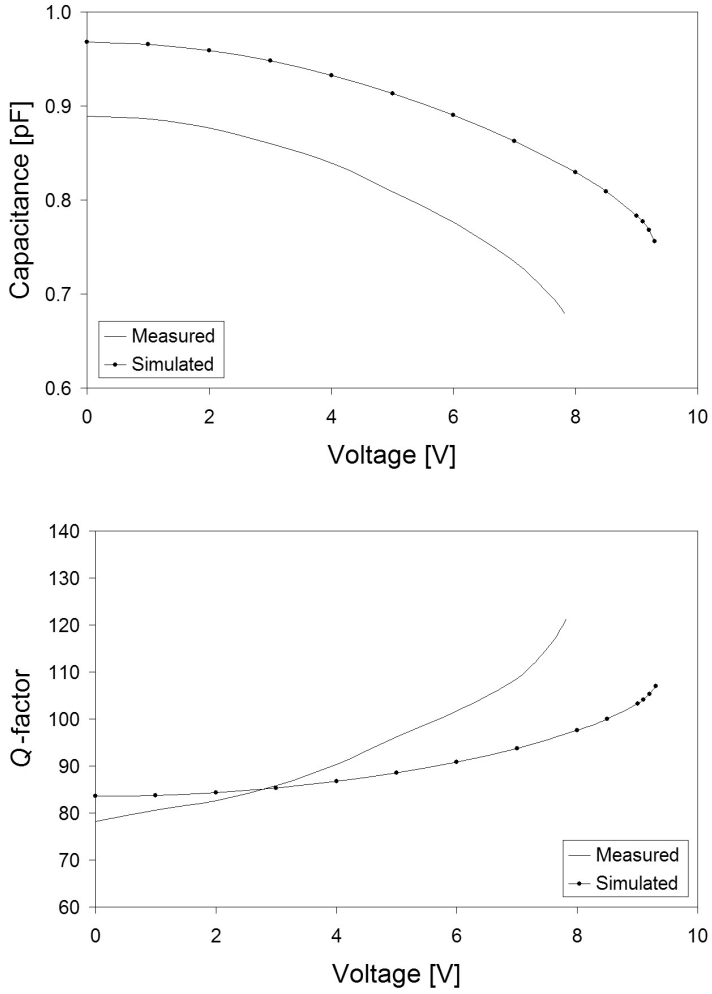

Figure 3.15: Measured and simulated tuning characteristics for a small full capacitance electrode gold capacitor (f7) at 4.0 GHz.

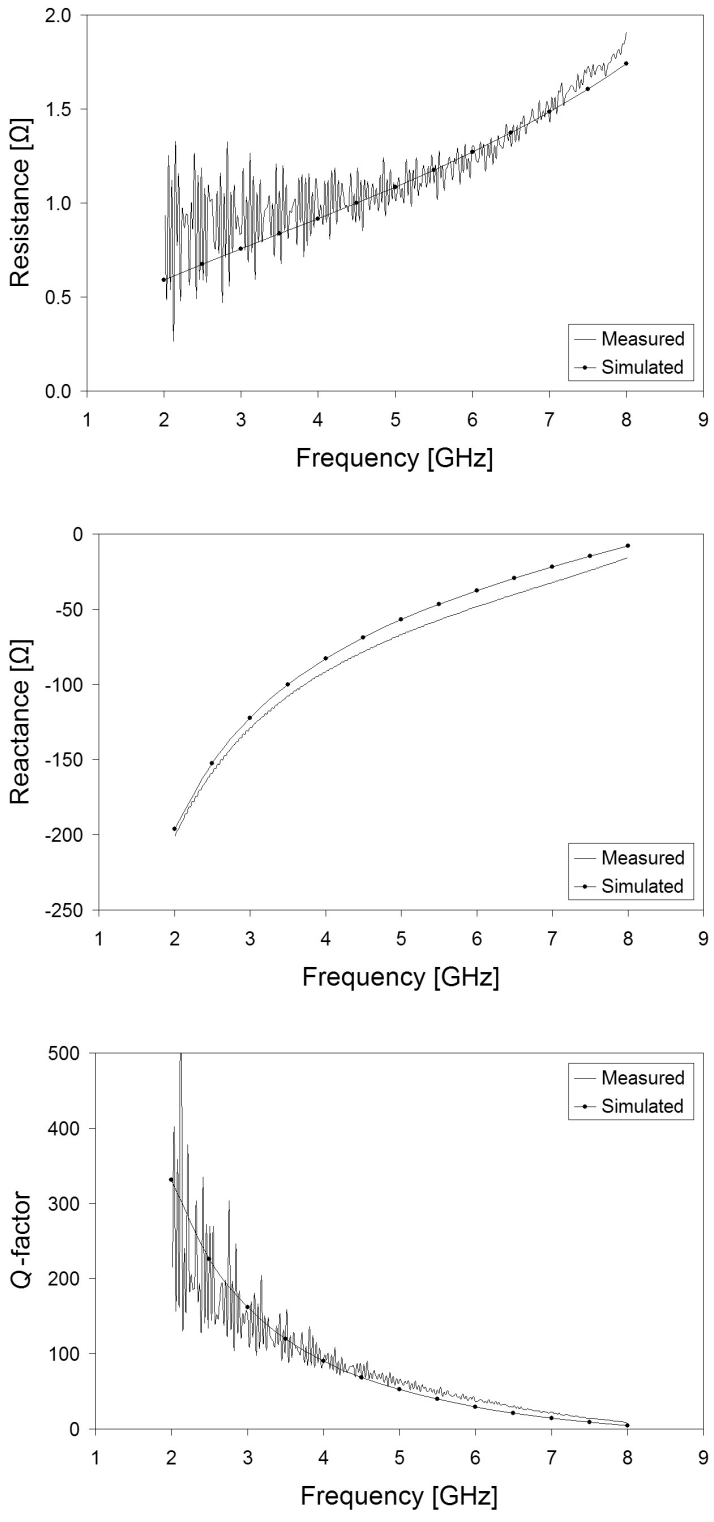

Figure 3.16: Measured and simulated static impedance results for a large half capacitance electrode nickel capacitor (e10) with no applied actuation voltage (0 V).

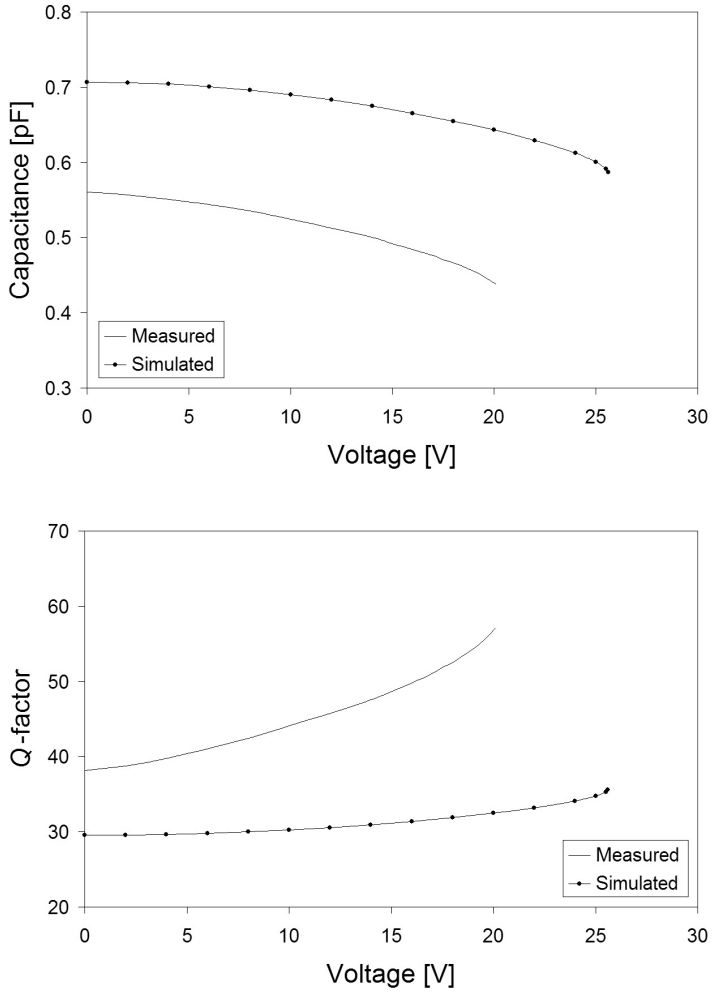

Figure 3.17: Measured and simulated tuning characteristics for a large half capacitance electrode nickel capacitor (e10) at 6.0 GHz.

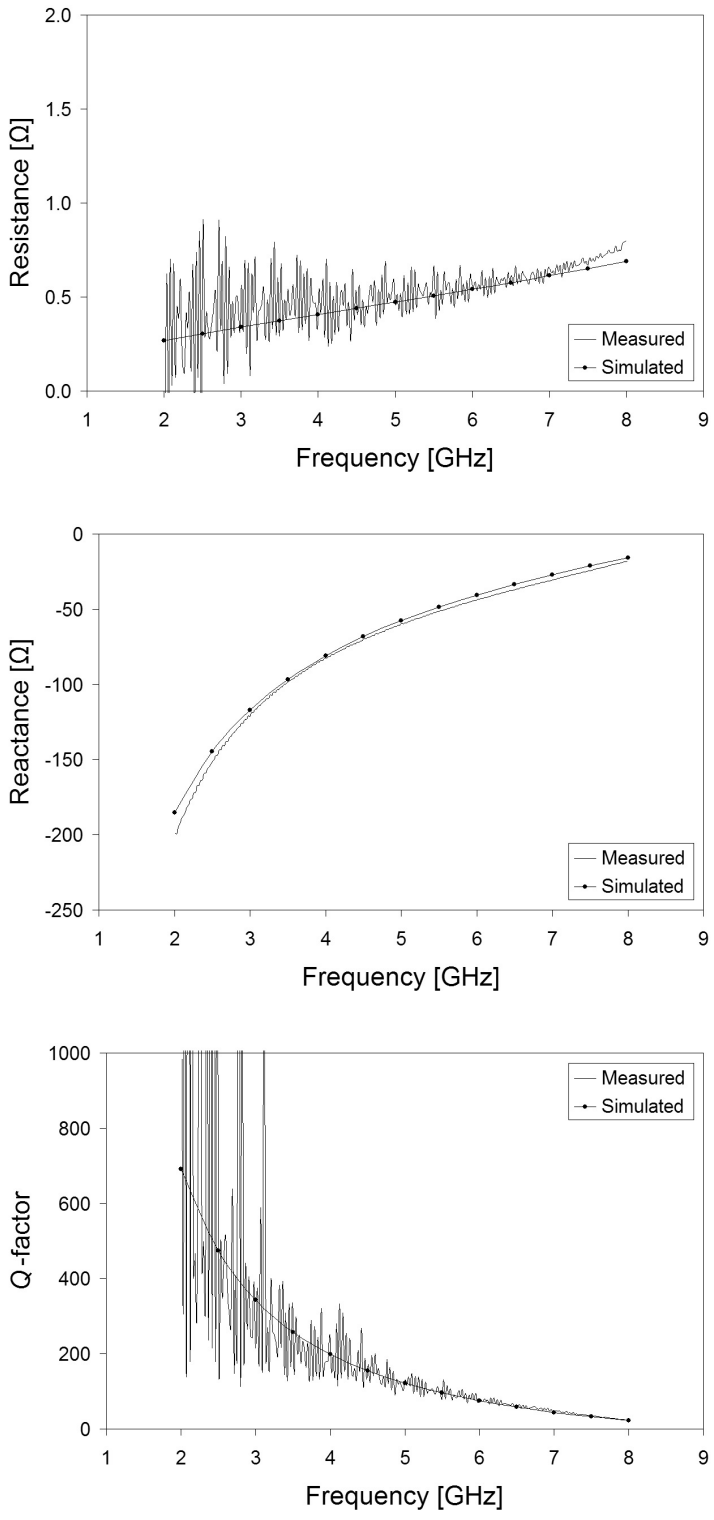

Figure 3.18: Measured and simulated static impedance results for a small half capacitance electrode gold capacitor (e7) with no applied actuation voltage (0 V).

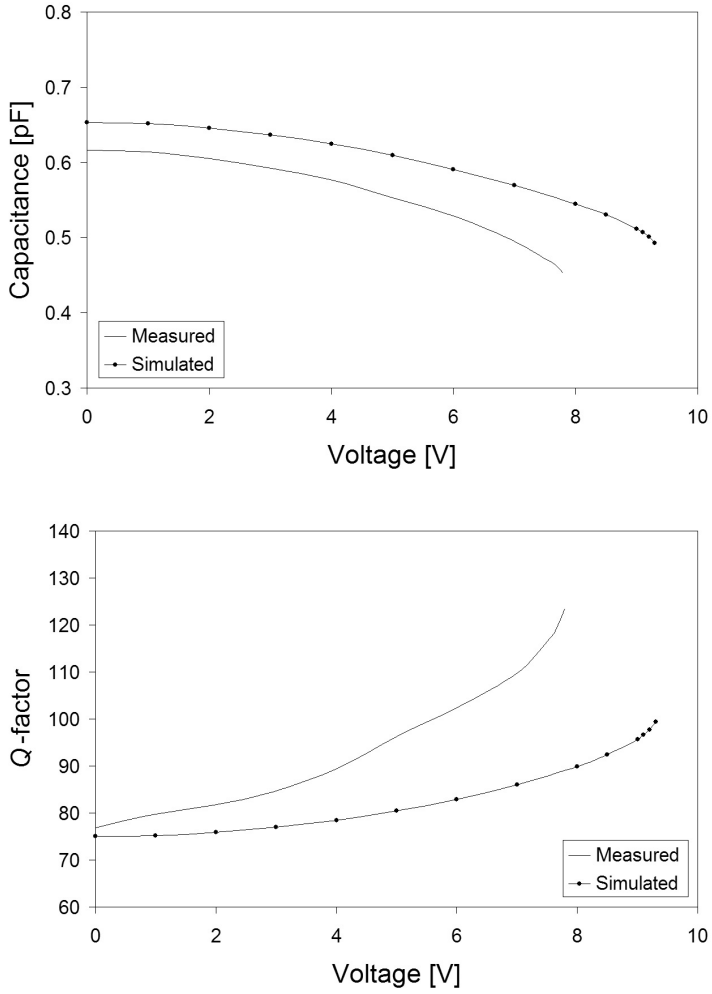

Figure 3.19: Measured and simulated tuning characteristics for a large half capacitance electrode nickel capacitor (e7) at 6.0 GHz.

Table 3.3: Summary of measured [and simulated] vertical RF MEMS variable capacitor performance.

Device Type	C_o [pF] @f_o	R_o [Ω] @f_o	Operating Frequency [f_o, GHz] $X_c = 50\ \Omega$	Frequency Range [GHz] $X_c = 25$ - $100\ \Omega$	C Tuning Range [pF]	Tuning Voltage [V]	Q @f_o	ΔQ $X_c = 25$ - $100\ \Omega$	SRF [GHz]
large full electrode	0.80	1.2	3.9	2.2 - 5.7	0.84 - 0.68	0.0 - 20.0	41	15 - 120	7.6
(nickel) (f10) [5, 85]	[0.88]	[1.1]	[3.6]	[2.0 - 5.4]	[0.93 - 0.78]	[0.0 - 25.6]	[46]	[18 - 130]	[7.4]
small full electrode	0.86	0.5	3.7	2.0 - 5.8	0.89 - 0.68	0.0 - 7.8	94	35 - 266	8.9
(gold) (f7) [5]	[0.92]	[0.4]	[3.5]	[1.9 - 5.4]	[0.97 - 0.76]	[0.0 - 9.3]	[112]	[42 - 309]	[8.5]
large half electrode	0.54	1.2	5.9	3.7 - 7.5	0.56 - 0.44	0.0 - 20.1	42	15 - 107	8.9
(nickel) (e10) [5]	[0.60]	[1.1]	[5.3]	[3.5 - 6.8]	[0.71 - 0.59]	[0.0 - 25.6]	[44]	[17 - 119]	[8.6]
small half electrode	0.57	0.5	5.6	3.5 - 7.4	0.62 - 0.45	0.0 - 7.8	95	39 - 214	10.1
(gold) (e7) [5]	[0.59]	[0.5]	[5.4]	[3.4 - 7.2]	[0.65 - 0.49]	[0.0 - 9.3]	[99]	[40 - 274]	[9.6]

As mentioned previously, the ANSYS beam bending simulations used to determine the change in gap capacitance are DC simulations and do not consider high frequency effects as the HFSS simulations do. Therefore, in order to determine the simulated tuning capacitance at a desired frequency, the gap capacitance, with no actuation voltage, determined by ANSYS was subtracted from the calculated capacitance from HFSS high frequency impedance results. This remainder is a parasitic capacitance value and is added to the gap capacitance tuning characteristic, which approximates the change in capacitance at the desired frequency. To determine the simulated Q-factor as a function of tuning voltage this approximated capacitance change is used along with the resistance ($R = \mathrm{Re}\{Z_{11}\}$) value predicted using HFSS at that frequency. From the measured tuning characteristics, the real component of the impedance decreases slightly with an increase in tuning voltage. A more rigorous and very time consuming method, which was not investigated here, would be to import the beam geometry predicted using ANSYS into HFSS and perform full 3-D high frequency electromagnetic simulations as a function of frequency for each tuning voltage step performed using ANSYS.

The 50 Ω operating frequency is in the range 3.7 - 3.9 GHz for full-length electrode devices and 5.6 - 5.9 GHz for half-length electrode devices. The typical 25 - 100 Ω reactance range is 2.0 - 5.8 GHz for the full-length electrode devices and 3.5 - 7.5 GHz for the half-length electrode devices. The static capacitance of the full-length electrode capacitors at the 50 Ω operating frequency is 0.8 - 0.9 pF and for the half-length electrode devices is 0.5 - 0.6 pF. Evident from Figures 3.12, 3.14, 3.16, and 3.18 are high-quality capacitive reactances, with very low parasitic resistances of $< 1\ \Omega$ for gold devices and $< 2\ \Omega$ for nickel devices up to 8 GHz. In fact, the half-length electrode gold device has a parasitic resistance of 0.5 Ω up to around 6 GHz. The real component of the measured impedance is quite erratic (especially at low frequencies), but appears to follow a definite trend. This occurs since with a low frequency, the magnitude of the impedance is large, therefore the error in the small real component of the impedance will be larger at low frequencies. The parasitic resistance is an indication of both metal conductive losses and dielectric losses in the device, and both are low as a result of the compact vertical structure. The capacitive plates are perpendicular to the substrate; thus, most of the electric field intensity is concentrated above

the substrate, resulting in low dielectric loss. The capacitive plates are also perpendicular to the signal propagation direction, resulting in relatively short metallic resistance paths and low conductive losses. The low loss is reflected in the Q-factors for the variable capacitor devices. Nickel capacitors have Q-factors around 41 - 42 at their nominal 50 Ω operating frequencies, while Q-factors approach 200 in the lower portion of the frequency ranges. Due to the higher conductivity, the gold capacitors have higher Q-factors of the order of 94 - 95 at their nominal 50 Ω operating frequencies and in excess of 500 in the lower portion of the frequency ranges.

Figures 3.13, 3.15, 3.17, and 3.19 plot the measured and simulated tuning characteristics of the nickel and gold variable capacitors near the nominal operating frequencies. As the tuning voltage is increased from 0 V, the beam bends gradually toward the actuation electrode until the pull-in voltage (the right-most point on the curves) is reached. Increasing the voltage beyond the pull-in voltage causes the beam to rapidly deflect onto the actuator electrode. Significant local electrostatic force is realized in the compact variable capacitor structures. For instance, the measured pull-in voltage for the nickel structures is only around 20 V for both the full electrode structure at 4 GHz (Figure 3.13) and the half-length electrode version at 6 GHz (Figure 3.17), which is somewhat less than the simulated values for nickel of 25.6 V. The main reason for this is likely a reduced elastic modulus for electroplated nickel compared with bulk nickel. Aside from the smaller pull-in voltage, the bending characteristics of the measured devices match quite well with that predicted by simulation, considering that the simulation results include approximated high-frequency parasitic capacitance effects. The measured capacitive tuning ratios for the nickel devices are 1.23:1 for the full-length electrode device and 1.28:1 for the half-length electrode device.

As a result of the reduced elastic modulus, the gold structures have considerably lower pull-in voltages, some 7.8 V for both the full electrode structure at 4 GHz (Figure 3.15) and the half-length electrode version at 6 GHz (Figure 3.19). Again, these measured values are slightly less than those of 9.3 V predicted by simulations for the same reason as described above for nickel. The measured capacitive tuning ratios for the gold devices are 1.31:1 for the full-length electrode device and 1.36:1 for the half-length electrode device.

3.4 Summary

Pull-away style, high aspect ratio, high Q-factor, RF MEMS variable capacitors have been fabricated using deep X-ray lithography and electroplating. These devices demonstrate that DXRL is suitable for the fabrication of high performance RF MEMS devices with movable parts due to the ability to fabricate thick metal structures with precise features. PMMA layers of 100 μm and 150 μm have been patterned and electroplated with 70 μm and 100 μm thick nickel and gold. The fabricated capacitors feature very long beams ($>$ 1 mm) and narrow gaps (down to 1.3 μm) which results in high aspect ratios of approximately 115 in PMMA and 75 in gold. A 3 μm thick titanium thin film was used as plating base as well as etch time-controlled sacrificial layer. Thus, the cantilever beam was released without an additional lithographic layer while still providing good adhesion of the larger adjacent metal structures. Auxiliary layout structures are required to successfully process these high aspect ratio polymer structures. Subsequent electroforming severely deforms the microstructures unless processed at close to ambient temperature.

The tall vertical structure of these devices results in low loss and high performance, mainly due to the separation of fields from the substrate and the use of thick metal layers. Q-factors as large as 214 at 3.5 GHz, 95 at 5.6 GHz and 39 at 7.4 GHz have been measured for a capacitor with a 0.57 pF nominal capacitance at 5.6 GHz. This same device features a 1.36:1 tuning ratio at 6 GHz and a tuning voltage of 7.8 V.

4. Design Challenges

This chapter discusses some of the challenges encountered when designing micro-scale moving structures. Some of these challenges are general issues for movable MEMS devices, some are specific to electrostatically actuated MEMS devices and some are specific to MEMS variable capacitors. A few of these challenges have been discussed in detail in [19], and will be briefly discussed in the following sections. The others will be discussed in greater detail.

4.1 Stiction

4.1.1 Introduction

A thorough investigation of the stiction phenomena and how it relates to this class of structures was presented in [86]. One of the major challenges with MEMS devices is the fact that as device dimensions decrease, the surface to volume ratio increases. Surface phenomena are of great importance to MEMS fabrication and this includes surface adhesion. The characteristics commonly found in MEMS devices can often lead to the adhesion of these thin beams and plates to adjacent structures. This adhesion phenomenon has been given the term "stiction", which has been used to describe the unintentional adhesion of compliant microstructure surfaces when restoring forces are unable to overcome interfacial forces [87].

One of the main issues with the capacitors presented in Chapter 3 is that most of the devices suffered from stiction. An example of this is shown in Figure 4.1, which is the cantilever tip of capacitor e10 in 100 μm tall nickel. Figure 4.1 (top) shows a wet device after being etched in 5% HF and then rinsed in de-ionized (DI) water. This etching procedure removes the titanium sacrificial layer beneath the beam. No sticking occurs, air gaps are observed on both sides of the cantilever. Once the water has evaporated, as shown in Figure 4.1 (middle), the device sticks to the closer adjacent electrode. These observations clearly show that the observed stiction is a result of the combination of capillary force during evaporation and intersolid adhesion and is not due to an internal stress present in the cantilever. Figure 4.1 (bottom) shows the device after being released with a stream of

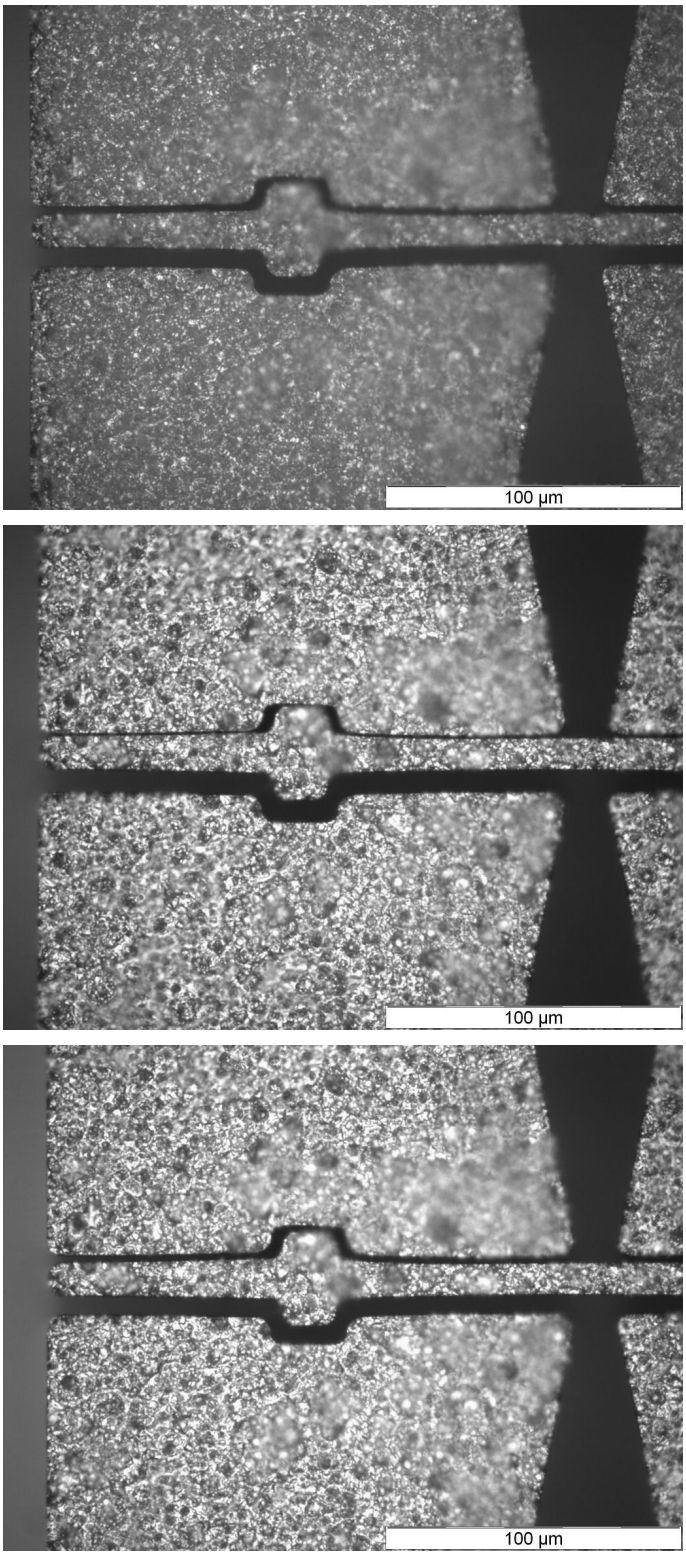

Figure 4.1: Cantilever tip of 100 µm tall nickel capacitor e10. *Top*: wet sample after etch. *Middle*: dry sample showing stiction. *Bottom*: nitrogen released sample.

compressed nitrogen. This was found to be a useful approach at the prototype level, since the beams can be reliably released without damage and the devices can therefore be tested, however this is not a satisfactory solution to the stiction problem on a fabrication-scale level. Stiction theory, including the conditions for stiction to occur and critical dimension formulas, will now be investigated to see whether slight changes in the capacitor layout can eliminate the observed stiction problem.

For stiction to occur, two conditions must be satisfied: (1) mechanical collapse of the structure onto an adjacent structure must happen and (2) the intersolid adhesion between the collapsed structure and the adjacent structure must be greater than the restoring force of the collapsed structure [88]. Intersolid adhesion of the two surfaces can result from various forces such as van der Waals forces, electrostatic forces, and hydrogen bridging forces, depending on the nature of the surfaces [89]. If either of these conditions is not satisfied, then stiction will not occur. The first condition, mechanical collapse, can be divided into two categories: (a) release related collapse and (b) in-use collapse [90]. Release related collapse is often a result of the capillary force during the drying process after the removal of the sacrificial layer. This was the case in the example shown in Figure 4.1. Two situations can lead to in-use collapse: (i) the microstructure is exposed to a humid atmosphere leading to capillary condensation and the formation of a water droplet in the gap [91] and (ii) an external force causes the structure to collapse either by deliberate placement of a collapsing force or by accidental shock.

4.1.2 Critical Dimensions

The following sections give equations and example figures that can be used during design to quantize the stiction problem. The first section addresses the problem of collapse by capillary force, the second section addresses the intersolid adhesion problem, and the third section provides a useful example for two cantilever structures.

Example high aspect ratio cantilever and fixed-fixed beam structures are shown in Figure 2.2 on page 29. The beam has a length l, width w, height h, and undeformed air gap d. The beams are anchored to the larger stationary structures and are the only portions of the structure that are not attached to the substrate allowing them to move freely.

Collapse by Capillary Force and the Elastocapillary Number

One of the main reasons for collapse during the fabrication and use of MEMS devices is the collapse by capillary force. This force results as the liquid evaporates from within the air gap separating the movable structure and a fixed adjacent structure. This liquid bridge pulls the movable beam onto the adjacent surface as the volume of the liquid decreases. A dimensionless number, called the elastocapillary number N_{EC}, has been proposed [92] to characterize the problem. The microstructure will not touch the adjacent surface during drying if $N_{EC} > 1$ and will touch the adjacent surface if $N_{EC} < 1$. This number can be explained as the ratio of elastic restoring energy to the capillary energy. The elastocapillary numbers for different structure types are shown in Table 4.1 with variable names changed from [92] to reflect the vertical rather than planar orientation of the beams.

Table 4.1: Elastocapillary numbers for different structure types [92].

Structure Type	Approximate Elastocapillary Numbers (N_{EC})
cantilever beam	$\frac{2}{9}\frac{Ed^2w^3}{\gamma_l \cos\theta_c l^4(1+w/h)}$ (4.1)
fixed-fixed beam	$\frac{128}{15}\frac{Ed^2w^3}{\gamma_l \cos\theta_c l^4(1+w/h)}\left[1+\frac{2}{7}\frac{\sigma_R l^2}{Ew^2}+\frac{108}{245}\frac{d^2}{w^2}\right]$ (4.2)

In Table 4.1, E is Young's (elastic) modulus, γ_l is the liquid surface tension, θ_c is the contact angle between the liquid and the solid, and σ_R is the residual stress. The critical length can be determined by setting N_{EC} to 1 and solving for the length. This will determine the largest structure that can be fabricated without touching during drying. The surface tension of water, a commonly used drying liquid, is 73 mN/m [93]. Other liquids are often used as a drying solution due to their lower surface tension, such as ethanol (22 mN/m) [93]

and n-hexane (19 mN/m) [94]. Contact angles are highly dependent on surface properties such as roughness and contaminants. For metal surfaces, the surface is nevertheless of high free energy and, under ambient laboratory conditions, covered with a reversibly physisorbed layer of water, hydrocarbons, and other organic compounds [95]. In [95] the authors report contact angles of $30^\circ - 70^\circ$ for freshly prepared gold slides under laboratory conditions. As a worst case scenario, the designer can assume a completely wetted surface ($\theta_c = 0^\circ$), which gives a lower bound to the above elastocapillary numbers.

Contact Stiction and the Peel Number

In order for the movable structure to stick after collapse, the intersolid adhesion must be greater than the restoring force of the structure, which is one of the conditions for stiction to occur and an example can be seen in Figure 4.1.

A number called the peel number N_P has been proposed for the intersolid adhesion problem [92], which is the ratio of elastic strain energy stored in the deformed microstructure to the work of adhesion between the microstructure and an adjacent structure. If $N_P > 1$, the restoring energy is greater than the work of adhesion and the structure will not stick. If $N_P < 1$, the structure cannot overcome adhesion and sticks to the substrate. The peel numbers for different structure types are shown in Table 4.2. The surface energy per unit area of the bond γ_s, depends on the nature of the adhesion forces at work. Typically, in strong crystalline solids this energy is very high ($500 - 2000$ mJ/m^2), and in soft solids, such as polymers, it is very low ($5 - 100$ mJ/m^2) [92]. These values are heavily influenced by surface contaminants and roughness as in the case for contact angle determination.

Critical Dimension Examples

The theoretical stiction results of two cantilever beam structures are presented. These results are a useful example of the types of issues facing designers of movable high aspect ratio structures. The two cantilevers have identical geometries, but are a different material, both commonly used in fabricating high aspect ratio structures. Consider a cantilever beam dried using water (Figure 2.2(a), page 29) with a width w of 10 μm, an air gap d of 5 μm, and a height h of 100 μm. These dimensions are comparable with the dimensions of the capacitor

Table 4.2: Peel numbers for different structure types [92].

Structure Type	Approximate Peel Numbers (N_P)
cantilever beam	$\frac{3}{8}\frac{Ed^2w^3}{\gamma_s l^4}$ (4.3)
fixed-fixed beam	$\frac{128}{5}\frac{Ed^2w^3}{\gamma_s l^4}\left[1+\frac{4}{21}\frac{\sigma_R l^2}{Ew^2}+\frac{256}{2205}\frac{d^2}{w^2}\right]$ (4.4)

shown in Figure 4.1, which is a large nickel device presented in Chapter 3. The air gap value used here is between the large (actuator) and small (capacitance) gap sizes. The elastocapillary number and peel number for a nickel cantilever is plotted in Figure 4.2 (top). In the figure, two elastocapillary number curves are shown. The first is for a contact angle θ_c of 78° [96]. The second, a lower bound, corresponds to a completely wetted surface, a contact angle of 0°. The surface energy γ_s of nickel is 2240 mJ/m^2 [97]. The elastic modulus E of bulk nickel is 207 GPa [49]. The bulk nickel value was used since the value for LIGA electroplated nickel varies significantly in the literature and depends heavily on electroplating conditions.

Looking at the elastocapillary numbers, for a contact angle of 78°, the length of the shortest beam that will touch during drying is 513 μm. If the surfaces are completely wetted ($\theta_c = 0°$), the length of the shortest beam that will touch is 347 μm, which represents a lower bound. Looking at the peel number curve, the shortest beam that will stick after making contact is 173 μm. These results show that the intersolid adhesion of metal beams is very strong and even beams that are quite short will stick despite the large restoring force from the large elastic modulus, yet these shorter beams do not make contact during drying.

Figure 4.2 (bottom) is a plot of the elastocapillary number and peel number of a PMMA cantilever beam dried from water. The surface energy γ_s of PMMA is 43 mJ/m^2 [98]. The elastic modulus E of PMMA is 3.3 GPa [99], which is much lower than the value for

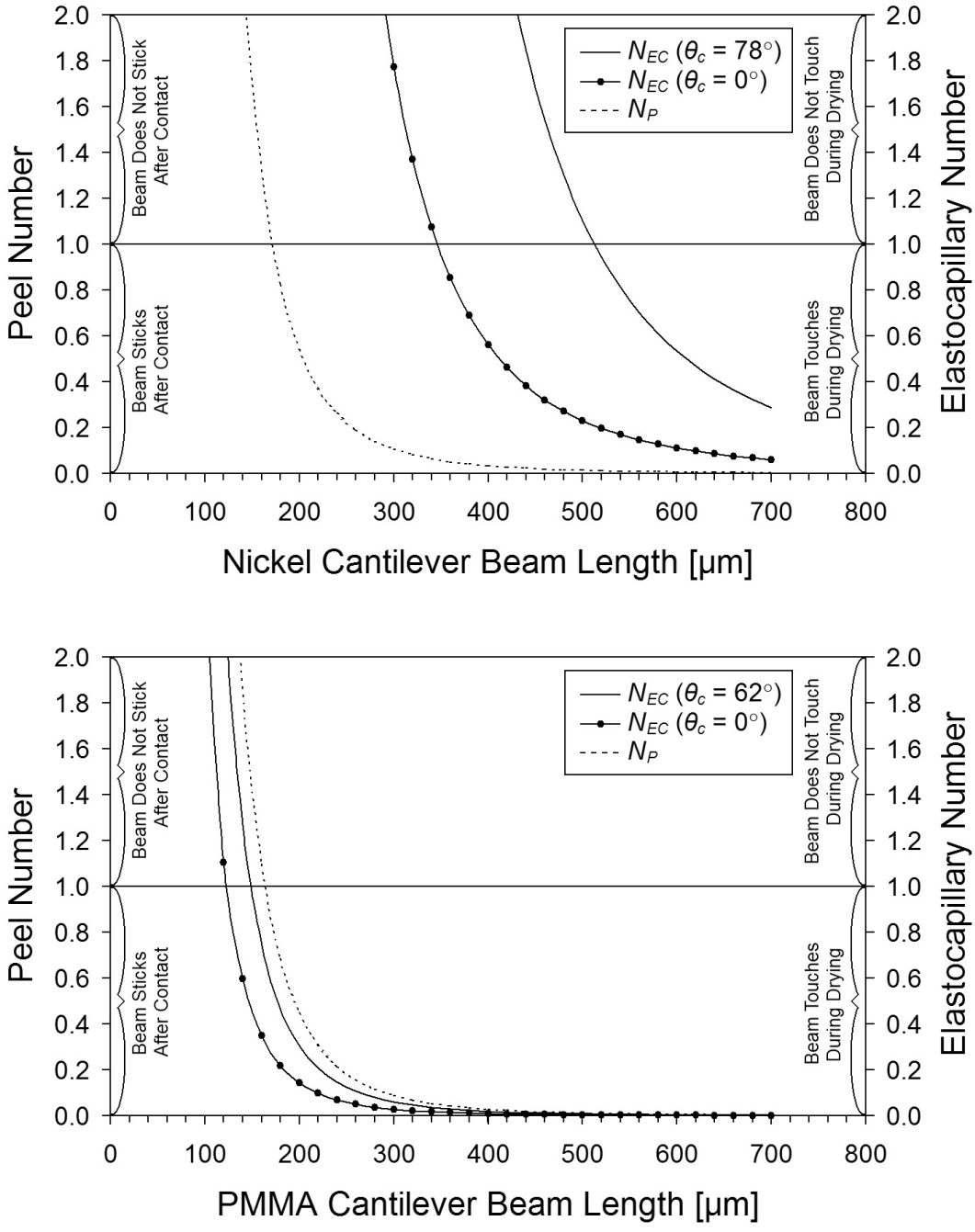

Figure 4.2: Stiction of high aspect ratio beams. *Top*: nickel. *Bottom*: PMMA.

nickel. Again two elastocapillary number curves are shown, corresponding to contact angles of 62° [98] and 0°. From the elastocapillary curves, for a contact angle of 62°, the shortest beam that will touch during drying is 150 μm. For a contact angle of 0°, this length becomes 124 μm. From the peel number curve, the shortest beam that remains stuck after contact is 165 μm. These results show that very small polymer beams, similar to the length of nickel beams, will stick despite the fact that they have a much lower surface energy. They stick because they also have a much lower elastic modulus, which decreases the elastic restoring force. In addition, beams smaller than the nickel beams will touch during drying due to the small elastic modulus.

4.1.3 Prevention

As shown in the previous chapter, the layout for capacitor devices requires a minimum length of the cantilever beams to be approximately 1 mm to give a suitable reactance in the desired frequency range. It is obvious that the theoretically derived critical cantilever lengths are so much shorter that stiction cannot be avoided by reducing the cantilever length without compromising device performance.

Many methods have been suggested and implemented to reduce or eliminate stiction. These can be divided into three categories; (1) methods that reduce or eliminate collapse due to capillary force, (2) methods that reduce the surface energy so that beams don't permanently adhere even if they come into contact, and (3) simultaneous solutions that eliminate capillary pull and reduce surface energy.

Methods that reduce capillary pull include drying using a low surface tension liquid such as ethanol or n-hexane [94] as well as drying at increased temperatures [100], which reduces the capillary force since surface tension decreases with increasing temperature. Also temporary supports can be added that prevent mechanical motion during drying, which are removed following the removal of the sacrificial layer. In fabrication for experimental purposes, these supports are removed mechanically (probing) or by melting the supports [101]. Batch processing compatible temporary supports have been developed that can be removed in oxygen plasma after the sacrificial layer etch [102]. Another method is termed liquid bridge cleavage, in which devices can be designed so that the last remaining droplets during

evaporation are concentrated near the strong supporting structures of the movable structure instead of the weakest portion of the movable structure [103]. This minimizes the impact of capillary pull. Various schemes exist that are based on dry etching the sacrificial layer. This eliminates the collapsing force since there is no liquid present during drying. One of these techniques involves the replacement of the sacrificial layer with a plastic that can be etched using oxygen plasma [102]. Other methods are employed that bypass the traditional evaporation drying cycle. Two variations are freeze-sublimation drying and supercritical drying. In freeze-drying the rinse solution is first frozen and then exposed to a heated vacuum environment. The solid turns directly to vapour, which eliminates the capillary pull since there is no liquid state present. This was first applied to MEMS devices in [104]. One disadvantage is that the rinse solution can experience significant volume expansion during freezing which can permanently deform the structures. This can be minimized using liquids that expand little when frozen. This process is now rarely used, in favour of the more successful supercritical drying technique [88]. In this technique, the rinse solution is replaced by liquid CO_2 at elevated pressures inside a high pressure chamber. The liquid CO_2 is then heated to a supercritical fluid. There is no interface formed during this transition. The chamber is then vented at a constant temperature above the critical temperature. The CO_2 exits in gaseous form. During evaporation of the supercritical carbon dioxide, no liquid-vapor interface exists, so there are no capillary forces working.

Methods that reduce surface energy include increasing the surface roughness and reducing the contact area. Increasing surface roughness dramatically reduces adhesion because the van der Waals force is expected to be extremely sensitive to surface roughness. A tenfold reduction of the adhesion energy can be obtained [89]. This procedure also has the benefit that it can often be accomplished without a complete redesign of the structure, requiring a tailoring of the fabrication process. Another method to reduce the surface energy is to reduce the contact area. In many instances, early in the design, stiction reducing bumps can be added into the layout [105]. These bumps are placed to significantly reduce the contact area of the movable structure and the adjacent structure. This technique is very simple, but suffers from two drawbacks. First, it cannot be applied in all situations, and second, the adhesion of the bumps is often larger than anticipated [88].

Simultaneous solutions that eliminate capillary pull and reduce surface energy come in the form of low surface energy, hydrophobic coatings that have become very popular in combating the stiction problem. The reason for their popularity is that in many cases they are able to simultaneously reduce the surface energy as well as make the surface hydrophobic, which eliminates the capillary pull during drying. This is the only solution that tackles both problems simultaneously. One example of these coatings is referred to as self-assembled monolayers (SAMs), since they form a single layer of adsorbed molecules on the surface. These molecules can be tailored to adsorb on a wide range of surfaces, including metals and semiconductors. The head group can be tailored to adsorb to the desired substrate while the tail group points away from the substrate. The tail group can be terminated with appropriate molecules depending on the application. These monolayers have also been shown to be very useful in reducing friction and wear [106].

For the capacitor structures presented in Chapter 3, drying using a low surface tension liquid (ethanol) was tried on nickel structures with no success. The majority of cantilever beams showed stiction after the removal of the sacrificial layer. Also, an attempt at applying a monolayer of dodecanethiol to nickel structures was performed. The thiol was applied to the capacitors immediately after the HF etch, before the devices were dried. Thiols have been observed to make metal surfaces hydrophobic and significantly lower surface energy. This eliminates stiction during drying and actuation. Thiols have not been adequately investigated on nickel MEMS devices and this is not a mature technique. The problem with nickel lies in the oxide layer which reduces the quality of the formed monolayer [96,107]. This test was unsuccessful and stiction was observed after drying and during actuation. Removal of the oxide layer before the application of the monolayer should be employed in future tests.

One issue with the methods that solely reduce or eliminate the capillary pull during drying is the fact that these devices may become stuck during use, if accidental contact is made, which is possible for some structure types including the capacitors presented in Chapter 3. For this reason, either surface energy reduction techniques or a surface coating appear to be possible solutions to the stiction problem for these devices. During etching and testing of the pull-away style capacitors it was noticed that certain devices do not stick once they have collapsed onto the electrode. This was only observed in a few devices and is not

consistent across samples. It is believed that some devices make better contact than others, therefore some stick while others do not. Based on these observations, a reduction in area during contact seems to be a promising technique for the elimination of stiction during both fabrication and actuation.

This could be achieved by adding small bumps to either the cantilever sidewalls, or electrode sidewalls, or both. For vertically oriented beams fabricated using the LIGA process, these bumps can be simply incorporated as a feature on the mask. This produces bumps that run the full height of the beam, or electrodes and allows for the precise control of their geometry. In planar processes, the incorporation of these bumps typically requires an additional lithography step and their shape can be process limited by planar layer thickness. The required size and spacing of these bumps can be determined from beam length calculations using the peel number equations presented above. When the beam collapses, these bumps maintain a gap distance equal to the size of the bumps. The beam can then be approximated as a fixed-fixed (doubly supported) beam with a length equal to the spacing between the bumps and a gap distance equal to the size of the bumps. The peel number equation for a fixed-fixed beam then gives a good indication as to whether a beam of this length will stick if contact is made.

Lengths of fixed-fixed beams at the peel bound (onset of sticking) ($N_P = 1$) are shown in Figure 4.3 for beam widths (w) ranging from 2.5 to 20 μm. Four lines are shown corresponding to nickel and gold beams with gap distances (bump sizes) of 0.5 and 1.0 μm. The surface energy γ_s of gold is 1540 mJ/m^2 [97] and the elastic modulus E of bulk gold is 78 GPa [49]. The residual stress σ_R was set to 0.

From the figure it is clear that nickel beams can be longer than gold beams without sticking. Nickel has a higher surface energy, but also a significantly larger Young's modulus, which makes it less prone to sticking. In the remaining work it can be assumed that no beams will be fabricated with a width smaller than 5 μm. Therefore, if both nickel and gold structures are to be fabricated, the spacing between bumps should be made at most 80 μm if 0.5 μm bumps are used and 113 μm if 1.0 μm bumps are used.

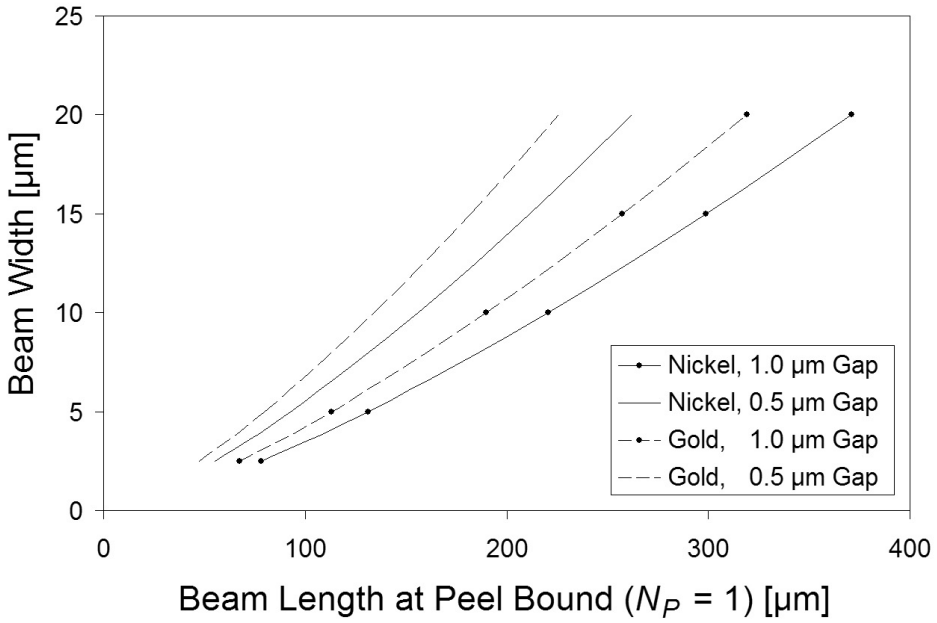

Figure 4.3: Lengths of fixed-fixed beams at the peel bound ($N_P = 1$).

4.2 Structures for the Determination of Surface Energy

As shown in the previous section, one of the important material property parameters when designing microstructures is the surface energy γ_s. This parameter is useful when analysing structures to determine if the structures will stick during fabrication or device operation. In the proposal for this research it was suggested that a set of test standards to determine the surface energy could be investigated, similar to the structures presented in [108], but modified for thick electroplated metal layers.

An example of these structures is shown in Figure 4.4. The technique involves fabricating beams of known geometry and increasing length. In this case an array of polysilicon cantilever beams was constructed. During the wet removal of the sacrificial layer, the devices come into contact with the substrate due to the large capillary forces present during drying. In the dry samples, adhesion forces hold the beams against the substrate with a characteristic interfacial surface energy γ_s. The length of the longest beam that is detached is proportional to the magnitude of this surface energy. Using this method, relatively accurate values of the

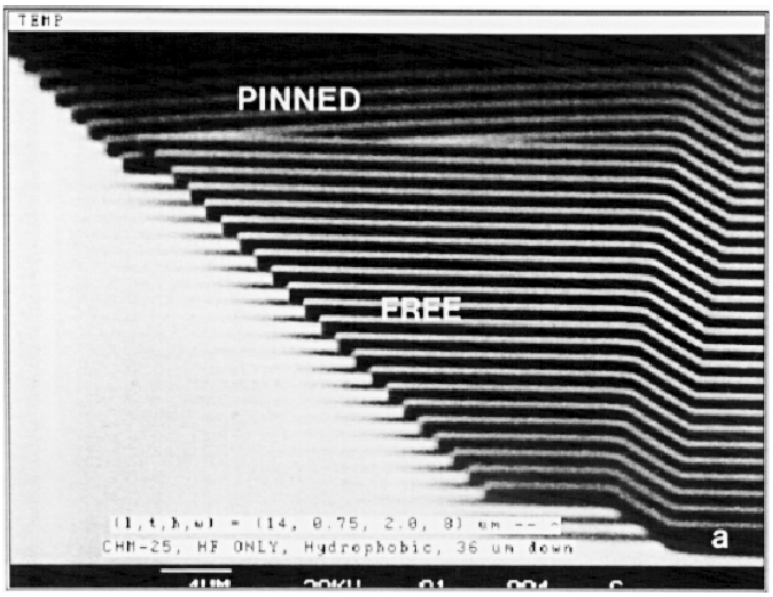

Figure 4.4: Polysilicon cantilever beams of increasing length. The shorter beams are free from the substrate and the longer beams are pinned to the substrate with the transition signifying the peel bound (reproduced from [88]).

surface energy can be determined that provide the designer with some insight into the types of structures that can be built free of stiction.

Upon further investigation, this technique is not applicable to the metal beams found in this work. The reason for this can be seen in Figure 4.2. In the figure for nickel (top), beams that have a length equal to the peel bound do not touch during drying, only longer beams do. Phrased differently, the shortest beam to touch during drying will stick, but beams shorter than this would stick if they came into contact. Therefore, this technique, used with metal structures, would only yield information as to which beams came into contact during the drying process. In the figure for PMMA (bottom), beams shorter than the peel bound would touch during drying, however only beams longer than the peel bound would remain stuck after the structures were dry. Therefore, PMMA stuctures could be used with this technique.

With metal beams, these shorter beams that don't touch during drying could be possibly forced to make contact using a different method such as mechanically (probing) or using an

electrostatic force. This was not investigated as mechanically actuating these beams would be unreliable. Also, the voltage required to electrostatically actuate peel bound length beams is very large and the breakdown of air at these voltages could be possible, which will be shown in a following section. For the peel bound length nickel cantilever beam example with dimensions; $l = 173$ μm, $w = 10$ μm, $d = 5$ μm, and $h = 100$ μm, the pull-in voltage would be approximately 1,000 V using the theoretical pull-in voltage equations presented earlier.

4.3 Mechanical Material Properties

As discussed in Chapter 3, the bending characteristics of the measured devices match quite well with that predicted by simulation, considering that the simulation results include approximated high-frequency parasitic capacitance effects. However, the measured pull-in voltage values are considerably smaller than the values predicted by simulations using bulk material properties. For the large nickel devices, the measured pull-in voltage is approximately 20.0 V compared to 25.6 V predicted by simulations and for the small gold devices the measured pull-in voltage is approximately 7.8 V compared to 9.3 V predicted by simulations.

In Chapter 1 it was shown that the mechanical properties of thick electroplated layers used in the fabrication of microstructures often differ from bulk values and are dependent on process parameters such as bath types, temperatures, currents, plating areas, etc. In this case, bulk mechanical properties predict a higher pull-in voltage, therefore the magnitude of Young's modulus in the fabricated devices is likely smaller. A set of test structures called VM-TEST was developed to determine the important mechanical material properties of thick electroplated layers including Young's modulus E and the residual stress σ_0. These structures were presented in [109] and a discussion of the structures is given in Chapter 7.

4.4 Tuning Ratio

The maximum tuning ratio for the pull-away style variable capacitors, as shown in Chapter 3, was 1.36:1 for the small gold half capacitance electrode (e7) device. Some applications require only a small tuning ratio to fine-tune an impedance value, most applications require a ratio of at least 2:1 [2]. Conventional solid-state varactors made from silicon or gallium arsenide using either p-n or Schottky-barrier junction structures typically feature tuning ratios of 2:1

to 4:1 including parasitics. A high aspect ratio MEMS capacitor structure fabricated using DXRL with a significantly increased tuning ratio over the pull-away variable capacitors is discussed in Chapter 6. This device uses the principle of leveraged bending and places the capacitance electrode on the same side of the beam as the actuation electrode. Using this approach, the tuning ratio is significantly increased and the device features similar large Q-factors as the pull-away variable capacitors.

4.5 Reduction of Actuation Voltage

The reduction of actuation voltage has been an important topic in MEMS design since the integration of these devices with integrated circuits has been one of the major goals. Electrostatically actuated devices typically require actuation voltages that are significantly larger (20 - 80 V) than the voltages used in integrated circuits ($<$ 5 V). While the direct operation of MEMS devices at lower voltages would be optimal, a common approach has been to include circuitry to increase the voltage level to that required by the MEMS devices. An example of this approach is found in the WiSpry^{TM} antenna tuner for handsets chip (WS2018) mentioned in Chapter 1. This device provides impedance optimization using digitally tunable MEMS capacitors. It compensates for antenna source impedance changes due to the need to operate over different frequency bands as well as to compensate for antenna load changes that are caused by hand, head and other body effects. The chip can be driven using an existing supply as the high voltage (35 V) charge pump for electrostatic actuation is fully integrated on the same die as the MEMS variable capacitor elements.

To reduce the actuation voltage in future designs, an adjustment of the gap shape was performed and the results were presented in [110]. By changing the gap shape the actuation voltage can be reduced by as much as approximately 40% for cantilever beams and 30% for fixed-fixed beams. A detailed description of the gap shapes and procedure is presented in Chapter 6.

4.6 Other Challenges

The following challenges have been thoroughly covered in [19] and will be briefly discussed in the following sections.

4.6.1 Stress Concerns

The stress levels present in the device during actuation must be examined. In general the stress should be kept at a minimum. The larger the stress during actuation, the fewer number of cycles the device will be able to tolerate before failure.

Nickel tensile specimens were fabricated and analyzed [41] to determine their strength and high-cycle fatigue performance. Based on these findings, the tensile strength was found to be approximately 600 MPa, the yield strength approximately 370 MPa and the fatigue strength (endurance limit) of approximately 195 MPa.

Nickel cantilever and fixed-fixed beams were analyzed using ANSYS with geometries ($w = 6$ μm, $d = 6$ μm, $l = 1000$ μm) similar to the devices found in this work [19]. They were analyzed with and without the large rounding (30 μm radius) where the beam attaches to the stationary support structure. For cantilever beams without a rounded attachment point, the maximum stress intensity (for a 2 μm displacement) was found to be approximately 3.4 MPa. For the fixed-fixed beam without rounded corners the value was approximately 8 times larger at 26.3 MPa. Both values are significantly smaller than the endurance limit found in [41], and should perform quite well during small deflections.

Rounding the attachment points resulted in similar stress intensities, but a reduction in the stress component in the direction perpendicular to the beam by a factor of approximately 7. Most importantly, there is no large stress component near a sharp corner that could propagate tiny cracks, which would cause the device to fatigue prematurely.

In all cases the stress levels were well below the 195 MPa endurance limit for LIGA nickel. This does not suggest that the selection of geometry for a MEMS device is arbitrary. Steps must be taken to reduce the stress levels, especially the elimination of sharp corners where tiny cracks can propagate and cause the device to fail prematurely. In addition, the stress in the polymer resist that results due to expansion and shrinkage during development, must

be taken into account. Sharp corners in the tall polymer structures will crack or possibly lift from the substrate. Therefore, there should be no sharp corners in the MEMS device at all if possible. This includes components of the MEMS device that are not involved in actuation. A rounding radius of 1 or 2 μm for static corners is usually adequate.

4.6.2 Breakdown of Air at Micrometer Separations

MEMS devices that feature electrostatic actuation often require large voltages applied between electrodes, which are often spaced by only a few microns. The MEMS designer needs to know how large of a voltage can be applied, before the air between the electrodes breaks down and allows current to pass in the form of a spark.

It is commonly believed that if the voltage between two electrodes in atmospheric air is below the Paschen minimum breakdown voltage of approximately 325 V, then a breakdown between the electrodes is not possible [111].

Measurement data [111] reveals that for gaps greater than 4 μm the breakdown voltage is in the range of 300 - 400 V, and is consistent with Paschen's law. For gaps less than 4 μm the breakdown voltage is smaller than the values predicted by the Paschen curve and is a function of the separation of the electrodes. Experimental data suggests the breakdown voltage falls between 65 V/μm and 110 V/ μm for gaps up to 4 μm wide. The breakdown of air at micrometer separations is very similar to the breakdown of vacuum at small separations and suggests a similar breakdown mechanism may govern both cases. Since the mean free path of the electrons in air at atmospheric pressure is about 4 μm, the presence of air in very small contact gaps will only have a small effect on the breakdown process [111].

For the MEMS designer, this data reveals that one must be careful to avoid designs that require actuation voltages that are large enough to cause breakdown. During actuation of MEMS devices the gap becomes smaller as the voltage is increased. Therefore, the maximum voltage and the smallest gap size are the two most important parameters. From the data presented above, a value of 65 V/μm should not be exceeded to be on the safe side. This linear relationship is only valid for gaps smaller than 4 μm. For larger gaps Paschen's law provides accurate information.

4.6.3 Beam Deflection due to Acceleration

Gravity will cause the beam to deflect. This is a potential problem if the deflection of the beam is significant. If gravity causes the capacitance to change by a significant amount then the orientation of the capacitor becomes important. This is not a desirable characteristic since this device should be able to perform adequately regardless of its physical orientation. Accelerations other than gravity will also cause the beam to deflect. The capacitor should also be able to perform under a wide range of accelerations. The device should not be limited to stationary operation.

For example, a nickel cantilever beam with $l = 1000$ μm, $w = 10$ μm, and $h = 100$ μm placed on its side (for maximum deflection) will have a deflection due to gravity g of 0.006 μm at the beam tip. A fixed-fixed nickel beam with similar dimensions will have a deflection due to gravity of 0.0001 μm at the beam center. The density used for the calculations was 8.902 g/cm^3 [49] with bulk mechanical properties ($E = 207$ GPa, $\nu = 0.31$) [49].

Assume the beam is used as one electrode in a capacitor with an air gap of 1 μm. For the cantilever beam, the deflection due to gravity is 0.57% of the overall gap. The change in capacitance will be approximately 1/3 of the tip deflection, approximately 0.19%. This number could be significant depending on the application. For the fixed-fixed beam, the deflection due to gravity is 0.012% of the overall gap. The change in capacitance is approximately 0.004%, which is not likely significant regardless of the application.

Alternatively the required acceleration can be calculated for a beam deflection of 3% (0.03 μm) of the gap. The associated change in capacitance will be approximately 1%. For the cantilever beam configuration, the acceleration required is 5.2 g. For the fixed-fixed beam configuration the acceleration required is 251.8 g. In comparison, the acceleration during a space shuttle launch is 2 - 3 g. A fighter jet is capable of 8 - 9 g. The deflection of the cantilever beam can become significant during large accelerations. Accelerations capable of a significant deflection of the fixed-fixed beam are not likely to be encountered.

5. Layout and Fabrication Challenges

This chapter gives a brief overview of the layout that was created to address some of the challenges that were discussed in Chapter 4. The high aspect ratio beams and gaps found in these structures make fabrication non-trivial. Therefore, some of the general challenges encountered when fabricating deep X-ray lithography masks and samples featuring structures with these dimensions are also discussed.

5.1 Layout

The layout that was created to address some of the challenges discussed in Chapter 4 is shown in Figure 5.1. The layout has been divided into a grid for easier discussion. The following is a brief overview as to the different structures found in the layout. Structures presented in the remainder of this work will be discussed first, followed by a brief description of the remaining structures not covered in this work as well as supporting structures used in the fabrication process.

The devices in coordinate C2 are leveraged bending capacitors with increased tuning ratio and will be discussed in detail in Chapter 6. There are 12 devices in total and they differ by size (3) and anti-stiction measures (4). The small devices have beams 1000 μm long, beam widths of 5 μm and an actuator air gap width of 5 μm. The medium devices have beams 1200 μm long, beam widths of 6.5 μm and an actuator air gap width of 6 μm. The large devices have beams 1400 μm long, beam widths of 8 μm and an actuator air gap width of 7 μm. The capacitance gaps for all devices were scaled according to the actuator air gap size. The four different anti-stiction measures are bumps attached to the electrodes in two different sizes (0.5 and 1.0 μm) and large triangles that protrude from the electrodes the same distance as the bumps (0.5 and 1.0 μm).

The devices in coordinates A(1,2), F(1,2) and H(1,2) are structures for determining mechanical material properties. These structures will be discussed in detail in Chapter 7. Each coordinate set contains 16 cantilever beams and 16 fixed-fixed beams of varying lengths. The six coordinate sets vary in anti-stiction measures (3) and whether or not the beams

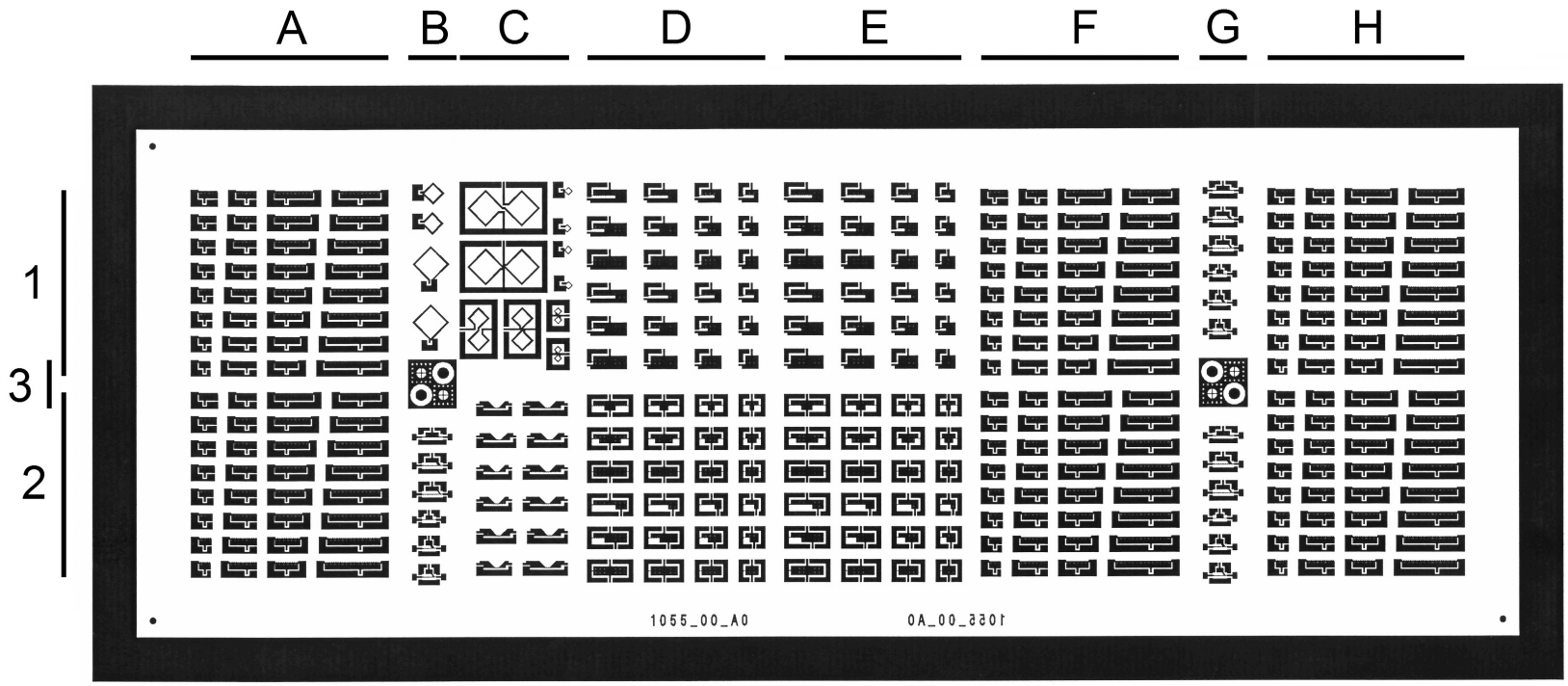

Figure 5.1: Mask layout.

have periodic widening on the side opposite to the actuator electrode (2). The anti-stiction measures are 1.0 μm bumps (F1,H1), 0.5 μm bumps (F2,H2) and 1.0 μm triangles (A1,A2). Structures with periodic beam widening are (A2,H1,H2) and those without are (A1,F1,F2). Only the devices with 1.0 μm bump anti-stiction measures will be discussed in the following chapters as these measures proved to be the most reliable.

The devices in coordinates D(1,2) and E(1,2) are modified pull-away style variable capacitors. Both cantilever and fixed-fixed beam structures in four sizes were designed including structures smaller than the structures presented in Chapter 3. Anti-stiction measures have been incorporated along with full, 2/3 and 1/3 length capacitance electrode designs. Some of the cantilever devices feature a modified layout with smaller ground structures for lower parasitics and higher performance. These structures require testing and characterization. The devices in coordinates B2 and G(1,2) are high aspect ratio RF MEMS series microswitches. They differ in size (2) as well as actuation electrode design (3) and contact area design (3). These structures also require testing and characterization. The devices in coordinates (B,C)1 are micromachined inductors fabricated for another researcher.

The structures found in coordinates (B,G)3 are used for alignment, which is necessary if the structures on the mask are to be aligned to a substrate that has been previously patterned. Portions of the mask membrane inside the alignment structures are etched away, making these areas optically transparent so that alignment is possible. Also visible in Figure 5.1 are small structures in three of the corners of the mask. These structures are translation rings that can be used to monitor the extent of the mechanical translation present during the exposure. These structures will be discussed in greater detail in a following section.

5.2 Mask Fabrication Challenges

The fabrication process for creating titanium membrane X-ray masks consists of first constructing an intermediate mask and then transferring this pattern into a working mask which can be used to pattern the thicker PMMA templates that are used to electroform the final structures. The titanium membrane mask fabrication process is thoroughly discussed in [12, 112, 113].

The intermediate mask is created by e-beam writing the layout pattern into 3 - 4 μm of

PMMA situated on top of a 2 - 3 μm thick sputtered titanium carrier layer. The titanium layer is sputtered on top of a silicon wafer coated with a 100 nm carbon layer as an anti-adhesion film to facilitate the release of the titanium layer. The developed resist template is electroplated with approximately 2 μm of gold. The resist is stripped, then the wafer is glued to an Invar support frame. Finally, the titanium membrane supporting the gold X-ray absorber pattern is released from the silicon wafer.

The intermediate mask pattern is then transferred into a working mask using soft X-ray lithography. The working mask starts off similar to the intermediate mask except a resist layer of approximately 30 μm is used. This resist template is then electroplated with gold to a height of approximately 20 μm. Similar to the intermediate mask, the resist is stripped, the titanium membrane is glued to an Invar frame, then the membrane with gold absorbers is released from the silicon wafer.

The following discussion illustrates the complexity of the mask fabrication process and one of the challenges that was encountered when attempting to fabricate a working mask based on the layout described in the previous section. During the intermediate mask electroplating process, significant gold underplating was observed beneath the resist structures that are meant to define the air gaps in the fabricated devices. Example images of a fabricated intermediate mask are shown in Figure 5.2. Gold underplating can be seen in the air gaps of both large (Figure 5.2(a)) and small (Figure 5.2(b)) devices. Around the beam tip, in both images, the pitted rough darker surface of the oxidized titanium layer can be seen. In the large device, the lighter gold underplating is seen on both edges of the large gap, but not in the center of the gap. In the small gap the underplating appears to cover the whole gap. In the small device, the underplating appears to cover both large and small gaps.

When this intermediate mask is transferred using soft X-ray lithography into a working mask, the resist in the small gaps is not adequately removed in the development process as the exposure dose in these areas was not large enough due to the significant amount of gold. This leads to incomplete electroplating in the areas that feature unwanted resist. An example of this is shown in Figure 5.3, which is a working mask test sample (03671_01). These figures depict the start of the gold electroplating on the working mask. The height of the gold is approximately 100 nm. On the large device, plating starts on both the small and

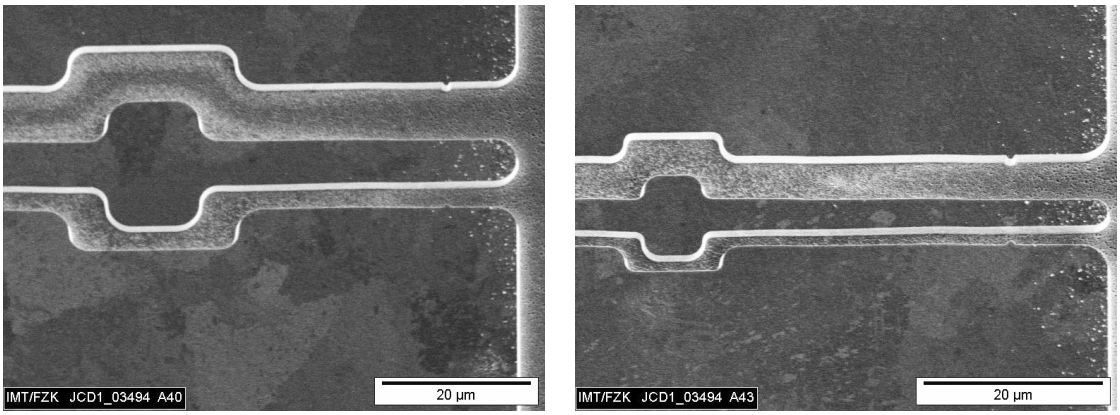

(a) Large Device (b) Small Device

Figure 5.2: SEM images of intermediate mask (03494). Images show the beam tips of large and small capacitor devices and the unwanted gold underplating in the gaps.

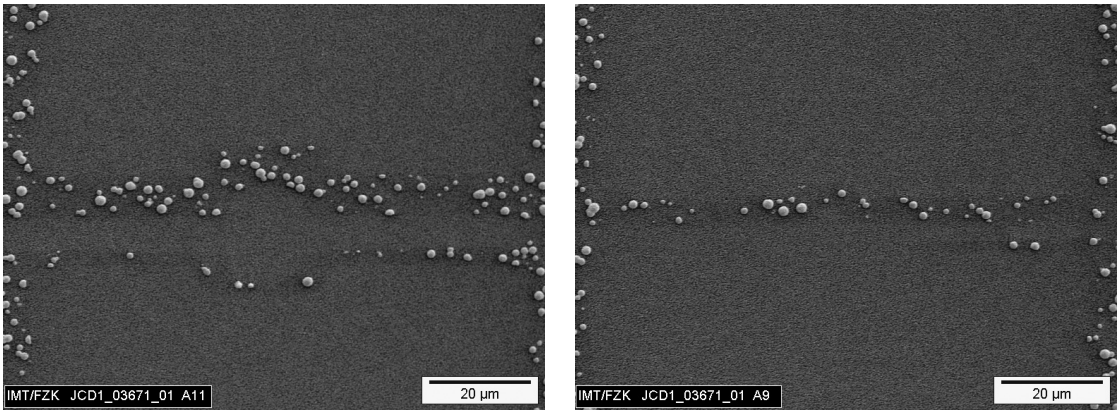

(a) Large Device (b) Small Device

Figure 5.3: SEM images of working mask test sample (03671_01) with approximately 100 nm of electroplated gold. Images show the beam tips of large and small capacitor devices.

large gaps, but on the small device there is no plating on the small gap.

After electroplating the working mask (03630) to a height of approximately 25 µm, as shown in Figure 5.4, voids in the gold absorber structures meant to define the air gaps in the final devices can be seen due to incomplete resist development. Visible in the small gap of the large device is incomplete electroplating and what appears to be trapped resist. The small device has large portions of the small gap absorbers missing. The images are not the

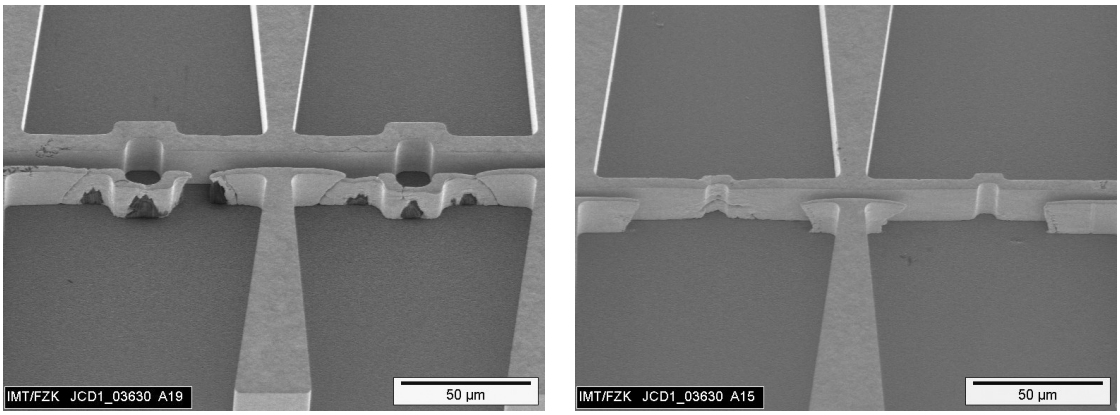

(a) Large Device (b) Small Device

Figure 5.4: SEM images of working mask (03630) with approximately 25 µm of electroplated gold. The incomplete electroplating of the gold absorber structures can be seen.

exact devices shown in Figures 5.2 and 5.3, but have identical size gaps and are expected to have very similar underplating.

Based on these results, the underplating is likely thicker in the smallest gaps of the intermediate mask which would explain why these areas do not properly develop in the working mask, even though there appears to be significant underplating in the large gap of the small device. Later attempts at the fabrication of an intermediate mask were successful by improving the adhesion of the resist with the oxidized titanium. An example of successfully fabricated small and large capacitor devices from working mask 03916 are shown in Figure 5.5.

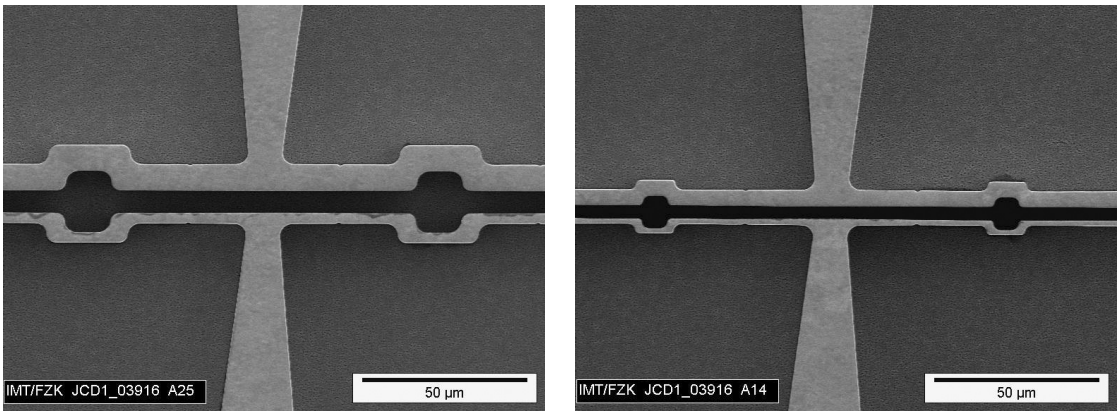

(a) Large Device (b) Small Device

Figure 5.5: SEM images of working mask (03916) with approximately 25 µm of electroplated gold showing the successful fabrication of both large and small capacitor device structures.

5.3 Exposure Challenges

5.3.1 Mechanical Translation

The mechanical translation of the sample with respect to the mask during an exposure is a common issue as the scanner is constantly in motion during the exposure. This translation must be monitored in each sample as the resulting structure quality directly depends on the magnitude of this translation. This is also important when copying an intermediate mask into a working mask as translation during this step is possible as well.

Inside the scanner chamber, the mask and sample are pressed together with a pneumatic force. This force along with the friction between the resist and the proximity spacers on the mask prevents the two from moving in relation to one another. The proximity spacers are used to define the air gap during the exposure. They cycle together vertically though the beam to achieve a uniform radiation dose on the sample. The sample and mask can cycle thousands of times during an exposure that can often last for hours depending on the thickness and type of resist. It is not uncommon for the two to move in relation to one another during this process.

To monitor this, auxiliary structures called translation rings can be added to the layout, as was done in the layout in Figure 5.1. Concentric rings are placed in three of the four

corners on the mask. They are placed in the corners as it helps to isolate them from mask membrane thermal expansion effects, which will be discussed in the next section. After exposure and development of the sample, the rings on the sample are inspected and the circularity of the rings can be used to determine the extent of the translation during the exposure.

Example images of bottom left corner translation rings can be seen in Figure 5.6. These images were acquired using an optical microscope with an attached camera. To determine if translation occurred a circle is drawn using measurement software into the inner ring and the two are compared. Figure 5.6(a), from sample 03704, shows minimal translation as the rings are very circular. In this image translation is not detectable. Figure 5.6(b), from sample 03701, shows significant translation as the inner ring is elongated with respect to the reference circle. From the measurement values on the image, the magnitude of the translation can be estimated to be approximately 6 µm. The magnitude of the translation in this image is not typical, however this method can be used to identify translation problems greater than approximately 1 µm using an optical microscope, a camera and appropriate aquisition and measurement software.

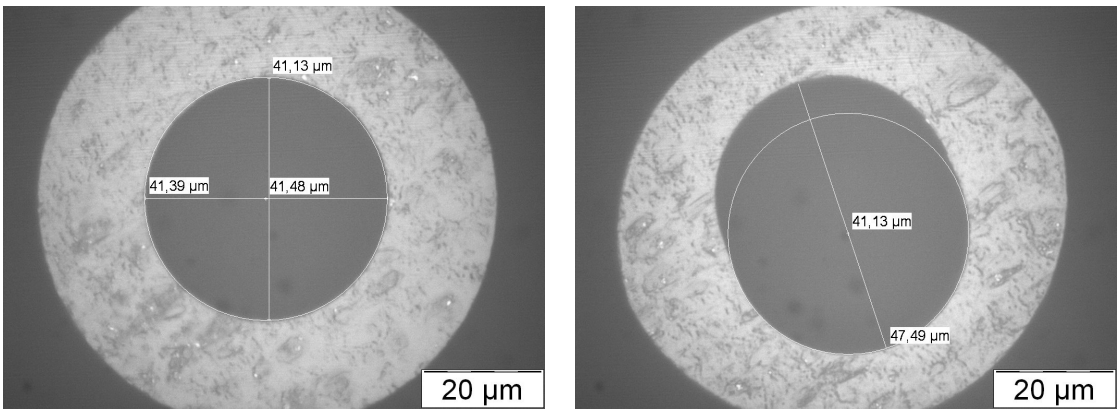

(a) Minimal Translation (03704)

(b) Significant Translation (03701)

Figure 5.6: Optical microscope images of translation rings.

5.3.2 Mask Membrane Thermal Effects

As mentioned previously, the titanium membrane X-ray masks are fabricated with a very thin (2 - 3 μm) titanium carrier membrane with thicker gold absorbers (≈ 20 μm) electroplated on top. The membrane is attached to a cooled Invar frame. This membrane and the gold absorbers heat significantly as the beam passes over them during a scan [113,114]. This causes them to locally expand, then contract, during each scan pass, which can cause significant deformations in the transferred image. The beam homogeneously irradiates the mask in the horizontal direction. Vertically the beam is a few millimeters high therefore scanning is required, which imparts the most significant thermal distortion into the vertical direction with the maximum deformation amount located in the center of the mask.

An example of a structure showing thermal distortion is shown in Figure 5.7. For this exposure, the sample (03710) was rotated 90° from normal in the scanner so that the beam and gap lengths were oriented vertically rather than horizontally. This was done to minimize the thermal distortions of the beam and gap widths, which are the most sensitive dimensions in the layout. Figure 5.7(a) is an image of the bottom left translation ring for this sample in 150 μm of PMMA. No significant translation is visible in the image signifying that the mask and sample did not move with respect to each other during the scan. Figure 5.7(b)

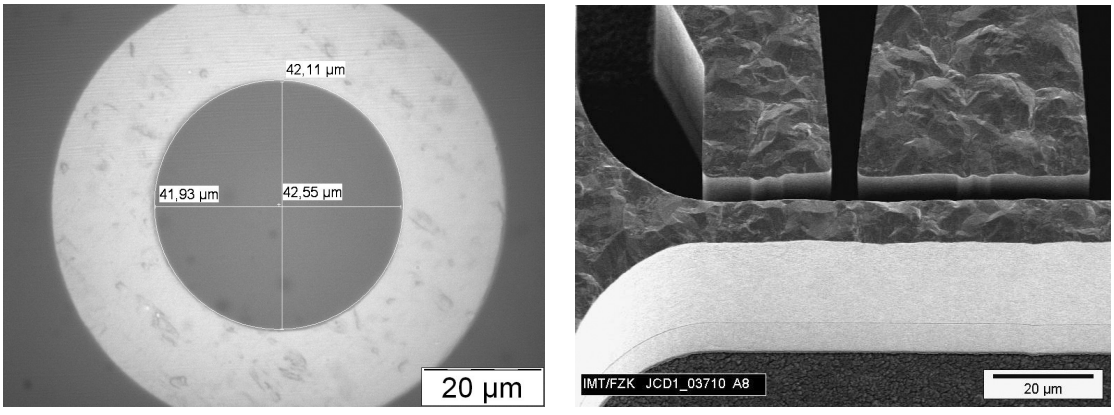

(a) Minimal Translation (03710) (b) Significant Thermal Distortion (03710)

Figure 5.7: Images from sample 03710 showing no translation effects but significant thermal distortion.

is an image of a structure for determining mechanical material properties in 100 μm of electroplated nickel. In the image it is clear that two anti-stiction bumps are present in each location that contains only one on the mask. This was caused by significant thermal distortion in the vertical direction during the scan.

Sample rotation to reduce distortion is only possible if the critical dimensions in the layout lie in only one direction. In this case, these dimensions can be oriented so that they are least distorted. Other methods to reduce thermal distortion, in general, involve reducing the beam power that impinges on to the mask and the sample. This reduction in thermal distortion can be achieved, to a certain extent, by reducing beam power and increasing exposure time. There are multiple methods to reduce the beam power including reducing the source energy or current, increasing the mirror angle, beam chopping and the use of pre-filters. Increasing the mirror angle softens the spectrum by removing higher energy photons. The mirror angle is typically tailored to the resist thickness since higher energy photons are required for thicker resists. The most practical method to reduce beam power is beam chopping. A chopper is a mechanical device that rotates and periodically blocks (absorbs) the incoming beam. This causes the beam to be pulsed in time, which reduces power, but maintains the spectral profile. The percentage of the time that the beam is on, is inversely proportional to the required exposure time. Pre-filters inserted into the beam path remove the lower energy photons and harden the spectrum. This method also slightly reduces beam power, but this technique is typically used to lower the exposure dose at the top of the resist where the lower energy photons are absorbed.

5.4 Etching

Initial etching tests to remove the approximately 3 μm thick titanium seed layer, electrically isolating the structures and releasing the thin beams, were performed using 5% HF acid. This etchant was created by diluting concentrated 48% HF acid to 5% by volume with de-ionized (DI) water. Although this technique was successful, it was found to be hard to control as the etch times were too short and significant etching underneath the nickel structures (underetching) was common. Also, on occasion, the short etch times would not be sufficient for the etchant to properly penetrate the gaps and fully remove the titanium

seed layer present in these narrow trenches. This resulted in electrically shorted structures.

An improvement was made by etching these structures with HF acid diluted to 1%. This increased the etch time, but allowed the etchant more time to penetrate into the narrow trenches and remove the titanium material in the gaps. With the minimum time required to fully remove the titanium material in the gaps, the 1% HF etchant showed less underetching than the 5% in the other more open areas.

A further improvement for etching structures with narrow trenches was found by diluting the 48% HF acid to 10% by volume with isopropyl alcohol (IPA). The lower surface tension of the IPA was found to quickly and evenly penetrate the narrow gaps. It was also found that a much higher HF concentration was required for an adequate etch rate when the HF was diluted using IPA. In addition, a pre-soak in pure IPA then a direct transfer into the etchant was beneficial as this helps draw the etchant into the gaps in the etch step. More detailed information on this procedure as well as comparison images between the different methods can be found in [115]. A pre-soak in DI water would also likely be beneficial for the 5% and 1% HF etchants diluted using DI water. In all cases, the structures were rinsed in DI water after the etch step.

Based on these findings, 5% HF is recommended for sacrificial layer removal that is not time critical. HF diluted to 1% is recommended for time critical etching without the presence of any narrow trenches or other areas where it would be hard for the etchant to penetrate. An example of this would be seed layer removal to electrically isolate structures where minimal underetching is required. HF diluted to 10% using IPA is recommended for structures featuring high aspect ratio trenches or holes etc., where the etchant would have a difficult time to penetrate. Holes or trenches with aspect ratios of 10:1 or greater would benefit from using this technique.

5.5 Dimension Comparisons

The following discussion illustrates how the dimensions of the sample might change throughout the fabrication process. These dimensions are given as one example, which is not necessarily typical or optimal. As mentioned previously, the sequence for device creation is: layout, intermediate mask, working mask, final sample. The intermediate mask number is

03494, the working mask is 03630 and the sample is 03704, all of which were fabricated at IMT.

To analyze the dimensions, 32 line and space measurements were taken in both vertical and horizontal directions for each fabrication step. The same measurement locations were used throughout the process. In the vertical direction, beam and gap widths were measured and in the horizontal direction the support triangle width and the spacing between triangles was measured. Table 5.1 shows the average difference between the 32 measurement points, in μm, across the layout as fabrication progresses. These measurements were taken with an optical microscope fitted with a camera and image capture and measurement software. On the masks, the electroplated gold structures were measured and on the samples the developed resist structures were measured.

The measurements show a difference between the layout and the intermediate mask of approximately 1 μm. The lines on the layout increase by approximately 1 μm and the spaces decrease by approximately the same amount. The difference between the working mask and the intermediate mask is quite small. The difference in the vertical direction is negligible and a slight horizontal difference suggests a possible small horizontal translation during the exposure. The transfer from intermediate mask to working mask shows that virtually identical mask copies are possible if the translation is minimal and the thermal effects are negligible. The transfer from the working mask to the sample is quite accurate with a dimension change of less than 1 μm. In this sample, no translation can be observed using the translation rings. The larger vertical than horizontal difference suggests a possible slight vertical translation and/or thermal effects. Throughout the overall process, from layout to final sample, the lines increase by approximately 1.4 - 1.7 μm and the spaces decrease by approximately the same amount.

Table 5.1: Dimension comparison through the fabrication process. The values listed are the average of the differences between values measured across the samples. IM = Intermediate Mask and WM = Working Mask.

Dimension Type (IM,WM,Sample)	Avg. Δ Between IM (03494) & Layout [μm]	Avg. Δ Between WM (03630) & IM (03494) [μm]	Avg. Δ Between WM (03630) & Layout [μm]	Avg. Δ Between Sample (03704) & WM (03630) [μm]	Avg. Δ Between Sample (03704) & Layout [μm]
Vertical Dimension (line,space,line)	0.79 $\sigma = 0.21$	-0.04 $\sigma = 0.25$	0.75 $\sigma = 0.20$	0.67 $\sigma = 0.35$	1.42 $\sigma = 0.28$
Vertical Dimension (space,line,space)	-0.84 $\sigma = 0.20$	-0.04 $\sigma = 0.23$	-0.88 $\sigma = 0.24$	-0.67 $\sigma = 0.30$	-1.55 $\sigma = 0.26$
Horizontal Dimension (line,space,line)	0.79 $\sigma = 0.14$	0.56 $\sigma = 0.35$	1.36 $\sigma = 0.27$	0.36 $\sigma = 0.35$	1.71 $\sigma = 0.20$
Horizontal Dimension (space,line,space)	-1.02 $\sigma = 0.11$	-0.37 $\sigma = 0.19$	-1.40 $\sigma = 0.17$	-0.34 $\sigma = 0.27$	-1.74 $\sigma = 0.36$

5.6 Sample Comparisons

This section is a comparison of four samples fabricated at different institutes using working mask 03630. This is not every sample prepared as part of this work, but a small subset for comparison purposes. They are the most accurate samples prepared to date at each location using mask 03630 except for sample 03710. This is not meant as a comparison between institutes, as time spent and sample numbers prepared at different locations varies greatly. Also each institutes sample is not necessarily optimal for that facility, just an example of the type of dimensions that are possible. The exposure parameters for the four samples are listed in Table 5.2.

Samples 03704 and 03710 were fabricated at IMT in Karlsruhe, Germany. Sample CAMD-1 was fabricated at the Center for Advanced Microstructures and Devices (CAMD) in Baton Rouge, Louisiana. Sample SYL-00120 was fabricated at the Synchrotron Laboratory for Micro and Nano Devices (SyLMAND) at the Canadian Light Source (CLS) in Saskatoon, Saskatchewan. Sample 03704 was a low power exposure done on beamline Litho 1 with a mirror angle of 15.4 mrad as noted by the long exposure time of 6 hours and 25 minutes. Also note that the scan velocity was reduced to 2 mm/s for this exposure due to translation problems likely associated with the long exposure durations. Sample 03710 was a higher power exposure done on beamline Litho 2 with a mirror angle of 4.85 mrad. To minimize the distortion of the beam and gap widths, both sample and mask were rotated by 90° during the exposure. Sample CAMD-1 was exposed on XRLM1 and SYL-00120 was exposed at SyLMAND with a mirror angle of 8 mrad and a 25% chopper setting.

A comparison of the dimensions of the four samples is given in Table 5.3. These values are the average of the difference between the sample and the working mask in μm. Sample 03704 was discussed previously and is a very accurate transfer with a dimension change less than 0.7 μm. In this sample no translation can be observed using the translation rings. The larger vertical than horizontal difference suggests a possible slight vertical translation. Sample 03710 has minor dimension change (< 0.9 μm) in the vertical direction on the sample, but significant change in the horizontal direction (≈ 3 μm). No translation is detectable using the rings. Since the sample was rotated 90° during the exposure this represents significant

Table 5.2: Exposure parameters for samples exposured at IMT, CAMD and SyLMAND using working mask 03630.

Sample	03704 (IMT)	03710 (IMT)	CAMD-1 (CAMD)	SYL-00120 (SyLMAND)
Resist Thickness [μm]	100	150	160	100
Seed Layer	Ti/TiO_x	Ti/TiO_x	none	none
Substrate Material	Alumina	Alumina	Si	Si
Substrate Thickness [μm]	1000	1000	500	500
Beamline	Litho 1	Litho 2	XRLM1	SyLMAND
Electron Energy [GeV]	2.5	2.5	1.3	2.9
Magnetic Field [T]	1.5	1.5	1.5	1.35
Bottom Dose [kJ/cm^3]	3.5	3.5	4	4
Top Dose [kJ/cm^3]	unknown	5.8	11.4	7.1
Dose Ratio	unknown	1.7	2.9	1.8
Dose Curr. [mA min/cm]	10633	510	3116	2000 (500)
Mirror Angle [mrad]	15.4	4.85	none	8.0
Chopper	none	none	none	25%
Sample Rotation	none	90°	none	none
Filter	none	40 μm C	42 μm C	125 μm Kap.
Kapton on Resist [μm]	50	125	25	25
Scan Velocity [mm/s]	2	40	20	20
Scan Acceleration [mm/s^2]	200	400	200	200
Beam Curr. [mA]	148 - 104	160 - 155	138 - 116	145 - 132
Exposure Time [min]	385	30	104	88

Table 5.3: Dimension comparison of sample exposures done at IMT, CAMD and SyLMAND using working mask 03630. The values listed are the average of the difference between the sample and the working mask. WM = Working Mask.

Dimension Type (WM,Sample)	03704 (IMT) [μm]	03710 (IMT) [μm]	CAMD-1 (CAMD) [μm]	SYL-00120 (SyLMAND) [μm]
Vertical Dimension (space,line)	0.67 $\sigma = 0.35$	0.87 $\sigma = 0.32$	0.29 $\sigma = 0.31$	1.29 $\sigma = 0.33$
Vertical Dimension (line,space)	-0.67 $\sigma = 0.30$	-0.74 $\sigma = 0.28$	-0.38 $\sigma = 0.23$	-1.22 $\sigma = 0.27$
Horizontal Dimension (space,line)	0.36 $\sigma = 0.35$	3.04 $\sigma = 1.02$	1.02 $\sigma = 0.32$	2.16 $\sigma = 0.24$
Horizontal Dimension (line,space)	-0.34 $\sigma = 0.27$	-3.16 $\sigma = 0.95$	-0.72 $\sigma = 0.15$	-1.70 $\sigma = 0.12$

thermal effects. The standard deviation for these values is also significantly larger, suggesting that it is very location dependent as is expected with thermal effects. Sample CAMD-1 is also a very accurate transfer with a small dimension change (< 0.4 μm vertical, ≤ 1 μm horizontal). A very slight horizontal translation is noticeable when examining the translation rings for this sample. Sample SYL-00120 has considerably more dimension change in both the vertical and horizontal directions, with significant translation noticeable in both directions when examining the translation rings for this sample. The magnitude of the translation, based on translation ring measurements, is approximately 1.5 μm. Work is ongoing at SyLMAND to reduce this translation error. Further exposures at IMT on Litho 2 were improved with the use of a chopper. Samples with chopper settings of 12.5% and 25% showed more accurate values in the vertical direction (horizontal if rotated 90°) on the sample due to reduced thermal effects.

6. Leveraged Bending Variable Capacitors

6.1 Theory

In this chapter, the theory, design, fabrication and testing details are presented for a high aspect ratio variable capacitor that is suitable for fabrication with the LIGA process and features a considerably increased tuning ratio over the pull-away style variable capacitors. The device incorporates a capacitance electrode on the same side of the vertical beam as the actuator electrode and relies on the principle of leveraged bending to increase the displacement of the thin beam and increase the capacitance tuning ratio. A consequence of the increased tuning ratio, is an increase in the required actuation voltage. Also presented is a method to reduce the pull-in voltage in future designs by adjusting the shape of the actuation gap.

A simplified 3-D view of a vertical, high aspect ratio cantilever beam is shown in Figure 2.2(a) on page 29. It is composed of two metal structures, a cantilever beam and a fixed electrode. The fixed electrode is attached to the substrate and remains stationary. The cantilever beam is not attached to the substrate, but is instead anchored to the larger metal piece on the left that is attached to the substrate. The cantilever has length l, height h and width w. The cantilever and the fixed electrode are separated by an air gap that has a distance d. A DC bias voltage is applied between the beam and the fixed electrode, which causes the beam to displace towards the electrode. A top view of the cantilever beam is shown in Figure 2.3(a) on page 30. This figure shows the beam above the electrode, opposite from Figure 2.2(a), but the operating principles are the same for both configurations. The coordinate system used in the remainder of the chapter is also shown in Figure 2.3(a).

Simulations of the cantilever beam shown in Figure 2.2(a) were performed using the ANSYS Multiphysics simulator with parameters listed in Table 6.1. The mechanical property values listed are for bulk nickel [49]. Simulations of beam displacements just before pull-in are shown in Figure 6.1. With a full actuator electrode from $0 \leq x \leq 1400$ μm, the beam tip deflects 3.11 μm just before pull-in at a voltage of 18.16 V. This corresponds to a displacement

Table 6.1: Simulation parameters.

Beam Length (l) [μm]	1400
Beam Width (w) [μm]	8
Air Gap (d) [μm]	7
Young's Modulus (E) [GPa]	207 [49]
Poisson's Ratio (ν)	0.31 [49]

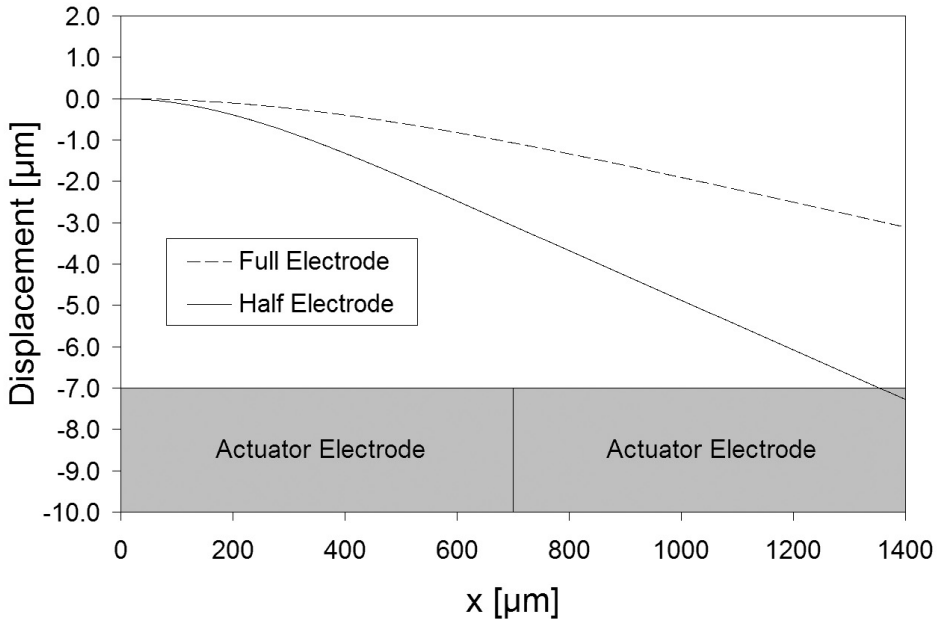

Figure 6.1: Beam displacements and actuator locations for full and half length actuator electrodes.

of 44% of the original gap distance. The capacitance change for this beam configuration is shown in Figure 6.2. The capacitance changes from 0.00179 to 0.00223 pF/μm over this voltage range, which corresponds to a tuning ratio of 1.25:1. The capacitance units are per μm because the simulations are 2-D and have no height. For actual capacitance values, these results should be multiplied by the height. The theoretical equation for the pull-in voltage of a cantilever beam, given in [53, 54] (Equation 2.9, page 34), predicts a pull-in

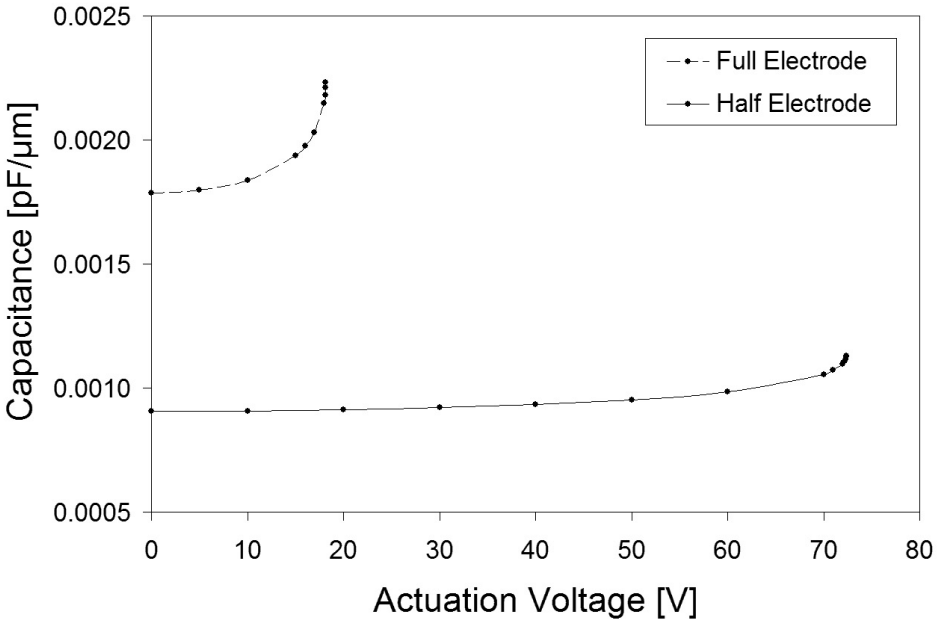

Figure 6.2: Capacitance as a function of actuation voltage for full and half length actuator electrodes.

voltage of 18.19 V as the height, h, approaches infinity. Letting the height approach infinity in the theoretical equations is similar to 2-D simulations, since the 2-D simulations neglect the fringing fields at the top and bottom edges of the beams. The height approaching infinity in the equations also eliminates the effect of top and bottom edge fringing. Using the cantilever beam equation from [59] (Equation 2.11, page 34) a value of 18.37 V is predicted for the pull-in voltage as the height approaches infinity. Both theoretical equations show a percent difference of less than 2% when compared to the simulated results.

If the actuator electrode is made half as long corresponding to $0 \leq x \leq 700$ μm, the beam tip deflects 7.20 μm just before pull-in at a voltage of 72.30 V as shown in Figure 6.1. This corresponds to a beam displacement of 103% of the original gap distance. This principle of achieving larger that complete gap displacements by omitting the portion of the actuator electrode directly by the beam tip in the case of cantilevers, or by the beam center in the case of fixed-fixed beams, is called leveraged bending. The key is that the electrostatically actuated portions of the structure deflect less than the pull-in limit, while other portions of

the structure can move through the entire gap [116]. As shown in Figure 6.2, the capacitance changes from 0.00091 to 0.00113 pF/μm over this voltage range, which also corresponds to a tuning ratio of 1.25:1 similar to the full electrode case. This is expected since with the half electrode configuration, the deflection at the center of the beam just before pull-in is approximately the same as the maximum tip deflection for the full electrode configuration. The use of leveraged bending allows the maximum actuator displacement to be increased significantly by a factor of 2.32, but comes at the cost of an increase in actuation voltage by a factor of 3.98.

Using a device with a half actuator electrode and the principle of leveraged bending allows for the design of a capacitor that has an arbitrarily large tuning ratio. An example of such a device is shown in Figure 6.3. In this configuration, a half actuator electrode is used and a separate capacitance electrode is placed towards the tip of the beam and is given an angled linear shape so that the edge of the beam just contacts the capacitance electrode before pull-in. The device then starts with a finite capacitance defined by the beam

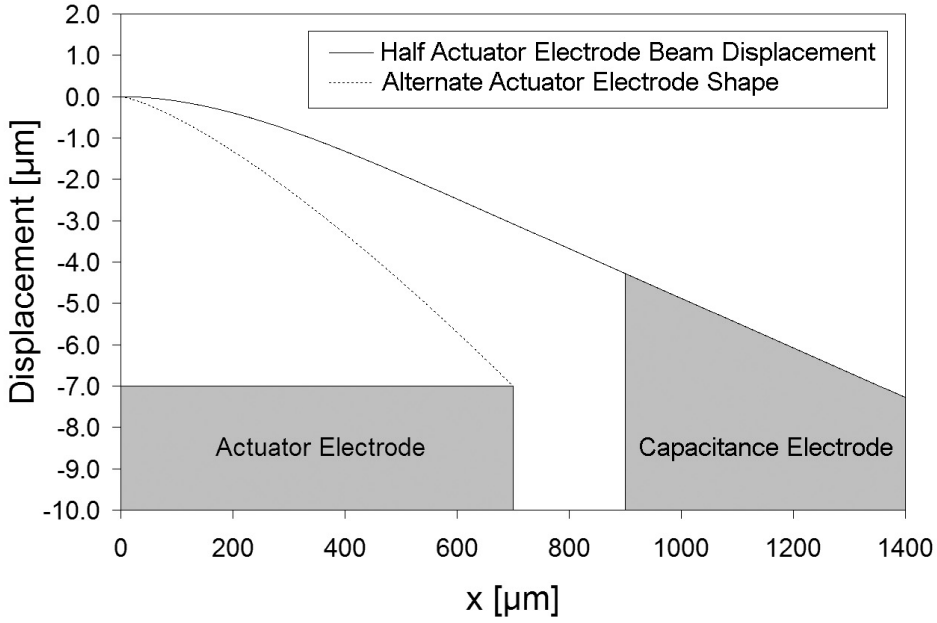

Figure 6.3: Capacitance electrode location and alternate actuator shape that reduces tuning voltage for large tuning ratio design.

and capacitance electrode geometry with no applied actuation voltage. As the actuation voltage is increased, the beam bends stably towards the capacitance electrode and this gap distance approaches zero as the voltage approaches the pull-in voltage. The maximum tuning capacitance would occur just before the beam contacts the capacitance electrode. Contact is undesirable in this structure, for a functional device, as it produces a short circuit between the beam and capacitance electrode. In this case, stops could be added in a functional layout to prevent contact. These test structures are allowed to contact so the full-tuning range can be characterized. For the device presented here, a half actuator electrode was used from $0 \leq x \leq 700$ μm, and the capacitance electrode is situated from $900 \leq x \leq 1400$ μm. With no actuation voltage applied, the actuator electrode has a uniform gap width of 7 μm and the capacitance electrode gap width varies linearly from 4.23 μm at $x = 900$ μm to 7.20 μm at $x = 1400$ μm. Also included in Figure 6.3 is an alternate actuator electrode shape that could be used to further decrease the pull-in voltage. By varying the gap so that the gap distance is proportional to $l^{4/3}$, a reduction in the tuning voltage of approximately 40% can be acheived with a similar maximum deflection. A larger maximum actuator gap than shown here would be required for a similar amount of displacement. These principles are discussed in a following section.

The capacitance change is shown in Figure 6.4. With no actuation voltage applied, the initial capacitance is 0.00082 pF/μm. Initially, increasing the actuation voltage slowly increases the capacitance. As the cantilever beam nears the capacitance electrode, the capacitance increases rapidly as the gap distance approaches zero. Just before pull-in, with 72.33 V applied, the capacitance is 0.04540 pF/μm, which results in a tuning ratio of 55.4:1. The deflection at the cantilever tip is 7.10 μm at this voltage, which corresponds to a distance between the cantilever and the capacitance electrode of approximately 0.10 μm.

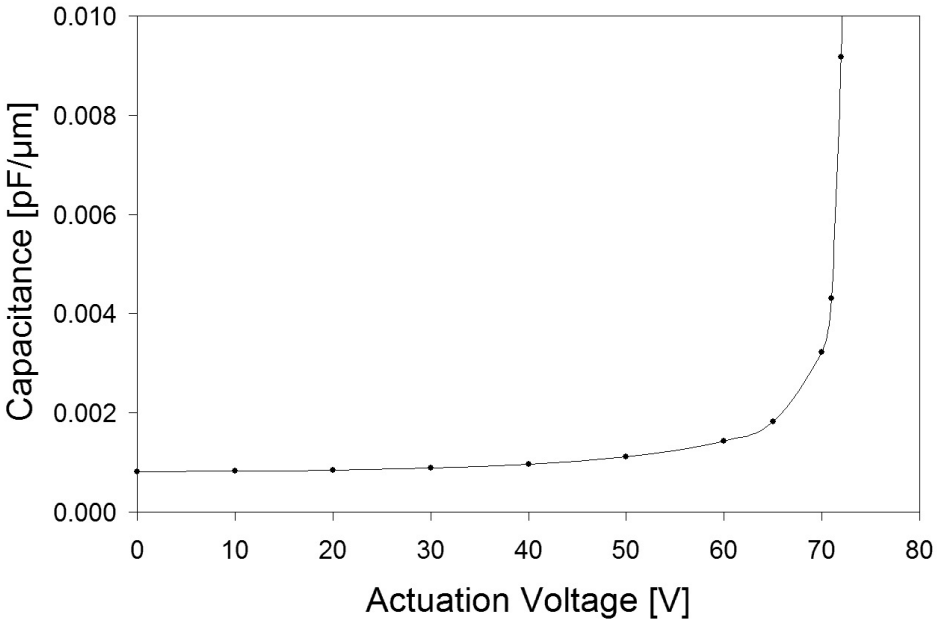

Figure 6.4: Capacitance as a function of actuation voltage for ideal large tuning ratio design.

6.2 Design

The ideal capacitor discussed in the previous section requires auxiliary supporting structures in order for it to survive the fabrication process without suffering severe deformations as discussed in Chapter 3. A layout drawing of the capacitor is shown in Figure 6.5. Three metal structures can be seen in this figure including the actuator electrode, the capacitance electrode and a large ground structure that the thin cantilever is anchored to. Also included are two ports that are included to simplify testing using standard 150 μm pitch wafer probes.

A magnified view of the capacitance electrode is shown in Figure 6.6. The auxiliary supporting structures can be clearly seen in this image. This includes a periodic widening of the beam and triangular voids, which increase the rigidity of the thin PMMA wall that defines the air gap during processing. They also assist in etching the seed layer by allowing the etchant to more freely move into the narrow gaps. Also shown are small anti-stiction bumps attached to the actuator and capacitance electrodes that limit the contact area so that stiction does not occur during fabrication or device operation. Although necessary

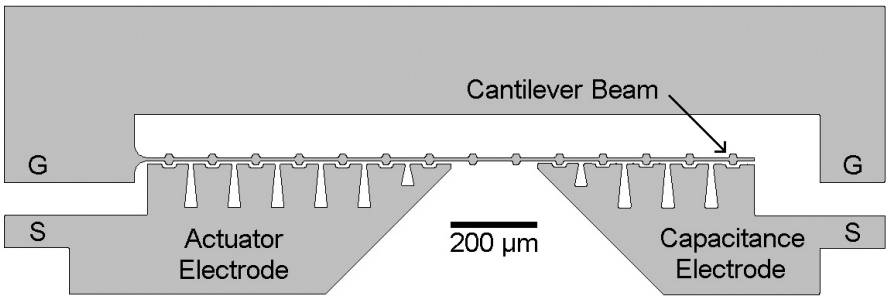

Figure 6.5: Layout drawing of leveraged bending capacitor design.

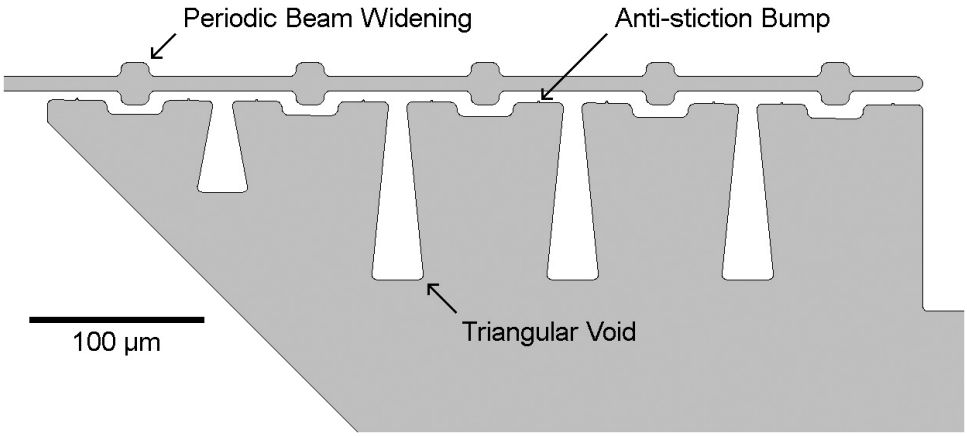

Figure 6.6: Magnified view of capacitance electrode.

for device operation, these auxiliary structures limit device performance by reducing the maximum capacitance and therefore reducing the capacitance ratio.

The dimensions are very similar to the device in the previous section. The beam is 8 µm wide and 1400 µm long. The actuator gap is 7 µm wide and 700 µm long. The capacitance gap varies from 5.23 µm wide at x = 900 µm to 8.20 µm at x = 1400 µm. It was increased in width by 1 µm so that the beam just contacts the anti-stiction bumps before pull-in, which protrude 1 µm from the electrodes. The anti-stiction bumps are placed at a maximum distance of approximately 60 µm apart. The triangular voids are spaced 100 µm apart and are 10 µm wide closest to the beam and expand to 30 µm wide over a distance of 100 µm. The beam widens periodically every 100 µm to a width of 24 µm over a 16 µm length. Also shown in Figure 6.5 is a 30 µm rounding radius where the beam connects to the large ground

structure. This is included to reduce stress at the attachment point during actuation.

This device was simulated using ANSYS Multiphysics electrostatic-structural coupling to obtain the mechanical bending and capacitance change characteristics, as well as Ansoft HFSS to obtain the high frequency electomagnetic characteristics. The capacitor was modelled on a 1 mm thick alumina substrate with a 3 μm titanium seed layer and 100 μm of electroplated nickel with material properties as discussed in Chapter 2. The impedance of the device, as a function of frequency, with no applied actuation voltage is shown in Figure 6.7 and the capacitance change, as a function of voltage, is shown in Figure 6.8.

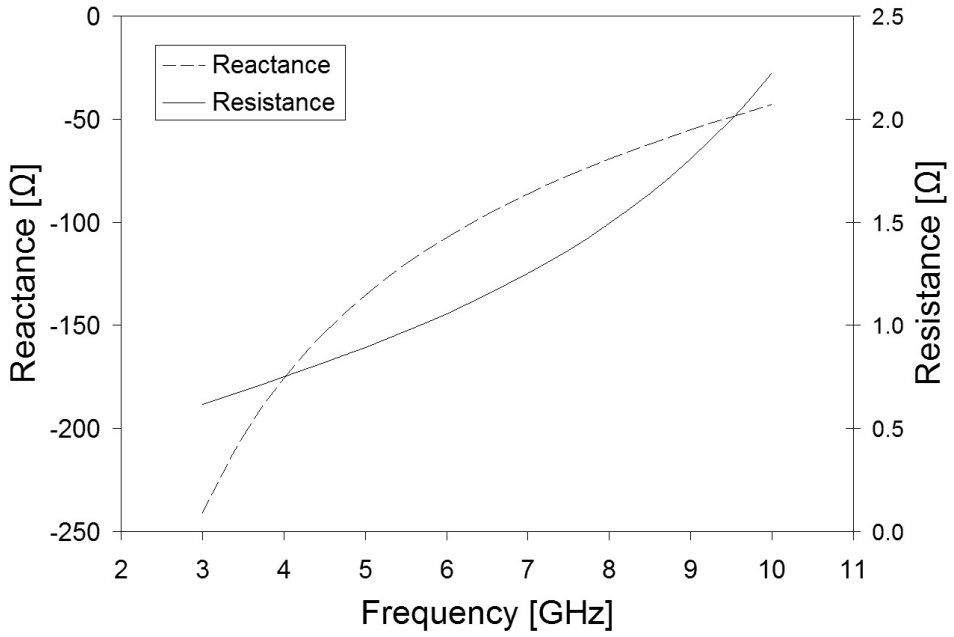

Figure 6.7: Simulated impedance of 100 μm tall nickel, as drawn, leveraged bending capacitor as a function of frequency with no applied actuation voltage.

The reactance of the device varies from 241.0 Ω to 43.0 Ω from 3 to 10 GHz and the resistance varies from 0.62 Ω to 2.22 Ω over the same span. This corresponds to Q-factor values ranging between 391.9 and 19.3. If the reactance is converted to capacitance, the capacitance values are much higher than predicted by ANSYS electrostatic-structural simulation, which is shown in the lower curve of Figure 6.8. This is expected since the ANSYS

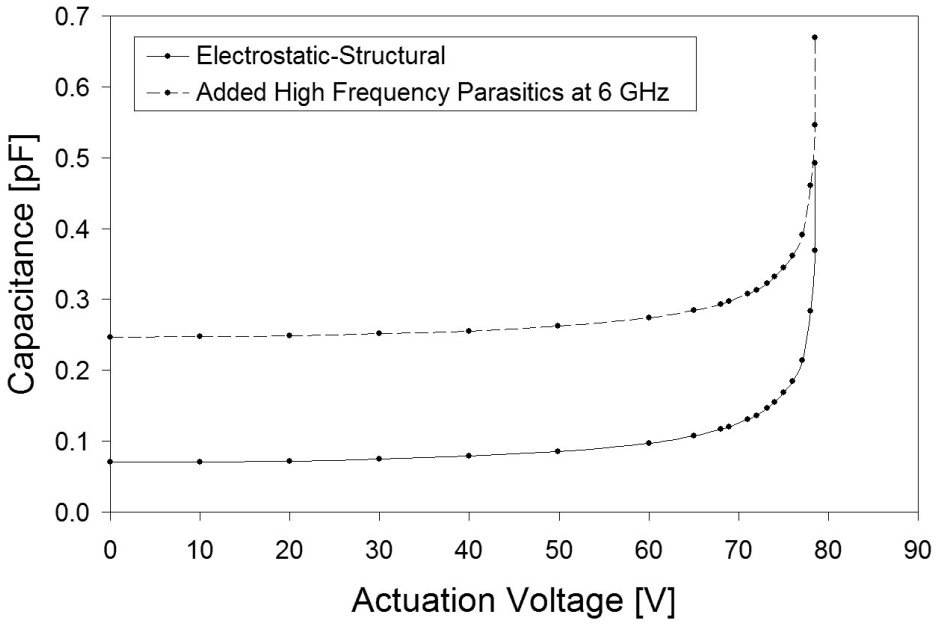

Figure 6.8: Capacitance as a function of actuation voltage for 100 μm tall nickel, as drawn, leveraged bending capacitor. Lower curve shows simulated gap capacitance change and upper curve shows capacitance change with added parasitics at 6 GHz.

simulations only determine the gap capacitance, where as the HFSS simulations are full 3-D electromagnetic simulations that take into account the gap capacitance as well as other high frequency parasitic effects in the device. To model the capacitance change at a particular frequency, the parasitics determined by HFSS can be added to the gap capacitance predicted by ANSYS. The simulated tuning range of the capacitor at 6 GHz is shown in the upper curve of Figure 6.8.

ANSYS electrostatic-structural simulations predict a capacitance change from 0.070 pF to 0.493 pF over a tuning span of 78.55 V. This corresponds to a capacitance ratio of 7.0:1. The tip deflection just before pull-in is 7.10 μm which results in a distance of approximately 0.10 μm between the cantilever beam and the anti-stiction bumps. the actuation voltage has been increased from the ideal case due to the triangular voids which reduce effective area and the periodic beam widening which stiffens the beam.

The parasitic capacitance at 6 GHz was determined to be 0.177 pF, which is the dif-

ference between the simulated gap capacitance and the capacitance extracted from full 3-D electromagnetic simulations. If these effects are taken into account, the capacitance changes from 0.247 pF to 0.670 pF over the same voltage range. This corresponds to a tuning ratio of 2.71:1. The reactance changes from 107.4 Ω to 39.6 Ω and the Q-factor varies from 101.5 to 37.5 Ω based on a resistance of 1.06 Ω.

6.3 Fabrication

The variable capacitor structures were fabricated using the LIGA process at the Institute for Microstructure Technology (IMT) at the Karlsruhe Institute for Technology (KIT). An overview of a 100 μm tall nickel capacitor is shown in Figure 6.9. The layout is identical to the layout discussed in the previous section. A magnified view of the left most portion of the capacitance electrode is shown in Figure 6.10. In this figure, the capacitance electrode can be seen as well as a triangular void in the electrode in the far right of the image. Also in the figure is the capacitance gap, which contains the small 1 μm anti-stiction bumps that are attached to the capacitance electrode. The cantilever beam is also seen including one of the periodically widened sections. Figure 6.11 is an inclined view of the portion of the cantilever

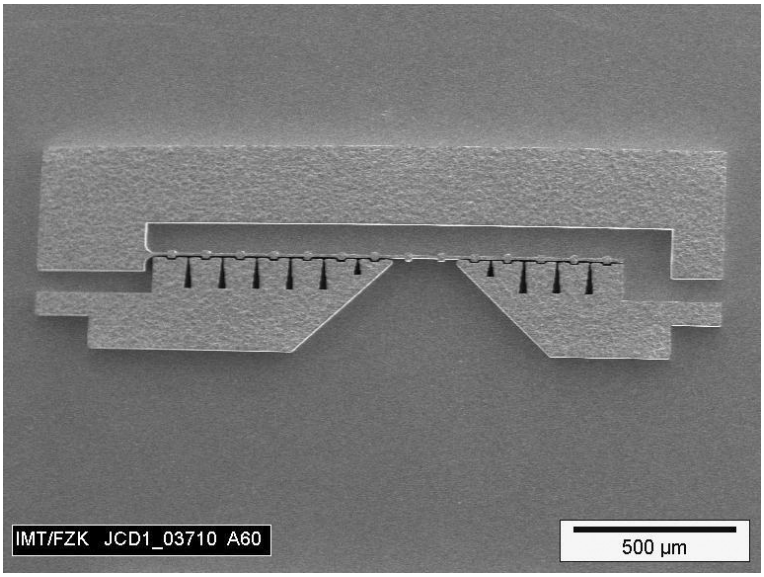

Figure 6.9: SEM overview of 100 μm tall nickel leveraged bending capacitor.

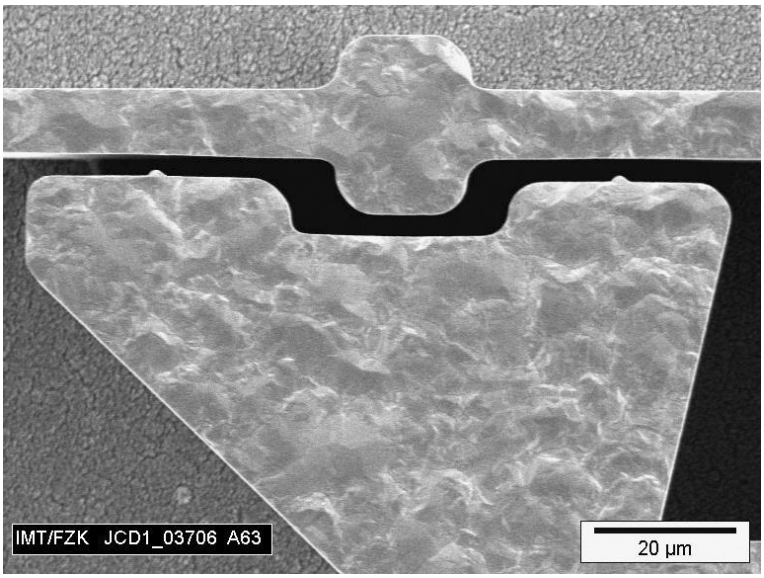

Figure 6.10: Detailed view of a section of the capacitance electrode, capacitance gap, cantilever beam and 1 µm anti-stiction bumps.

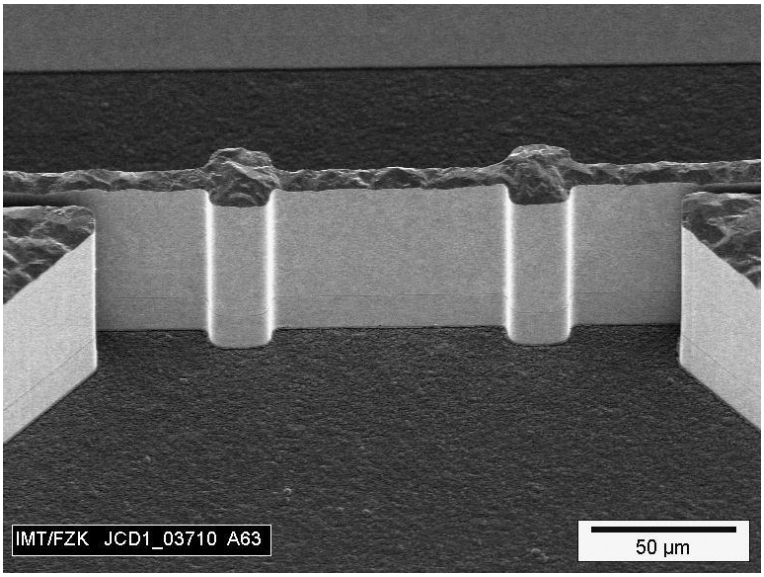

Figure 6.11: Inclined view of portion of cantilever beam between the actuator and capacitance electrodes.

beam between the actuator and capacitance electrodes. The smooth nickel sidewalls can be seen in this figure as well as the rough top nickel surface. Figure 6.12 is a highly magnified view of the bottom of the actuator gap. The actuator is seen on the left of the figure and the cantilever beam is shown on the right. Also visible is the rough oxidized titanium seed layer shown in the bottom of the figure. A line signifying the boundary between the lower glue layer and the upper resist foil is clearly seen on the actuator electrode and also noticeable on the cantilever beam. The thickness of the glue layer based on the figure appears to be on the order of 10 μm.

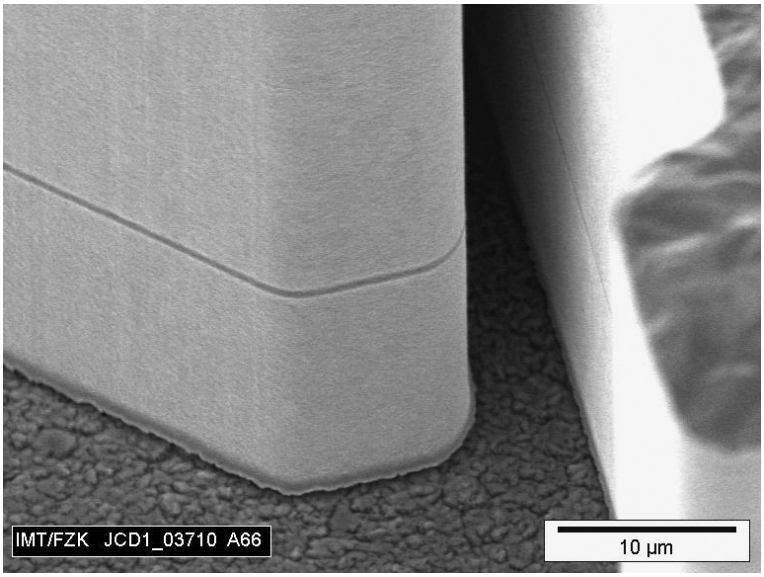

Figure 6.12: Bottom of actuator gap showing actuator electrode (left), cantilever beam (right) and oxidized titanium seed layer surface (below).

To fabricate the capacitor structures a 1 mm alumina (Al_2O_3) ceramic substrate was sputtered with 3 μm of titanium to be used as the electroplating seed layer. The surface of the titanium is then oxidized to Ti/TiO_x using a heated solution of sodium hydroxide (NaOH) and hydrogen peroxide (H_2O_2) diluted in water. This roughens the surface for an effective bond with the glued resist foil. A 150 μm PMMA resist foil is then glued and pressed to the roughened seed layer using a viscous cast resin [12] with properties similar to

the resist foil once hardened.

The resist foil was then exposed to X-rays through a titanium membrane X-ray mask. The exposure was performed at the 2.5-GeV ANKA synchrotron on beamline Litho-2 which incorporates a water cooled nickel coated mirror with a grazing incidence angle of 4.85 mrad to cut off the highest energy photons. Immediately following exposure, megasonic-supported development was performed for 150 min in GG developer at room temperature. The titanium seed layer was then used as a conductive base for 100 μm tall nickel sulfamate microelectroplating. The plating area was 357 mm^2 and the plating current was 1.0 A/dm^2 for a duration of 8 h and 20 min. The remaining resist on the sample was removed by flood exposing the sample and another step of development. The titanium seed layer is then etched in 1% HF for approximately 6 minutes, which electrically isolates the structures, and etches under the thin beam, releasing if from the substrate, while still maintaining good adhesion of the larger metal parts.

Fabricated structure dimensions vary considerably from layout values, which is common as dimensions change from layout to intermediate mask, intermediate mask to working mask, and again from working mask to sample. On average, for this particular sample, the thin beams were found to increase in size by approximately 1.6 μm, while the small gaps were found to decrease in size by the same amount from layout to finished device. For the specific device tested in the following section, measurements show a beam width of 9.53 μm, an actuator gap of 5.47 μm, a small capacitance gap of 3.72 μm at x = 900 μm and a large capacitance gap of 6.52 μm at x = 1400 μm. This compares to an 8 μm beam width, 7 μm actuator gap, 5.23 μm small capacitance gap and 8.20 μm large capacitance gap on the layout.

6.4 Test Results

The fabricated device described in the previous section was tested in the same manner as the pull-away style variable capacitors discussed in Chapter 3. The static impedance measurements for the device, from 3 to 10 GHz, with no applied actuation voltage (0 V), are shown in Figure 6.13. The resistance of the device varies from approximately 0.7 Ω at 3 GHz to 2.3 Ω at 10 GHz. These resistance values are similar to the nickel capacitors presented

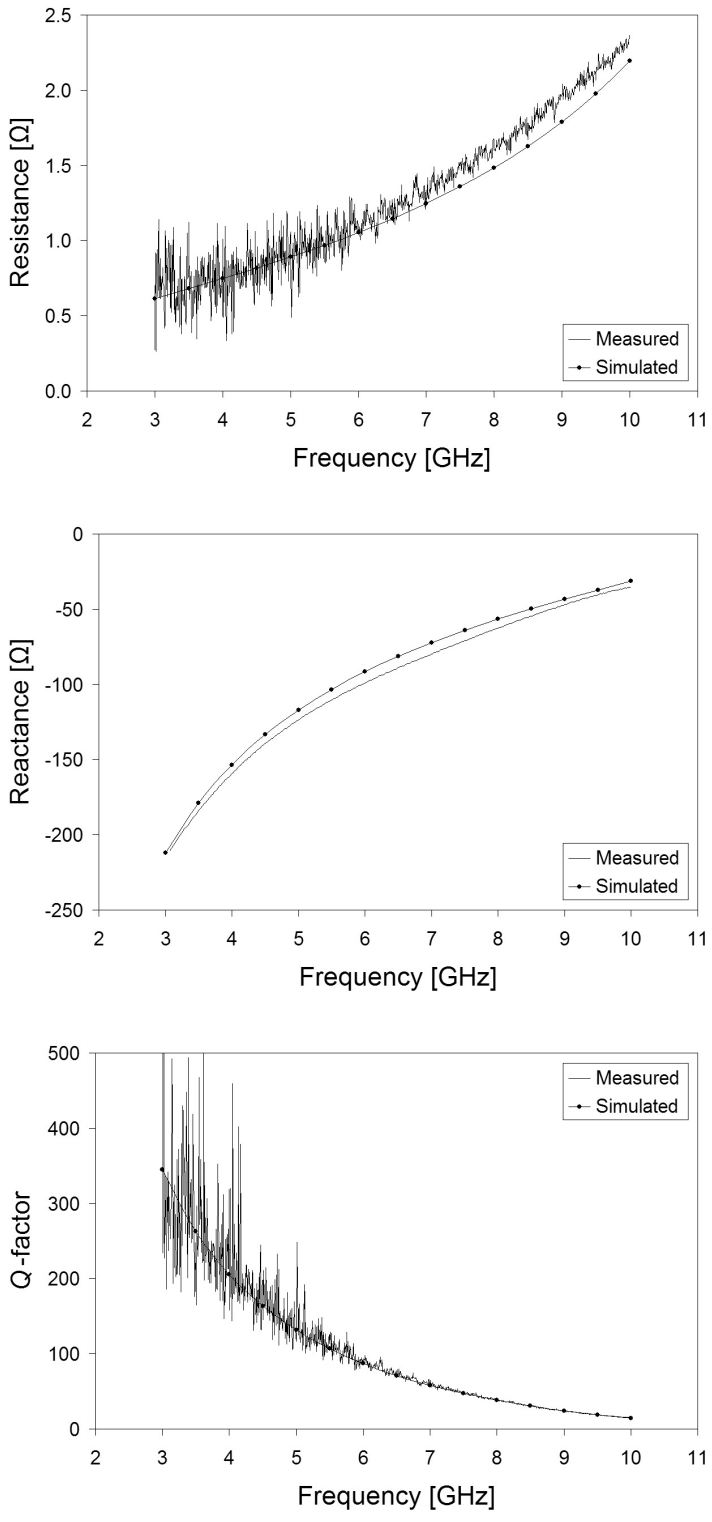

Figure 6.13: Measured and simulated static impedance results for nickel leveraged bending variable capacitor with no applied actuation voltage (0 V).

in Chapter 3, as expected. The reactance varies from approximately 215 Ω at 3 GHz to 35 Ω at 10 GHz which corresponds to a Q-factors from approximately 300 to 15 across the same frequency range. The frequency at a reactance of 50 Ω is 8.8 GHz (0.36 pF) and the resistance is 1.9 Ω corresponding to a Q-factor of 26.

The tuning characteristics of the device at 6 GHz is shown in Figure 6.14. This frequency was chosen as it results in a reactance change from approximately 100 to 50 Ω, instead of the approximately 50 Ω and up as in the pull-away variable capacitor case. At this frequency, the capacitance changes from 0.27 to 0.50 pF over a voltage span of 0 to 63.1 V. This

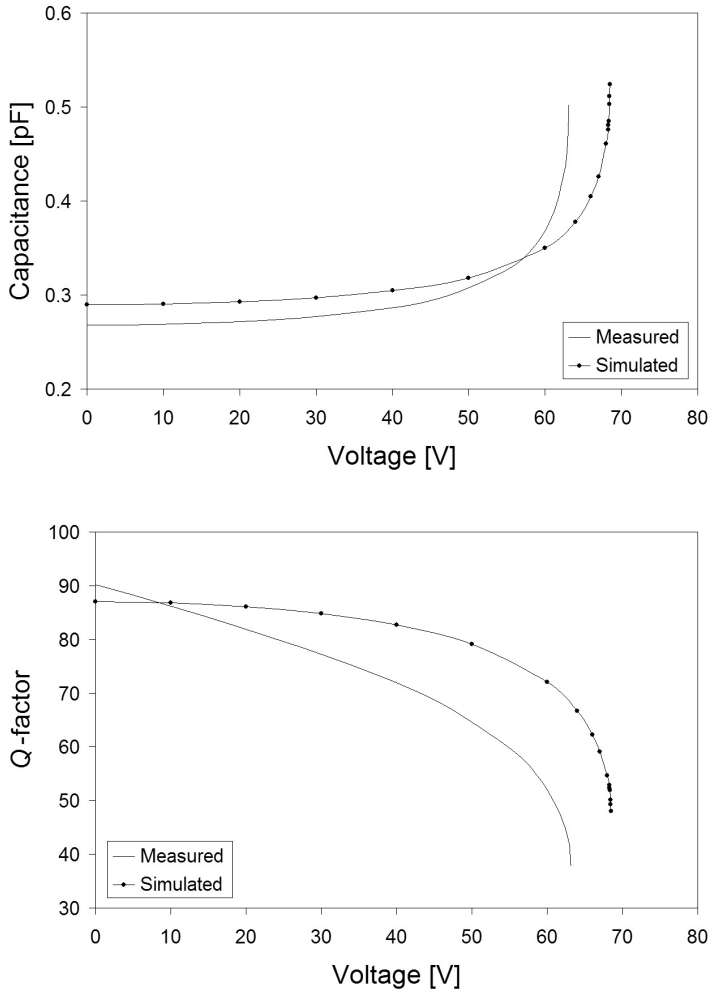

Figure 6.14: Measured and simulated tuning characteristics for nickel leveraged bending variable capacitor at 6.0 GHz.

corresponds to a tuning ratio of 1.9:1. The Q-factor varies from approximately 90 to 38 as the tuning voltage is increased. The simulation results using bulk material properties predict a larger tuning voltage (68.5 V) than the measured voltage similar to the pull-away variable capacitor case. The tuning ratio is significantly smaller than predicted by simulations with ideal dimensions (2.7:1), as the dimension change causes the capacitance electrode and the beam to no longer line up just before contact is made. Simulations show that as contact is made with the first anti-stiction bump at the leftmost part of the capacitance electrode, the gap between the beam and the anti-stiction bump at the rightmost part of the capacitance electrode is approximately 1.1 μm. This could be improved in future designs by simply modifying the capacitance electrode angle in the layout.

In the chapter following, the Young's modulus of this nickel sample was experimentally determined to be 186.2 GPa. Figure 6.15 shows the tuning characteristic if this value is used for simulation instead of the bulk value of 207 GPa. The simulated tuning voltage with $E = 186.2$ GPa is 64.9 V, which differs by only 3% from the measured value.

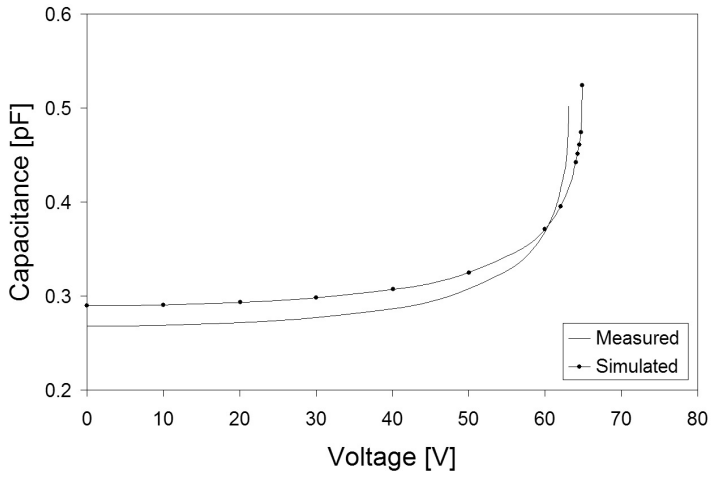

Figure 6.15: Measured and simulated tuning characteristic for nickel leveraged bending variable capacitor at 6.0 GHz. Simulated results use an experimentally determined Young's modulus of 186.2 GPa instead of the bulk value of 207 GPa.

6.5 Reducing Actuation Voltage by Adjusting Gap Shape

6.5.1 Introduction

As shown in the previous sections, the use of leveraged bending has significantly increased actuator displacement, but has also significantly increased the required actuation voltage. In this work [110], a method is presented that can be used in future designs to reduce the required actuation voltage and still maintain the required displacement by adjusting the shape of the gap between the beam and the attracting electrode.

In [116], the authors suggest that varying the gap distance along the length of the beam could be considered to lower actuation voltage, however what particular shapes these gaps should have is not discussed. In [117], the authors present curved electrode cantilever electrostatic actuators with large curvature ($n \geq 2$) capable of very large deflection, but these designs require that either a dielectric insulator or stand-off bumper structures be placed between the beam and the attracting electrode. The beam must contact these structures as deflection occurs, which may not be possible or desirable. Other designs with variable geometry have been presented [118,119], but not with the intention of finding specific shapes to reduce the actuation voltage for a given required displacement.

6.5.2 Problem Description

As discussed previously, vertically oriented (lateral) beams that are perpendicular to the substrate, as shown in Figure 2.2 on page 29, are particularly well suited for realization using DXRL and the LIGA process. One possible advantage to beams oriented in this fashion is that the profile of the gap (the "gap shape") can be easily controlled since it is a feature on the mask. This is considerably more difficult in the planar case, where complex processing steps would be required.

Profile views of the two different beam cases are shown in Figure 2.3 on page 30. This study involves adjusting the shape of the gap (d) as a function of the distance along the beam (x), in order to minimize the actuation voltage for a given required displacement. Beam shapes remain rectangular and as thin as possible to minimize pull-in voltage, but the profile of the gap is changed. Using finite element analysis with the software package

ANSYS Multiphysics, which was verified previously, it is shown that by changing the gap profile, the applied voltage can be reduced and still yield the same displacement.

For this work, a representative problem is described and the gap shape modified to reduce the pull-in voltage. The sample problem features dimensions and material properties similar to that found in other devices in this work. Both a cantilever and a fixed-fixed beam with common dimensions and material properties are investigated. A list of the important values is given in Table 6.2.

Table 6.2: Sample problem parameters.

Young's Modulus (E)	169 GPa
Poisson's ratio (ν)	0.32
Height (h)	100 μm
Length (l)	1000 μm
Width (w)	10 μm
Minimum Gap (d_{min})	1 μm
Required Displacement	2 μm

For both beam types, Young's modulus is 169 GPa, Poisson's ratio is 0.32, the height is 100 μm, the length is 1000 μm (1 mm) and the beam width is 10 μm. The minimum gap is 1 μm, which is assumed to be a limitation of the process for achievable aspect ratios. The required displacement is 2 μm, therefore some part of the beam must move at least 2 μm from its original position. For the cantilever configuration, this is likely to be the beam tip, and for the fixed-fixed configuration, the middle of the beam. This value was chosen as being a reasonable amount of deflection, suitable for many applications, but without unreasonably large actuation voltages. For all models, an initial element size of 0.5 μm was used in the simulations. This was chosen since, in general, the models increase in size over the verification case discussed in Chapter 2.

6.5.3 Required Displacement Constant Gap Case

In this section the gap is increased until the required displacement of 2 μm is achieved before pull-in. This case is also depicted in Figure 2.3 on page 30 with $d(x)$ equal to the constant value required for 2 μm of stable deflection before pull-in. The results are shown in Table 6.3. For the cantilever beam case, the gap width required is 4.56 μm with an actuation voltage of 23.66 V. For the fixed-fixed beam case, the gap width required is 4.99 μm with an actuation voltage of 178.26 V. These results also agree well with the theoretical equations with a maximum difference of 1.24% for the cantilever case and 1.75% for the fixed-fixed case. The results of this constant gap case are compared against the results obtained by varying the gap shape to determine the extent of the decrease in pull-in voltage.

Table 6.3: Constant gap case results (required 2 μm displacement).

Beam Configuration	V_{PI} [V]	Gap Width (d) [μm]	V_{PI} [V] Osterberg Closed-form [53, 54]	V_{PI} [V] Chowdhury Closed-form [59, 60]
Cantilever	23.66	4.56	23.53 (0.55%)	23.37 (1.24%)
Fixed-Fixed	178.26	4.99	175.20 (1.75%)	175.43 (1.61%)

6.5.4 Gap Profiles with Maximum Voltage Reduction

Only the gap profiles in [110] with the maximum reduction in actuation voltage are presented in this section. Complete results and a more thorough presentation can be found in [110].

Cantilever Beam with a Polynomial Gap Profile

For the cantilever beam case, the maximum voltage reduction of the profiles tested was found with an n^{th}-order polynomial function. The gap shape varies according to Equation 6.1. This equation holds except for the regions where this yields gaps smaller than the minimum gap

(d_{min}). In these regions the gap is set to d_{min}.

$$d(x) = d_{max}\left(\frac{x}{l}\right)^n \tag{6.1}$$

The cantilever beam polynomial gap case is shown in Figure 6.16 with $n > 1$. In ANSYS, these curves are implemented as piecewise linear segments with the x-axis divided into pieces of 10 μm length. For each value of n, the maximum gap (d_{max}) was increased until 2 μm of deflection was acheived and the effect on the pull-in voltage was observed. Table 6.4 lists pull-in voltages with the corresponding values of n. This data is plotted in Figure 6.17.

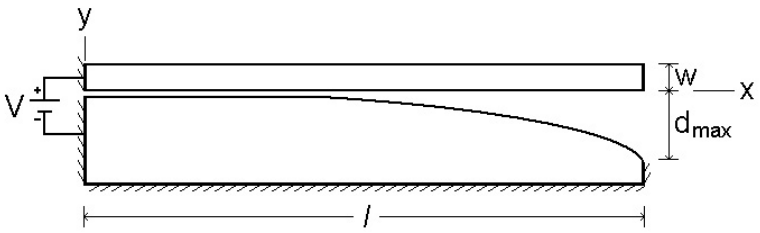

Figure 6.16: Cantilever beam with polynomial gap profile.

In Table 6.4 and Figure 6.17, the value for the linearly varying gap case is included as well, which corresponds to $n = 1$. The pull-in voltage for a linearly varying gap is 14.86 V, which corresponds to a 37.2% reduction from the constant gap case of 23.66 V. The lowest actuation voltage is obtained using a value of approximately $n = 1.3333$. At this point, the pull-in voltage is 14.14 V, which corresponds to a 40.2% reduction from the constant gap case. Values of $n > 1$ give rise to lower pull-in voltages than the $n = 1$ case up until approximately $n = 1.6$, where the values become larger than the $n = 1$ case.

The beam displacement profiles just before pull-in are shown in Figure 6.18. Three different beam profiles are based on the three different gap shapes, which include the constant gap, linear gap, and the $n = 1.3333$ polynomial gap case. The deflection based on the polynomial gap shape has the largest average displacement followed by the linear gap shape and then the constant gap shape.

Table 6.4: Polynomial order and corresponding pull-in voltage for cantilever beam with a required 2 μm of displacement.

n	V_{PI} [V]	Gap Width d_{max} [μm]
1.0000	14.86	4.84
1.1666	14.26	5.17
1.2916	14.15	5.55
1.3333	14.14	5.69
1.3750	14.22	5.88
1.5000	14.43	6.49
1.6666	14.97	7.57

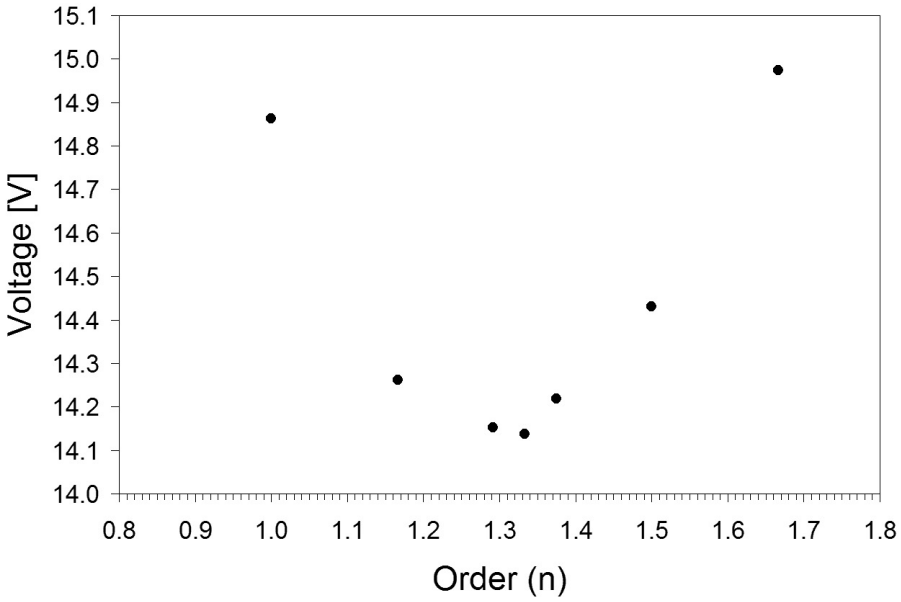

Figure 6.17: Pull-in voltages for cantilever beam polynomial gap case.

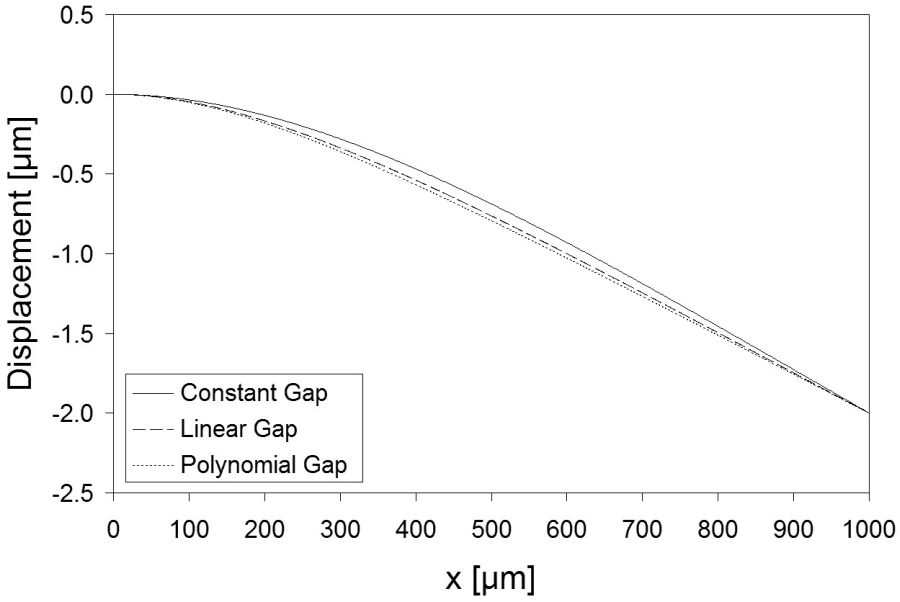

Figure 6.18: Cantilever beam displacement profile.

Fixed-Fixed Beam with a Linear Profile and a Flattened Bottom

For the fixed-fixed beam case, the maximum voltage reduction of the profiles tested was found with a linear profile and a flattened bottom. The beam profile for this case is shown in Figure 6.19.

For each value of d_{flat}, the value of d_{linear} was varied until 2 µm of stable deflection was obtained before pull-in. The value of d_{flat} was increased starting from $y = -6.57$ µm, which is the value required for 2 µm of deflection when $d_{flat} = d_{linear}$, or the linear case without a flattened bottom. The results are shown in Table 6.5 with the first row being the linear case without flattened bottom.

For this case, the actuation voltage is 125.48 V, compared to 178.26 V for the constant gap case, which results in a reduction of 29.6%. The "percentage of triangle removed" column gives the amount the triangle bottom was flattened and is defined as $((d_{linear} - d_{flat})/d_{linear}) \times 100\%$. Viewing these results in Figure 6.20, it is clear that a further reduction in pull-in voltage is possible with a minimum value of 123.94 V, which corresponds to a flat distance of 5.20 µm and a linear distance of 6.65 µm. This ratio results in a triangle with approximately

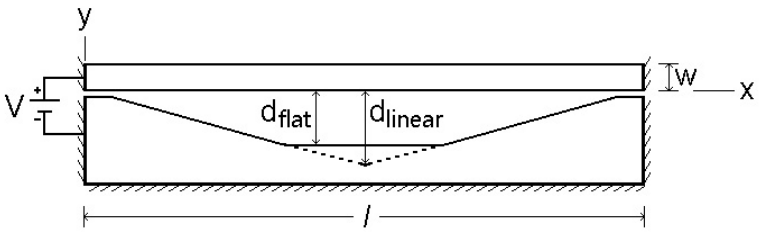

Figure 6.19: Fixed-fixed beam with linearly varying beam profile and a flattened bottom.

Table 6.5: Linearly varying gap with flattened bottom case results (required 2 μm displacement).

Flat Distance d_{flat} [μm]	Linear Distance d_{linear} [μm]	% Of Triangle Removed [%]	V_{PI} [V]
6.57	6.57	0.0	125.48
6.00	6.57	8.7	125.12
5.50	6.59	16.5	124.41
5.25	6.63	20.8	124.02
5.20	6.65	21.8	123.94
5.15	6.66	22.7	123.97
5.125	6.67	23.2	123.98
4.99	6.75	26.1	124.21
4.875	6.85	28.8	124.74

the lower 22% flattened. This gives a reduction in required actuation voltage of 30.5% over the constant gap case.

The beam displacement profiles for the constant gap case, linear gap without flattened bottom and for the minimum voltage case ($d_{flat} = 5.20$ μm) is shown in Figure 6.21. Larger average displacements are seen in the modified gap shape cases over the constant gap shape. Also, the average displacement of the beam with the flattened bottom is slightly lower than the linear gap case, which is due to the increase in d_{linear}.

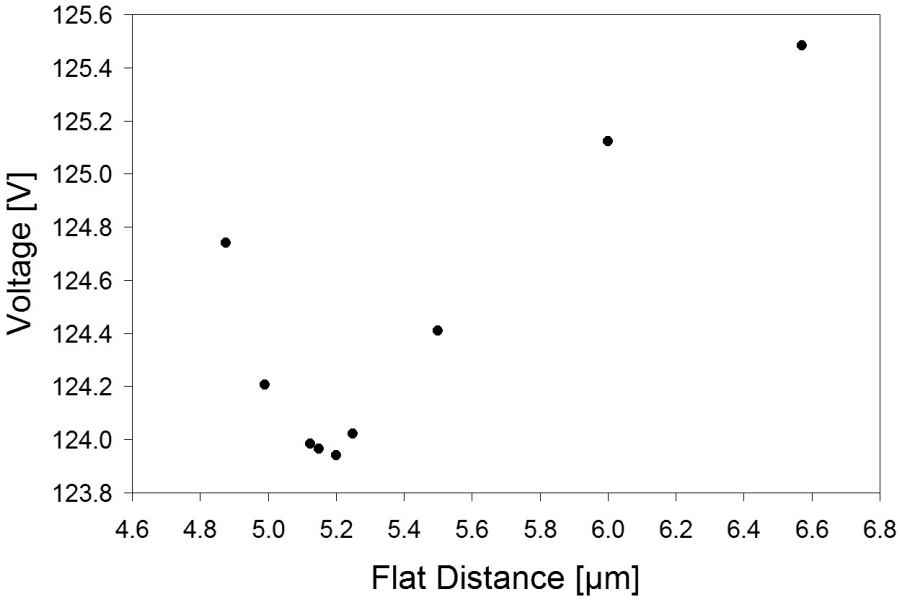

Figure 6.20: Pull-in voltages for fixed-fixed beam linear gap with flattened bottom case.

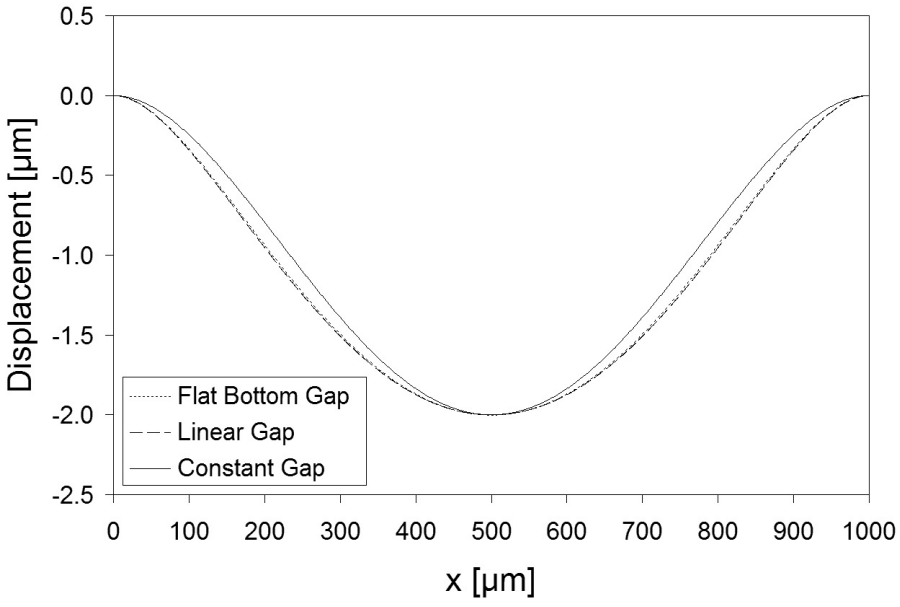

Figure 6.21: Fixed-fixed beam displacement profile.

6.6 Summary

A variable capacitor with a significantly increased tuning ratio over the pull-away variable capacitors has been presented. Using the principle of leveraged bending and placing the capacitance electrode on the same side as the actuator electrode, allows the capacitance gap to be fully tuned before the pull-in voltage occurs. In theory, this type of design is capable of an arbitrarily large tuning range. However, auxiliary structures must be incorporated into the design for successful fabrication, which significantly reduces the achievable tuning ratio. A large nickel variable capacitor with 1.0 μm anti-stiction bumps was tested. The device was found to have a 1.9:1 tuning ratio (0.27 to 0.50 pF) at 6 GHz and a tuning voltage of 0 to 63.1 V. The maximum achieved tuning ratio for the pull-away style variable capacitors was 1.36:1 at the same frequency. The Q-factor with no applied actuation voltage at 6 GHz is approximately 90. A significant increase in the tuning ratio would be possible by simply changing the angle of the capacitance electrode in the layout. Also, gold structures are expected to have significantly increased Q-factors, similar to the increase obtained in the pull-away style variable capacitors.

Significant reductions in the actuation voltage of both cantilever beam structures and fixed-fixed beam structures are possible by varying the geometry of the air gap while still achieving a required actuator displacement. The finite element simulator ANSYS Multiphysics has been used to determine both the pull-in voltage and the displacement of the beams before pull-in occurs. Significant reductions in actuation voltage can be made while still maintaining the required displacement by simply varying the gap profile in a linear fashion. In the case of the cantilever beam, this results in the pull-in voltage being reduced by 37.2% and for the fixed-fixed beam case the reduction is 29.6%. Slightly more complicated shapes can provide a further reduction in pull-in voltage. For the cantilever beam, a polynomial ($n = 4/3$) shape provides a reduction in actuation voltage of 40.2% and by flattening the bottom of the linearly varying gap in the fixed-fixed beam case, a reduction in the actuation voltage of 30.5% can be obtained. These simple electrode shapes, while not necessarily optimal, provide significantly large reductions in pull-in voltage, while still maintaining the same maximum beam displacement. In addition, the average beam displacement

has increased, which can be important in applications such as RF MEMS variable capacitors. Further reductions obtained from optimal electrode shapes are believed to be minimal.

7. VM-TEST: Mechanical Property Measurement

7.1 Introduction

In this chapter VM-TEST is presented [109], which is a set of test structures and a corresponding method that allows for the determination of important mechanical parameters, namely Young's modulus [E] and the residual stress [σ_0]. The extraction of mechanical parameters from fabricated structures is important as it strengthens the connection between simulation and fabrication when developing dynamic MEMS devices. VM-TEST is an extension of the M-TEST system [53, 54], which was developed for thin planar layers, into the vertical dimension for thicker layers as often seen in high aspect ratio processing techniques.

The method uses electrostatically actuated cantilever and fixed-fixed beams and the pull-in phenomena associated with this actuation type. At a certain sharp voltage called the pull-in voltage the electrostatic force overcomes the mechanical restoring force and the beam collapses spontaneously closing the remaining gap distance. This voltage can be determined solely from the geometry of the structure and the structure's material properties. If the geometry can be accurately determined, then the material properties can be accurately extracted from pull-in voltage measurements. The following sections outline the development and testing of this system using both nickel and gold test structures.

7.2 Background

Typical planar MEMS cantilever and fixed-fixed beams are shown in Figure 2.1 on page 28. The thin beam structures are suspended over a larger ground plane and are separated by a thin dielectric spacer that also defines the air gap dimension. A DC bias voltage is applied between the beam and the ground plane, which causes a separation of charge between the two. This charge separation creates an electrostatic force that deflects the thin movable beam towards the fixed ground plane. The beam deflects stably until the pull-in voltage is reached, at which, the beam spontaneously deflects the remaining distance and collapses onto the ground plane. This pull-in voltage is defined entirely by the geometry and material

properties of the beam and by the air gap distance.

M-TEST is a test chip for MEMS material property measurement using elecrostatically actuated test structures for planar, silicon based MEMS fabrication. These structures were designed to meet the emerging need for MEMS process monitoring and material property measurement at the wafer level during both process development and manufacturing [54]. This test is analogous to the electrical MOSFET test structures that are often called E-TEST and are used to extract MOSFET device parameters. The principle behind M-TEST is the electrostatic pull-in phenomena of certain test structures, namely cantilever beams, fixed-fixed beams, and diaphragms. Beams of different lengths and diaphragms with different radius are fabricated to improve accuracy. Accurate measurements of the pull-in voltage for the devices are combined along with accurate geometry measurements and, based on these findings, the mechanical properties can be extracted. In this fashion, precise sets of material properties have been produced for planar silicon test structures with ±4% accuracy [54].

These planar structures can be oriented in the vertical direction as shown in Figure 2.2 on page 29 to determine the material properties of high aspect ratio structures fabricated in thick materials. Vertical structures such as these can be fabricated using various micromachining technologies, but are particularly well suited for realization using the LIGA process [10, 85], due to the high aspect ratio requirements of the beams and gaps. These vertical beam structures operate under similar principles as the planar structures. One significant difference is that the ground (fixed) electrode is normally the same size (height) as the beam, but in the planar case the ground plane is modeled as extending out from the beam and can be considered to be infinite. For beams and gaps with high aspect ratios the practical difference between the two is minimal since the fringing field contribution is generally small. The magnitude of the difference is investigated in Section 7.4.

M-TEST is based on a set of closed-form equations that were fitted to a database of pull-in voltages created using a 2-D distributed model. These equations predict the pull-in voltage of cantilever beams, fixed-fixed beams and diaphragms with arbitrary geometry and material properties. The equations for cantilever and fixed-fixed beams are given in Equations 2.9 and 2.10 respectively on page 34, and are slightly modified from [53, 54] to represent the vertical rather than planar orientation of the beams.

Equations 2.9 and 2.10 correspond to the variables shown in Figure 2.2 on page 29, where h is the beam height, l is the beam length, w is the beam width and d is the air gap distance. The equations are simplifications of the general case given in [53,54] and assume there is no residual stress present in the beams. In addition, the equations are only valid in the small deflection regime (linear elastic mechanics) which is valid for $d/w \leq 1$ ([58]).

In [59, 60] the authors have developed pull-in voltage equations for both cantilever and fixed-fixed beams using a VLSI on-chip interconnect capacitance model. The author claims the accuracy of these equations is better when compared to other published models including the equations developed in M-TEST. The pull-in voltage equations adapted from [59, 60] are given in Equations 2.11 and 2.12 for cantilever and fixed-fixed beams respectively and are found on page 34. Here residual stress is included and there is no limitation to small deflections. The equations apply to all structures encountered in this work. For cases with extreme fringing fields or gaps much larger than beam width, the general equations are given in [59, 60].

From [56], for short beams ($h < 5w$), the effective modulus, $\tilde{E}$, is equal to Young's modulus, E, and the effective residual stress, $\tilde{\sigma}$, is equal to the residual stress, σ_0. For tall beams, ($h \geq 5w$), the effective modulus becomes the plate modulus, $E/(1-\nu^2)$, where ν is Poisson's ratio and the effective residual stress becomes $\sigma_0(1-\nu)$ [54]. All beams featured here are considered tall.

7.3 Test Structures and Fabrication

Test structures for material property determination in thick metal MEMS processes have been developed and fabricated using the LIGA process. The challenge in adapting these structures to high aspect ratio devices lies in the fact that long beams and adjacent electrodes usually suffer severe deformations during the development and/or electroplating process, as discussed in Chapter 3, and shown in Figure 7.1.

This figure is a top view depicting the deformation of the narrow and tall (150 μm) PMMA beams intended to define the air gaps during the subsequent electroplating step in the fabrication of device f4 from the pull-away style variable capacitor mask. To overcome this, these beams require additional support structures, as discussed in Chapter 3, that help to

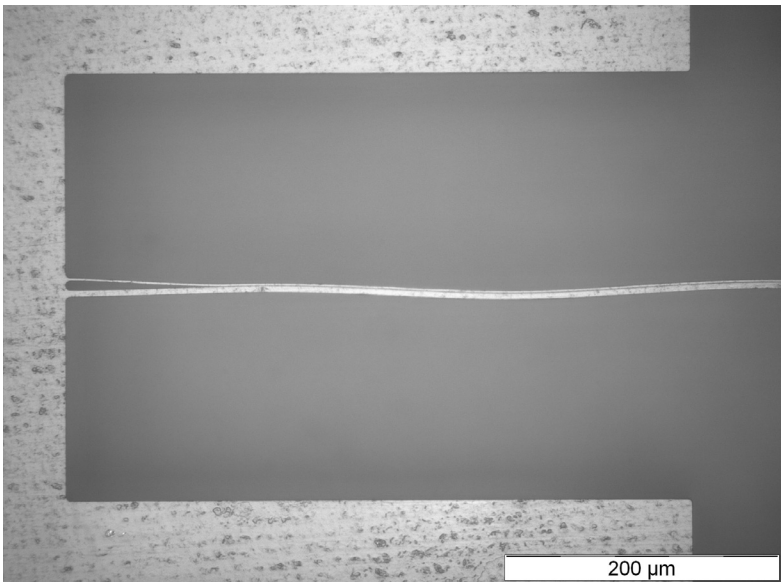

Figure 7.1: Deformation of thin PMMA walls during the development process. Top view of pull-away variable capacitor f4 in 150 µm of PMMA, with PMMA being the light coloured material.

increase the rigidity of the narrow PMMA walls, minimizing deformations during processing. These non-ideal structures still allow the pull-in phenomena, but since the geometry has been modified by including additional features, the pull-in voltage equations, as presented, are not accurate and corrections are necessary.

An overview of the test structure layout is shown in Figure 7.2. Included are 16 fixed-fixed beam structures found in the left two columns and 16 cantilever beam structures found in the right two columns. The 16 structures of each beam type have different beam lengths, which increases accuracy. In [53] it is recommended that at least 10 different lengths of each beam type should be included to ensure enough pull-in data points for a robust curve-fitting scheme.

Figures 7.3 and 7.4 are SEM overview images of fabricated cantilever beam and fixed-fixed beam structures. Each test structure is composed of two metal pieces, an actuator electrode and a ground electrode. In this case, the narrow vertical beam is connected to the ground electrode. The devices are designed to be tested using standard 150 µm pitch ground-

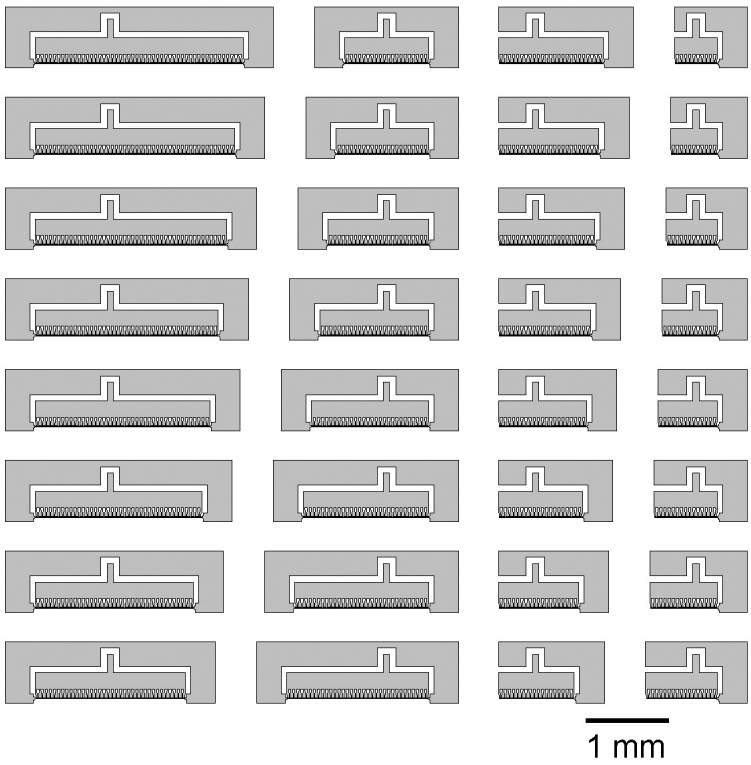

Figure 7.2: Test structure layout. Left two columns are 16 fixed-fixed test structures with varying lengths and right two columns are 16 cantilever test structures with varying lengths.

signal-ground (G-S-G) wafer probes and the probe ports are indicated in Figures 7.3 and 7.4. During actuation, a variable DC voltage is applied to the actuator electrode and the beam is grounded. The polarity of the DC voltage is reversed from that shown in Figure 2.1 (page 28) and Figure 2.2 (page 29), but device operation is unaffected.

The nominal length of the beams is 500 μm to 1250 μm in 50 μm steps for the cantilevers and 1000 μm to 2500 μm in 100 μm steps for fixed-fixed beams. The nominal beam width is 8 μm and the nominal air gap distance is 7 μm. These values were chosen with the understanding that the beam width of fabricated structures would be slightly larger and the air gap distance of fabricated structures would be slightly smaller than the nominal dimensions due to inaccuracies in the fabrication process. Provided the residual stress is low, this set of dimensions restricts pull-in voltages to less than 200 V for the set of metals of interest (gold, copper, and nickel).

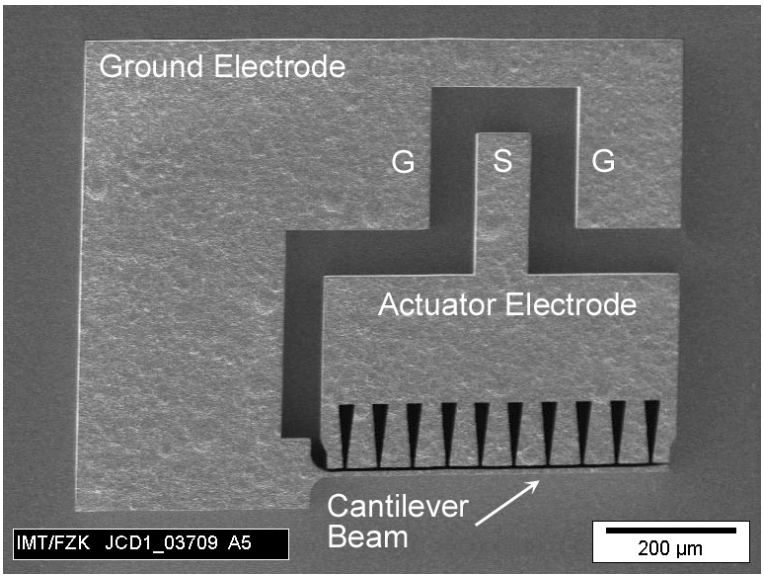

Figure 7.3: Top view of cantilever beam test structure. 100 µm tall nickel device with 500 µm beam length.

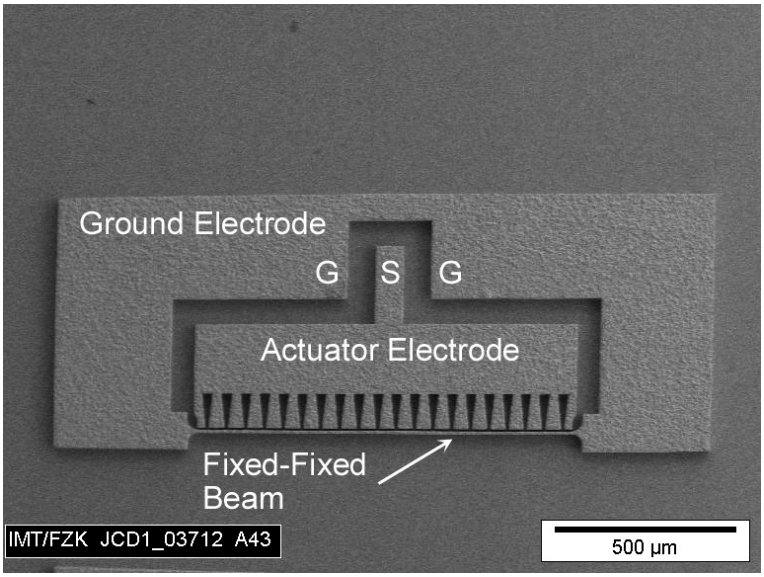

Figure 7.4: Top view of fixed-fixed beam test structure. 100 µm tall nickel device with 1000 µm beam length.

Figures 7.5 and 7.6 are detailed views of the beam attachment point where the thin beam connects to the larger ground structure. This connection has been rounded with a radius of 30 μm as shown in Figure 7.5, in order to reduce the stress at the attachment point during actuation. Also visible in Figures 7.5 and 7.6 are the triangular voids which add structural support for the thin PMMA wall and reduce deformations during development and electroplating processes [50]. These triangular voids also assist in the etching process by allowing the etchant to more freely move into the narrow gaps. The spacing between voids is 50 μm and the first void is placed 25 μm from the edge. The triangles are 10 μm wide closest to the gap and expand to 30 μm wide over a distance of 75 μm. Also shown are anti-stiction bumps which project out from the surface a distance of 1 μm. These bumps are included to prevent the thin beams from sticking after they collapse onto the actuator electrode. This collapse can occur while drying after the etch process, or when the pull-in voltage is exceeded during testing.

Fabrication of these structures was performed using the LIGA process at the Institute for Microstructure Technology (IMT) at the Karlsruhe Institute for Technology (KIT). A sample is prepared by first sputtering a 1 mm thick alumina wafer with 3 μm of titanium

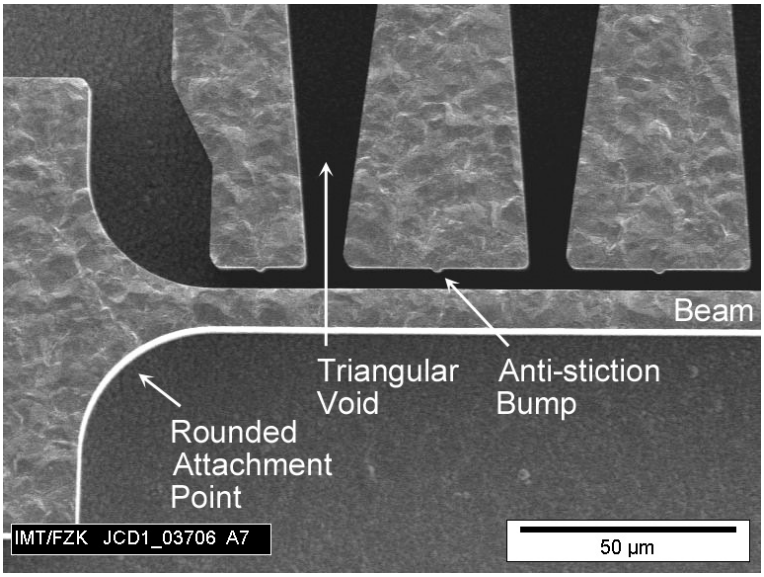

Figure 7.5: Detailed top view of attachment point of 100 μm tall nickel test structure.

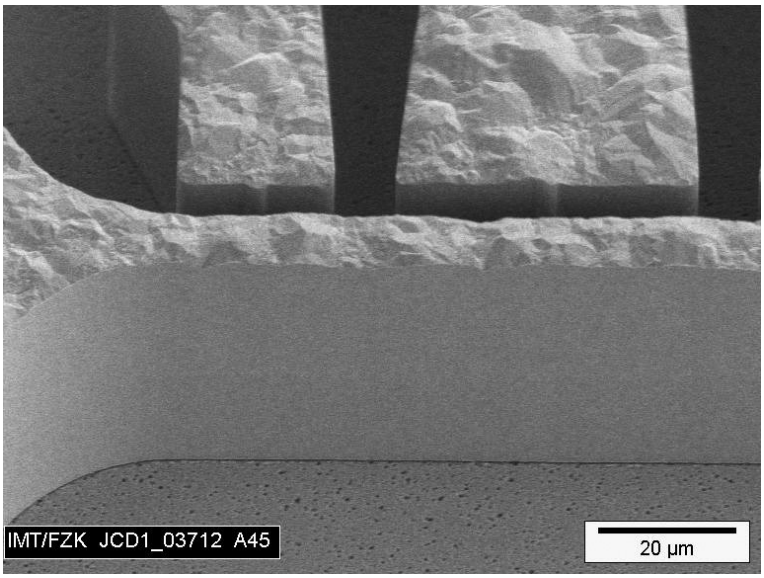

Figure 7.6: Inclined view of attachment point of 100 µm tall nickel test structure.

that initially acts as an electroplating seed layer. This titanium seed layer is oxidized to increase the adhesion of the 150 µm thick PMMA (GS 233) photoresist foil that is glued on top of it. These samples were exposed to X-rays using the 2.5 GeV electron storage ring ANKA and the bending magnet beamline Litho-2. The X-rays pass through an X-ray mask featuring 20 µm thick gold absorbers on a 2.7 µm thick titanium membrane. The bottom dose deposition was set at 3.5 kJ/cm^3. Following exposure, the exposed areas are developed using megasonic-supported GG developer at room temperature for 2.5 hours. The titanium coating on the wafer is then used as a plating base and the voids are filled to a height of 100 µm with electroplated nickel or gold. To remove the remaining PMMA resist, the sample is flood exposed, then given another step of development. Finally, the titanium coating is etched for approximately 6 minutes in 1% HF acid. This etch step acts as a time-controlled sacrificial layer that releases the thin beams from the substrate and electrically isolates the metal structures, but still maintains good adhesion of the larger metal parts.

7.4 Analysis of Difference in Pull-in Voltage between Ideal Beams and Fabricated Beams

As mentioned in the previous section, Equations 2.11 and 2.12 (page 34) are not sufficient to describe the pull-in voltage for the fabricated structures with the additional features highlighted in Figure 7.5. What is required is a method to determine the difference in pull-in voltage between the ideal case (for which the equations hold) and the fabricated structures. The values measured using the fabricated structures can then be scaled to ideal case values where the given equations can be used.

The analysis was performed using both 2-D and 3-D FEM simulations using ANSYS Multiphysics. A representative set of fabricated structures, as well as the ideal counterpart structures, were independently analyzed using ANSYS for each type of feature deviation from the ideal case. The parameters of the test set are listed as follows: beam types (cantilever, fixed-fixed); beam lengths (longest, shortest); beam widths (9 μm, 10 μm); gap widths (5 μm, 6 μm); material properties ($\{E = 75$ GPa, $\nu = 0.45\}$, $\{E = 200$ GPa, $\nu = 0.30\}$). This results in a test set composed of 16 cantilever beam structures and 16 fixed-fixed beam structures, which is meant to encompass the range of dimensions observed in fabricated structures.

The results from these simulations form a database and given the measured dimensions of a particular structure, the change in pull-in voltage from the ideal case can be interpolated. It should be noted that none of the changes were found to be dependent on material properties, which is important since these are the parameters we are trying to identify. Also the pull-in voltage of a fabricated structure can be smaller or larger than the ideal structure depending on structure type and dimensions.

To implement this in ANSYS, the beam is created and meshed with rectangular structural elements of type 82 (95 for 3-D) with the plane strain option turned on since the beam is tall and the plate modulus should be used. The beam and stationary electrode are surrounded by an air box which is meshed with rectangular electrostatic elements of type 121 (123 for 3-D). The stationary electrode does not receive mesh since the interior of it is neither a structural element nor an electrostatic element. The material properties are defined and

structural constraints are placed on the beam. Nonlinear geometry effects are turned on using the NLGEOM command. The beam has 0 V applied to it and the stationary electrode has the input voltage applied to it. Structural and electrostatic physics files are written and a coupled analysis is performed using the ESSOLV macro.

To verify the performance of the ANSYS simulator in obtaining accurate pull-in voltages, the results obtained from ANSYS for the ideal cases were compared to the results from the pull-in voltage equations given is Chapter 2. On average, for the complete test set, the ANSYS results agree with the pull-in voltage equations to a percentage difference of less than 2%. In the following sections, each type of feature deviation from the ideal case will be discussed and the magnitude of the effect on the pull-in voltage will be given.

7.4.1 Rounded Attachment Points (2-D Analysis)

The first difference investigated is the rounded attachment point included on the fabricated structures shown in Figure 7.5. This 30 μm rounding has the effect of making the beam less rigid and decreasing the pull-in voltage. Two-dimensional analysis was chosen since the rounding is consistent throughout the height of the structure. In all test set geometries, the rounded structures showed a reduction in pull-in voltage. The pull-in voltage change was weakly dependent on gap width and strongly dependent on beam length. For short cantilevers the reduction varied from 4.24 to 4.35% and for long cantilevers the reduction varied from 1.66 to 1.74%. For short fixed-fixed beams the reduction varied from 4.21 to 4.52% and for long fixed-fixed beams the reduction varied from 1.71 to 1.83%.

7.4.2 Anti-stiction Bumps (2-D Analysis)

Small anti-stiction bumps (in this case approximately 2 μm wide and 1 μm long) were included to reduce the surface area during contact, which also effectively reduces the gap width and decreases the pull-in voltage. The reduction in pull-in voltage was weakly dependent on both the gap width and beam length. For cantilevers, the pull-in voltage was reduced between 1.85 and 2.57% and for fixed-fixed beams the reduction was between 1.87 and 2.24%.

7.4.3 Triangular Electrode Voids (2-D Analysis)

The triangular voids added into the actuator electrode reduce the surface area, which increases the pull-in voltage. Electrode void widths of both 8 μm and 10 μm were simulated to determine the increase in pull-in voltage. It was found that the increase in voltage is weakly dependent on both gap width and beam length. For 8 μm voids, the cantilever beam pull-in voltage was increased between 3.50 and 4.73% and the fixed-fixed beam pull-in voltage was increased between 4.30 and 4.79%. The larger void width led to larger pull-in voltages as expected. For 10 μm voids, the cantilever beam pull-in voltage increased between 6.09 and 6.86% and the fixed-fixed beam pull-in voltage was increased between 6.29 and 7.12%.

7.4.4 Non-infinite Ground Plane (3-D Analysis)

As mentioned in Section 7.2, the theoretical equations given for the pull-in voltage are appropriate for planar structures situated over an infinite ground plane. For the high aspect ratio structures presented here, the electrode and the beams have approximately the same size. This will cause a slight increase in the pull-in voltage as the fringing fields will be weaker than in the infinite ground plane case. Using full 3-D analysis, the magnitude of the difference was investigated on 100 μm tall structures. The change in pull-in voltage varies with structure height since the fringing contribution decreases with an increase in structure height. In this case, 2-D analysis is not adequate since it neglects the fringing effects along the top and bottom of the beam. The increase in pull-in voltage was found to be weakly dependent on gap width and beam length. For cantilever beams, the pull-in voltage increased between 0.52 and 0.88% and for fixed-fixed beams the pull-in voltage increased between 0.29 and 0.87%.

7.4.5 Sidewall Verticality

In practice, the sidewalls of a structure cannot be made perfectly vertical and will have some slope. If this slope is significantly large then the beams and gaps will not have a uniform width and the above equation based on ideal structures will not be valid. However, one of the advantages of the LIGA process is the abilty to produce tall, vertical structures. In [11],

it is shown that structures with a variation in width of only 0.04 μm per 100 μm of height can be fabricated. For the beam and gap widths discussed here, this amounts to less than 1% change in width from the top of the structure to the bottom of the structure and will therefore be neglected.

7.5 Test Results

To determine the material properties of a set of electroplated structures, the following steps need to be performed on a group of cantilevers or fixed-fixed beams:

1. Measure the dimensions of all structures in the test set. The dimensions include the beam width, gap width, and possibly beam length. Also, the average void width for each structure has to be determined.

2. Measure the pull-in voltage for each structure.

3. Convert the measured pull-in voltage values to ideal pull-in voltage values using the database of simulation data.

4. Fit the ideal pull-in voltage values to Equation 2.11 or Equation 2.12 (page 34), for cantilever beams or fixed-fixed beams respectively, and determine the material properties.

The beam length of each individual structure could be measured to improve the accuracy of the material property extraction. Since the beams are quite long, the difference from the layout is expected to be small and therefore the associated error will be small. Each test set contains 10 beams per structure type as recommended in [53]. Fewer structures could be used with a decrease in accuracy. Cantilever beams should only be used in the case of low residual stress. For the structures presented here, known low stress electroplating processes were used. In addition, the released beams showed no signs of warping and were nicely centered. The results for both nickel and gold cantilever structures are shown in Tables 7.1 and 7.2 respectively.

The average beam width, gap width and void width were measured for both nickel and gold cantilever beams ranging in length from 650 μm to 1100 μm using an optical microscope

Table 7.1: Nickel cantilever values.

Beam length (μm)	650	700	750	800	850	900	950	1000	1050	1100	Ave.
Beam width (μm)	9.29	9.53	9.47	9.27	9.33	9.30	9.43	9.37	9.44	9.32	9.38
Gap width (μm)	5.40	5.52	5.62	5.34	5.59	5.47	5.55	5.58	5.49	5.65	5.52
Void width (μm)	9.52	9.60	9.47	9.42	9.53	9.58	9.57	9.63	9.47	9.53	
Measured pull-in (V)	71.1	60.3	55.2	45.9	43.3	32.3	30.2	30.3	24.9	24.0	
Ideal pull-in (V)	70.78	59.84	54.75	45.46	42.76	31.83	29.73	29.71	24.38	23.50	

Table 7.2: Gold cantilever values.

Beam length (μm)	650	700	750	800	850	900	950	1000	1050	1100	Ave.
Beam width (μm)	10.25	10.42	10.55	10.65	10.73	10.28	10.51	10.63	10.69	10.45	10.52
Gap width (μm)	4.68	4.61	4.44	4.37	4.57	4.43	4.47	4.42	4.35	4.58	4.49
Void width (μm)	9.50	9.58	9.46	9.56	9.63	9.66	9.52	9.59	9.49	9.53	
Measured pull-in (V)	42.5	32.5	25.2	22.5	21.6	19.2	16.8	16.0	13.6	15.0	
Ideal pull-in (V)	42.22	32.23	24.93	22.17	21.23	18.86	16.43	15.60	13.29	14.56	

and imaging software. For beam width and gap width, 5 points along the length were measured and the average was taken. For the void width, each void was measured and the average was taken.

The pull-in voltage was measured by probing the structures with tungsten G-S-G wafer probes (Cascade Microtech ACP40-W-GSG-150) connected to a DC power supply through a series resistor (100 kΩ). The series resistor was included to limit the current produced when the beam collapses after pull-in. The voltage was slowly increased by manually adjusting the supply until current was detected in the circuit which signifies pull-in has occurred. It is believed that the error associated with this technique is approximately ±0.1 V. More accurate automated methods could also be employed to further reduce this error.

The measured pull-in voltage values were then converted to ideal pull-in voltage values using the database of simulation results discussed in Section 7.4. This was performed by interpolating the database to the fabricated device dimensions, which results in a percentage change for each type of feature deviation from the ideal case. For all feature deviations, the percentage changes are summed and the total is applied to the measured pull-in voltage value giving the ideal pull-in voltage value. For the gold structures, the gap width and beam width are outside of the database range and therefore the ideal pull-in voltage values had to be extrapolated from the database. Ideal pull-in voltage values, corrected to average beam and gap widths using Equation 2.11, are shown in Figures 7.7 and 7.8 for nickel and gold test structures respectively.

To determine the material properties, a sum of least squares fitting scheme was used with the ideal pull-in voltage values listed in Tables 7.1 and 7.2. The effective modulus $\tilde{E}$ was varied and pull-in voltage values were calculated using Equation 2.11 until a minimum sum of the squares of the errors was achieved. For fixed-fixed beams, both $\tilde{E}$ and $\tilde{\sigma}$ should be varied. The least squares fit is shown in Figures 7.7 and 7.8 for nickel and gold respectively using the average values for beam width and gap width. To extract E from $\tilde{E}$, values for ν of 0.31 for nickel and 0.45 for gold were used [49]. This resulted in a Young's modulus of 186.2 GPa for nickel and 60.8 GPa for gold.

For nickel, this is significantly smaller than the 207 GPa reported for bulk material [49], but is within the range of values present in the literature for thick layers of electroplated

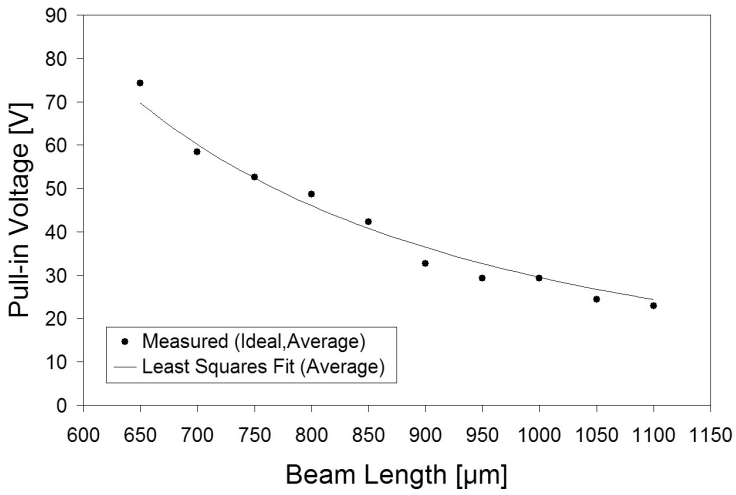

Figure 7.7: Measured and fit data for nickel cantilever beams.

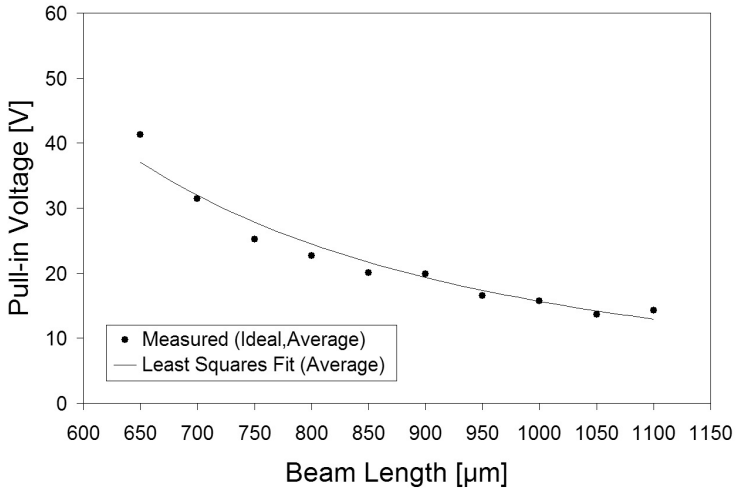

Figure 7.8: Measured and fit data for gold cantilever beams.

nickel from a sulfamate bath, which varies from 125 - 231 GPa, as shown in Chapter 1. The Young's modulus of the electroplated gold sample is also significantly smaller than the 78 GPa reported for bulk gold [49]. A lack of data exists for the mechanical properties of electroplated thick gold layers, but this value is in the range reported for thin gold films 35 - 78 GPa [120], which also has a fairly wide range, but shows a general trend of values

below that of bulk gold.

7.6 Summary

A simple, accurate, and relatively quick method to determine the mechanical properties of thick metal layers using the pull-in voltage of electrostatically actuated test structures has been developed. These structures were fabricated using the LIGA process and contain unique features that minimize the deformation of the high aspect ratio beams during the processing sequence. The inclusion of these features makes existing pull-in voltage equations inaccurate and corrections are necessary. To analyze the differences between ideal beams and these modified fabricated beams, both 2-D and 3-D finite element method simulations were performed using ANSYS Multiphysics. Both nickel and gold devices were fabricated to demonstrate the proposed approach. For each material, the pull-in voltage of 10 cantilever beams was measured, then converted to ideal pull-in voltage values using the results from ANSYS simulations. A sum of least squares fitting scheme was then used to extract the material property values from the ideal pull-in voltage values. For the nickel structures, a Young's modulus of 186.2 GPa was obtained and for gold, the value was 60.8 GPa. Both values are significantly smaller than values reported for bulk material, but fall within the range of values reported in the literature.

8. Conclusion

8.1 Summary and Conclusions

During the course of this work, several high aspect ratio, vertical, cantilever and fixed-fixed beam actuators, fabricated from various metals, were demonstrated in various devices. The potential applications of these actuators are widespread, particularly in the field of RF MEMS. Microstructures fabricated using thick metal layers have potentially significant advantages including increased coupling capacitances from tall sidewalls as well as increased power handling from thicker layers. Lower loss and dispersion are also possible due to the separation of the electromagnetic fields from the substrate. Also, smaller "volume efficient" devices could be achieved by trading lateral dimensions for vertical dimensions. This leads to devices that operate at higher frequencies and appear more lumped at higher frequencies. Smaller structures also lead to better integration from a systems point of view. These characteristics allow them to be combined into lumped-element circuits such as filters and couplers, which replace bulky transmission line versions, and were demonstrated in [5]. Placing actuator structures into these lumped-element versions would make them tunable and could greatly increase their versatility. Also shown in this work was the ability to incorporate anti-stiction measures (bumps) directly onto the mask layout. In planar fabrication processes, this is significantly more complicated and typically requires an additional lithography step. These bumps could also potentially be used as fine resolution contact surfaces in the case of vertically oriented RF MEMS contact switches.

However, the fabrication of these structures is not trivial, as the aspect ratios found in these tall actuators can be greater than 50:1. The thin beams and gaps, which run laterally for hundreds of microns, and are required for electrostatic actuation at appropriate voltage levels, are very difficult to fabricate without the addition of auxiliary supporting structures into the layout and optimized fabrication processes. This work involves improving the processing of these types of high aspect ratio actuators and utilizing them in novel devices, examples of which include, RF MEMS variable capacitors and structures for the

determination of mechanical material properties. The objectives of this research, as stated in Chapter 1, are:

1. Fully realize the LIGA-MEMS pull-away style variable capacitors. This includes the ability to actuate and test the tuning characteristics of the devices, which was not possible in [19]. Investigate areas of the fabrication process that can be optimized to eliminate or minimize the deformations that are present in the structures so that smaller designs can be fabricated and tested. Also, investigate other materials that can be utilized to increase the performance of the capacitors.

2. Investigate and implement a technique that can be used to realize LIGA-MEMS variable capacitor structures with a larger tuning range. This includes the design of the structure as well as the simulation, fabrication and testing of the device. Also investigate a method to reduce the actuation voltage required by these high aspect ratio beam structures.

3. Develop a set of test standards that can accurately determine the important mechanical material properties from an arbitrary electroplating process, which will improve the feedback loop between simulation and fabrication.

Pull-away style, high aspect ratio, high Q-factor, RF MEMS variable capacitors have been realized using deep X-ray lithography and electroplating in both large and small device sizes and in both nickel and gold metal layers. Device operation and RF performance results have been presented in [5,85]. These structures demonstrate, for the first time, that DXRL is suitable for the fabrication of high performance RF MEMS devices with movable parts, due to the ability to fabricate thick metal structures with precise features. The tall vertical structure of these devices results in low loss and high performance, mainly due to the separation of fields from the substrate and the use of thick metal layers. Q-factors as large as 214 at 3.5 GHz, 95 at 5.6 GHz and 39 at 7.4 GHz have been measured for a capacitor with a 0.57 pF nominal capacitance at 5.6 GHz. This same device features a 1.36:1 tuning ratio at 6 GHz and a tuning voltage of 7.8 V.

Fabrication of these devices is challenging as the fabricated capacitors feature very long beams ($>$ 1 mm) and narrow gaps (down to 1.3 μm) which results in high aspect ratios of

approximately 115 in PMMA and 75 in electroplated metal. To successfully fabricate these devices, certain optimizations had to be made to the fabrication process, some of which were presented in [50]. It was found that only the devices with auxiliary supporting structures such as periodic beam widening and triangular voids (resist relief) could be fabricated without severe deformations. The most important optimization to the fabrication process was a modified electroplating step, which allowed for electroplating at ambient temperatures. This significantly reduced swelling effects as well as thermal expansion effects, which resulted in structures with significantly reduced deformation.

In the pull-away style variable capacitors, it was found that the beams were suffering from a phenomena called "stiction" during the etch release step as well as during operation. This causes the beams to adhere to the adjacent electrodes. An analysis of the phenomena and how it relates to this class of structures was presented in [86]. The critical dimensions of structures as well as a critical dimension example was also presented. Based on these critical dimensions, a method to eliminate stiction in this class of structures has been developed based on a contact area reduction technique.

A variable capacitor with a significantly increased tuning ratio over the pull-away style variable capacitors has been presented. These devices use the principle of leveraged bending, which significantly increases the achievable beam displacement at the cost of an increase in tuning voltage. A device with a tuning ratio of 1.9:1 at 6 GHz has been realized with high Q-factors similar to the pull-away style variable capacitors. A significant increase in the tuning ratio to approximately 2.7:1 would be possible by simply changing the angle of the capacitance electrode in the layout.

To significantly reduce the actuation voltage in future designs, a FEM study on the shape of the actuation gap for cantilever and fixed-fixed beams was performed and the results have been presented in [110] and also in Chapter 6. In both beam types, varying the gap profile in a linear fashion provided significant reductions in the required actuation voltage. In the cantilever case, a polynomial ($n = 4/3$) shape provided the greatest voltage reduction (up to 40.2%) and in the fixed-fixed case, a linearly varying gap with a flattened bottom provided the greatest voltage reduction (up to 30.5%). These simple electrode shapes, while not necessarily optimal, provide significantly large reductions in pull-in voltage, while

still maintaining the same maximum beam displacement. Further reductions obtained from optimal electrode shapes are believed to be minimal.

A set of test structures called VM-TEST was developed as an efficient method to determine the mechanical properties of thick metal layers using the pull-in voltage of electrostatically actuated structures [109]. This is important as the accurate experimental determination of material properties strengthens the connection between simulated and fabricated devices. The addition of auxiliary structures made existing pull-in voltage equations inaccurate. Corrections were made by performing finite element simulations on both ideal and fabricated structures. Results from nickel and gold samples give Young's modulus values of 186.2 GPa and 60.8 GPa respectively.

These results were shown to significantly improve the difference between measured and simulated actuation voltage values for the leveraged bending capacitor device. At maximum capacitance, with experimentally determined mechanical properties, the voltage varies by only 3% where as in the case of bulk nickel mechanical properties, the voltage varies by 9%.

These experimentally determined mechanical properties would also improve the difference in measured and simulated pull-in voltages for the pull-away style variable capacitors. Simulated pull-in voltages using bulk values were too large and the experimentally determined Young's modulus values would decrease these values. A comparison is possible, but results drawn from these conclusions are likely inaccurate as these structures were fabricated at different times using different electroplating baths.

The devices in this work feature an approximately 3 μm Ti/TiO_x electroplating seed layer over the entire substrate. To electrically isolate the structures and time-critically release the thin beams this seed layer must be etched. The challenge in this step lies with the narrow and deep air gaps. Uniform penetration of the etchant into these gaps has been found to be difficult with traditional titanium etchants such as 5% HF acid. When the etchant is slow in moving into the gaps, the larger structures become severely underetched before the beams are fully released from the substrate. A solution was found by diluting the concentrated 48% HF to 10% by volume using isopropanol (IPA) instead of DI water. This lowers the surface tension, improving the penetration of the etchant into the gaps, resulting in increased etch uniformity. In addition, a 5 minute pre-soak in pure IPA then a direct transfer into the

etchant was beneficial as this helps to fully wet the gaps and draw the etchant into the gaps during the etch step. This etching technique will allow for the uniform etching of a wide class of high aspect ratio structures.

8.2 Contributions

Specific contributions of this work include:

1. Fully realizing the pull-away style RF MEMS variable capacitors [5, 50, 85].
2. Analysis of the stiction phenomena and how it relates to this class of structures and materials [86].
3. Development of RF MEMS variable capacitors with a significantly increased tuning ratio over the pull-away style variable capacitors, using the principle of leveraged bending.
4. A study on the shape of the actuation gap that allows the actuation voltage to be significantly reduced, while still maintaining a required actuator displacement [110].
5. Development of a set of test structures called VM-TEST to determine the mechanical properties of thick metal layers [109].
6. An improved titanium etchant for uniformly etching high aspect ratio holes and trenches.

8.3 Future Work

The following items should be investigated to continue the current study and to more thoroughly investigate the subject:

1. Further characterize the pull-away and leveraged bending style variable capacitors in terms of reliability, power handling capability and tuning speed.
2. Testing of the leveraged bending style variable capacitors in smaller device sizes and higher conductivity metals should be performed.

3. For the VM-TEST mechanical material property structures, future work will concentrate on investigating fixed-fixed beams with higher stress samples, automation of the conversion process from measured pull-in voltage values to ideal, improving the accuracy of the pull-in voltage measurement, improving the accuracy of beam and gap measurements, and determining the associated error.

4. Both the modified pull-away variable capacitor designs and the switch designs included on the layout should be tested and characterized.

5. Electrical material properties, similar to the mechanical material properties, should be more comprehensively determined as this determines the accuracy of simulations. Of particular interest is the uncertainty in the relative permeability of nickel at high frequencies.

6. Future designs should incorporate the modified gap shapes that were developed to reduce the required actuation voltage.

7. The application of monolayers as an anti-stiction mechanism should be further investigated. In particular, the removal of the native oxide layer from the nickel surface before the application of the monolayer should be attempted.

8. A high aspect ratio to planar transition structure should be designed, fabricated and tested that can efficiently connect tall structures to planar structures and would simplify the interface to planar circuitry.

REFERENCES

[1] Yole Développement, "Status of the MEMS Industry 2011," tech. rep., September 2011.

[2] J.J. Yao, "RF MEMS from a device perspective," *Journal of Micromechanics and Microengineering*, vol. 10, pp. R9–R38, December 2000.

[3] G.H. Stauffer, "Finding the lumped element varactor diode model," *High Frequency Electronics*, pp. 22–28, November 2003.

[4] D. Peroulis, S. Pacheco, K. Sarabandi, and L.P.B. Katehi, "Tunable lumped components with applications to reconfigurable MEMS filters," in *IEEE MTT-S International Microwave Symposium Digest*, vol. 1, (Phoenix, AZ), pp. 341–344, May 2001.

[5] D.M. Klymyshyn, M. Börner, D.T. Haluzan, E. Gono Santosa, M. Schaffer, S. Achenbach, and J. Mohr, "Vertical high-Q RF-MEMS devices for reactive lumped-element circuits," *IEEE Transactions on Microwave Theory and Techniques*, vol. 58, pp. 2976–2986, November 2010.

[6] C. Goldsmith, J. Ehmke, A. Malczewski, B. Pillans, S. Eshelman, Z. Yao, J. Brank, and M. Eberly, "Lifetime characterization of capacitive RF MEMS switches," in *IEEE MTT-S International Microwave Symposium Digest*, vol. 1, (Phoenix, AZ), pp. 227–230, May 2001.

[7] Hector J. De Los Santos, *Introduction to Microelectromechanical (MEM) Microwave Systems*. Boston, MA: Artech House, 1999.

[8] J.H. Comtois, V.M. Bright, and M.W. Phipps, "Thermal microactuators for surface-micromachining processes," *Proceedings of SPIE - The International Society for Optical Engineering*, vol. 2642, pp. 10–21, 1995.

[9] E.W. Becker, W. Ehrfeld, D. Münchmeyer, H. Betz, A. Heuberger, S. Pongratz, W. Glashauser, H.J. Michel, and R.v. Siemens, "Production of separation nozzle system

for uranium enrichment by a combination of X-ray lithography and galvanoplastics," *Naturwissenschaften*, vol. 69, pp. 520–523, November 1982.

[10] E.W. Becker, W. Ehrfeld, P. Hagmann, A. Maner, and D. Münchmeyer, "Fabrication of microstructures with high aspect ratios and great structural heights by synchrotron radiation lithography, galvanoforming, and plastic moulding (LIGA process)," *Microelectronic Engineering*, vol. 4, pp. 35–36, May 1986.

[11] J. Mohr, W. Ehrfeld, and D. Münchmeyer, "Requirements on resist layers in deep-etch synchrotron radiation lithography," *Journal of Vacuum Science and Technology B*, vol. 6, pp. 2264–2267, November 1988.

[12] W. Menz, J. Mohr, and O. Paul, *Microsystem Technology*. Weinheim, Germany: Wiley-VCH, 2001.

[13] T.L. Willke and S.S. Gearhart, "LIGA micromachined planar transmission lines and filters," *IEEE Transactions on Microwave Theory and Techniques*, vol. 45, pp. 1681–1688, 1997.

[14] K.Y. Park, J.C. Lee, J.H. Kim, B. Lee, N.Y. Kim, J.Y. Park, G.H. Kim, J.U. Bu, and K.W. Chung, "A new three-dimensional 30 GHz bandpass filter using the LIGA micromachined process," *Microwave and Optical Technology Letters*, vol. 30, pp. 199–201, 2001.

[15] A.A. Kachayev, D.M. Klymyshyn, S. Achenbach, and V. Saile, "High vertical aspect ratio LIGA microwave 3-dB coupler," in *International Conference on MEMS, NANO and Smart Systems*, pp. 38–43, 2003.

[16] Z. Ma, D.M. Klymyshyn, S. Achenbach, M. Börner, N. Dambrowsky, and J. Mohr, "An ultra-deep high-Q microwave cavity resonator fabricated using deep X-ray lithography," *IEICE Transactions on Electronics*, vol. E90-C, pp. 2192–2197, 2007.

[17] D.M. Klymyshyn, H.C. Jayatilaka, M. Börner, and J. Mohr, "High aspect-ratio coplanar waveguide wideband bandpass filter with compact unit cells," *IEEE Transactions on Microwave Theory and Techniques*, vol. 57, no. 11, pp. 2753–2760, 2009.

[18] A. Rashidian, D.M. Klymyshyn, M. Börner, and J. Mohr, "Deep X-ray lithography processing for batch fabrication of thick polymer-based antenna structures," *Journal of Micromechanics and Microengineering*, vol. 20, p. 025026, 2010.

[19] D.T. Haluzan, "Microwave LIGA-MEMS Variable Capacitors," M.Sc., University of Saskatchewan, Saskatoon, Saskatchewan, December 2004.

[20] K.R. Williams, K. Gupta, and M. Wasilik, "Etch rates for micromachining processing - part II," *Journal of Microelectromechanical Systems*, vol. 12, pp. 761–778, December 2003.

[21] D.J. Young and B.E. Boser, "A micromachined variable capacitor for monolithic low-noise VCOs," in *Solid-State Sensor and Actuator Workshop*, (Hilton Head, SC), pp. 86–89, 1996.

[22] A. Dec and K. Suyama, "Micromachined electro-mechanically tunable capacitors and their applications to RF IC's," *IEEE Transactions on Microwave Theory and Techniques*, vol. 46, pp. 2587–2596, December 1998.

[23] J. Jou, C. Liu, and J. Schutt-Aine, "Development of a wide tuning range two-parallel-plate tunable capacitor for integrated wireless communication systems," *International Journal of RF and Microwave Computer Aided Design*, vol. 11, pp. 322–329, September 2001.

[24] H.S. Lee, Y.J. Yoon, D.H. Choi, and J.B. Yoon, "High-Q, tunable-gap MEMS variable capacitor actuated with an electrically floating plate," in *International Conference on Micro Electro Mechanical Systems*, pp. 180–183, IEEE, January 2008.

[25] M. Bakri-Kassem and R.R. Mansour, "Linear bilayer ALD coated MEMS varactor with high tuning capacitance ratio," *Journal of Microelectromechanical Systems*, vol. 18, pp. 147–153, February 2009.

[26] J.J. Yao, S. Park, and J. DeNatale, "High tuning ratio MEMS based tunable capacitors for RF communications applications," in *Solid-State Sensor and Actuator Workshop*, (Hilton Head, SC), pp. 124–127, 1998.

[27] R.L. Borwick III, P.A. Stupar, J. DeNatale, R. Anderson, C. Tsai, K. Garrett, and R. Erlandson, "A high Q, large tuning range MEMS capacitor for RF filter systems," *Sensors and Actuators, A: Physical*, vol. 103, pp. 33–41, January 2003.

[28] L. Gu and X. Li, "Variable capacitors and tunable LC-tanks formed by CMOS-compatible metal MEMS for RF ICs," in *IEEE International Electron Devices Meeting*, pp. 427–430, December 2007.

[29] Z. Feng, H. Zhang, K.C. Gupta, W. Zhang, V.M. Bright, and Y.C. Lee, "MEMS-based series and shunt variable capacitors for microwave and millimeter-wave frequencies," *Sensors and Actuators, A: Physical*, vol. 91, pp. 256–265, July 2001.

[30] L. Dussopt and G.M. Rebeiz, "High-Q millimeter-wave MEMS varactors: Extended tuning range and discrete-position designs," in *IEEE MTT-S International Microwave Symposium Digest*, vol. 2, pp. 1205–1208, June 2002.

[31] T.G.S.M. Rijks, J.T.M. van Beek, P.G. Steeneken, M.J.E. Ulenaers, J. De Coster, and R. Puers, "RF MEMS tunable capacitors with large tuning ratio," in *17th IEEE International Conference on Micro Electro Mechanical Systems*, pp. 777–780, September 2004.

[32] Q. Shen and N.S. Barker, "Distributed MEMS tunable matching network using minimal-contact RF-MEMS varactors," *IEEE Transactions on Microwave Theory and Techniques*, vol. 54, pp. 2646–2658, June 2006.

[33] G. McFeetors and M. Okoniewski, "Performance and operation of stressed dual-gap RF MEMS varactors," in *36th European Microwave Conference* (IEEE, ed.), pp. 1064–1067, September 2006.

[34] P. Ruther, W. Bacher, K. Feit, D. Maas, and W. Menz, "Prototype of a microtesting system made by the LIGA process to measure the Young's modulus in cantilever microbeams," *ASME Journal of Dynamic Systems, Measurement and Control*, vol. 119, pp. 57–60, March 1997.

[35] E. Mazza, S. Abel, and J. Dual, "Experimental determination of mechanical properties of Ni and Ni-Fe microbars," *Microsystem Technologies*, vol. 2, no. 4, pp. 197–202, 1996.

[36] W.N. Sharpe, Jr,, D.A. LaVan, and R.L. Edwards, "Mechanical Properties of LIGA-deposited nickel for MEMS Transducers," in *International Conference on Solid-State Sensors and Actuators*, (Chicago), pp. 607–610, June 1997.

[37] T.R. Christenson, T.E. Buchheit, D.T. Schmale, and R.J. Boucier, "Mechanical and metallographic characterization of LIGA fabricated nickel and 80%Ni-20%Fe permalloy," in *MRS Symposium Proceedings*, vol. 518, pp. 185–190, 1998.

[38] S. Greek and F. Ericson, "Youngs modulus, yield strength and fracture strength of microelements determined by tensile testing," in *MRS Symposium Proceedings*, vol. 518, pp. 51–56, 1998.

[39] Z.L. Xie, D. Pan, H. Last, and K.J. Hemker, "Effect of as-processed and annealed microstructures on the mechanical properties of LIGA Ni MEMS," in *MRS Symposium Proceedings*, vol. 605, pp. 197–202, 2000.

[40] K.J. Hemker and H. Last, "Microsample tensile testing of LIGA nickel for MEMS applications," *Materials Science and Engineering: A*, vol. 319-321, pp. 882–886, December 2001.

[41] H.S. Cho, K.J. Hemker, K. Lian, J. Goettert, and G. Dirras, "Measured mechanical properties of LIGA Ni structures," *Sensors and Actuators, A: Physical*, vol. 103, pp. 59–63, January 2003.

[42] J. Lou, S. Allameh, T. Buccheit, and W.O. Soboyejo, "An investigation of the effects of thickness on mechanical properties of LIGA nickel MEMS structures," *Journal of Materials Science*, vol. 38, no. 20, pp. 4129–4135, 2003.

[43] Y. Yang, S. Allameh, J. Lou, B. Imasogie, B.L. Boyce, and W.O. Soboyejo, "Fatigue of LIGA Ni micro-electro-mechanical system thin films," *Metallurgical and Materials Transactions A*, vol. 38, pp. 2340–2348, September 2007.

[44] T.E. Buchheit, T.R. Christenson, D.T. Schmale, and D.A. Lavan, "Understanding and tailoring the mechanical properties of LIGA fabricated materials," in *MRS Symposium Proceedings*, vol. 546, pp. 121–126, 1998.

[45] L. Robert, *Etude des propriétés mécaniques du Nickel utilisé dans la technique LIGA*. Ph.D., Université de Franche-Comté, Besançon, France, 1997.

[46] L.S. Stephens, K.W. Kelly, S. Simhadri, A.B. McCandless, and E.I. Meletis, "Mechanical property evaluation and failure analysis of cantilevered LIGA nickel microposts," *Journal of Microelectromechanical Systems*, vol. 10, pp. 347–359, September 2001.

[47] H. Majjad, S. Basrour, P. Delobelle, and M. Schmidt, "Dynamic determination of Young's modulus of electroplated nickel used in LIGA technique," *Sensors and Actuators, A: Physical*, vol. 74, pp. 148–151, April 1999.

[48] W.N. Sharpe, Jr,, "Murray lecture tensile testing at the micrometer scale: Opportunities in experimental mechanics," *Experimental Mechanics*, vol. 43, no. 3, pp. 228–237, 2003.

[49] J.R. Davis, *Metals Handbook: Desk Edition*. Materials Park, OH: ASM International, second ed., 1998.

[50] S. Achenbach, D. Klymyshyn, D. Haluzan, T. Mappes, G. Wells, and J. Mohr, "Fabrication of RF MEMS variable capacitors by deep X-ray lithography and electroplating," *Microsystem Technologies*, vol. 13, pp. 343–347, 2006.

[51] D.J. Bell, T.J. Lu, N.A. Fleck, and S.M.Spearing, "MEMS actuators and sensors: observations on their performance and selection for purpose," *Journal of Micromechanics and Microengineering*, vol. 15, pp. S153–S164, June 2005.

[52] N. Paryab, H. Jahed, and A. Khajepour, "Creep and fatigue failure in single- and double hot arm MEMS thermal actuators," *Journal of Failure Analysis and Prevention*, vol. 9, no. 2, pp. 159–170, 2009.

[53] P.M. Osterberg, *Electrostatically actuated microelectromechanical test structures for material property measurements*. Ph.D., Massachusetts Institute of Technology, Cambridge, Massachusetts, September 1995.

[54] P.M. Osterberg and S.D. Senturia, "M-TEST: a test chip for MEMS material property measurement using electrostatically actuated test structures," *Journal of Microelectromechanical Systems*, vol. 6, pp. 107–118, June 1997.

[55] W.C. Young, *Roark's Formulas for Stress and Strain*. New York, NY: McGraw-Hill, 1989.

[56] S. Timoshenko, *Theory of Plates and Shells*. New York, NY: McGraw-Hill, 1987.

[57] K.E. Petersen, "Dynamic Micromechanics on Silicon: Techniques and Devices," *IEEE Transactions on Electron Devices*, vol. ED-25, pp. 1241–1250, October 1978.

[58] H. Sadeghian, G. Rezazadeh, and P.M. Osterberg, "Application of the generalized differential quadrature method to the study of pull-in phenomena of MEMS switches," *Journal of Microelectromechanical Systems*, vol. 16, pp. 1334–1340, 2007.

[59] S. Chowdhury, M. Ahmadi, and W.C. Miller, "A closed-form model for the pull-in voltage of electrostatically actuated cantilever beams," *Journal of Micromechanics and Microengineering*, vol. 15, pp. 756–763, 2005.

[60] S. Chowdhury, M. Ahmadi, and W.C. Miller, "Pull-in voltage study of electrostatically actuated fixed-fixed beams using a VLSI on-chip interconnect capacitance model," *Journal of Microelectromechanical Systems*, vol. 15, pp. 639–651, 2006.

[61] R.A. Anderson, *Fundamentals of Vibrations*. New York, NY: Macmillan, 1967.

[62] W.S. Best, A. Karnik, and J. Parkes, "Integrated Design and Simulation of RF-MEM Devices." Coventor presentation, January 2002.

[63] E.S. Hung and S.D. Senturia, "Tunable Capacitors with Programmable Capacitance-Voltage Characteristic," in *Solid-State Sensor and Actuator Workshop*, (Hilton Head, SC), pp. 292–295, 1998.

[64] Coventor, Inc., 4000 Centegreen Way, suite 190, Cary, NC 27513.

[65] ANSYS Version 10.0, ANSYS, Inc., Southpointe, 275 Technology Drive, Canonsburg, PA 15317.

[66] COMSOL AB, Tegérgatan 23, SE-11 40, Stockholm, Sweden.

[67] MSC Software Corporation, 2 MacArthur Place, Santa Ana, CA 92707.

[68] J.R. Gilbert, R. Legtenberg, and S.D. Senturia, "3D Coupled Electro-Mechanics for MEMS: Applications of CoSolve-EM," in *Proceedings of MEMS*, (Amsterdam), pp. 122–127, 1995.

[69] Ansoft HFSS Version 11.0, Ansoft Corporation, 225 West Station Square Drive, Suite 200, Pittsburgh, PA 15219.

[70] ANSYS, Inc., Southpointe, 275 Technology Drive, Canonsburg, PA 15317.

[71] S. Moaveni, *Finite Element Analysis: Theory and Application with ANSYS*. Upper Saddle River, NJ: Prentice Hall, 1999.

[72] T. Itoh, *Numerical Techniques for Microwave and Millimeter-Wave Passive Structures*. New York, NY: John Wiley and Sons, Inc., 1989.

[73] D.M. Pozar, *Microwave Engineering*. New York, NY: John Wiley and Sons, Inc., second ed., 1998.

[74] S. Lucyszyn, "Microwave characterization of nickel," *EM Academy's PIERS Online Journal*, vol. 4, pp. 686–690, June 2008.

[75] R. M. Bozorth, *Ferromagnetism*. New York, NY: Van Nostrand, 1951.

[76] G. F. Hodsman, G. Eichholz, and R. Millership, "Magnetic dispersion at microwave frequencies," *Proceedings of the Physical Society Section B*, vol. 62, pp. 377–390, 1949.

[77] W. Arkadiew, "The absorption of electromagnetic waves on two parallel wires," *Annalen der Physik*, vol. 58, no. 2, pp. 105 – 138, 1919.

[78] I. Simon, "Magnetic permeability of nickel in the region of centimeter waves," *Nature*, vol. 157, p. 735, June 1946.

[79] S. Graham, J. Kelley, N. Yang, and T. Borca-Tasciuc, "The role of microstructure in the electrical and thermal conductivity of Ni-alloys for LIGA microsystems," *Microsystem Technologies*, vol. 10, pp. 510–516, October 2004.

[80] W.H. Safranek, *The Properties of Electrodeposited Metals and Alloys: A Handbook*. Orlando, FL: American Electroplaters and Surface Finishers Society, second ed., 1986.

[81] HFSS 11.1 User's Guide, 3rd Edition, February 20, 2009.

[82] Ansoft HFSS 8.5 Documantation, Technical Notes.

[83] PUFF Version 2.0, Computer aided design for microwave integrated circuits, R. Compton and D. Rutledge, Cornell University, Ithaca, NY, 1991.

[84] A. Ruzzu and B. Matthis, "Swelling of PMMA-structures in aqueous solutions and room temperature Ni-electroforming," *Microsystem Technologies*, vol. 8, no. 2-3, pp. 116–119, 2002.

[85] D.M. Klymyshyn, D.T. Haluzan, M. Börner, S. Achenbach, J. Mohr, and T. Mappes, "High aspect ratio vertical cantilever RF-MEMS variable capacitor," *IEEE Microwave and Wireless Components Letters*, vol. 17, pp. 127–129, 2007.

[86] D.T. Haluzan, D.M. Klymyshyn, M. Börner, S. Achenbach, G. Wells, T. Mappes, and J. Mohr, "Stiction issues and actuation of RF LIGA-MEMS variable capacitors," *Microsystem Technologies*, vol. 14, pp. 1709–1714, October 2008.

[87] Y.P. Zhao, L.S. Wang, and T.X. Yu, "Mechanics of adhesion in MEMS - a review," *Journal of Adhesion Science and Technology*, vol. 17, pp. 519–546, May 2003.

[88] C.H. Mastrangelo, "Suppression of stiction in MEMS," in *MRS Proceedings*, vol. 605, pp. 105–116, 1999.

[89] N. Tas, T. Sonnenberg, H. Jansen, R. Legtenberg, and M. Elwenspoek, "Stiction in surface micromachining," *Journal of Micromechanics and Microengineering*, vol. 6, pp. 385–397, December 1996.

[90] B.H. Kim, T.D. Chung, C.H. Oh, and K. Chun, "A new organic modifier for anti-stiction," *Journal of Microelectromechanical Systems*, vol. 10, pp. 33–40, March 2001.

[91] J.N. Israelachvili, *Intermolecular and surface forces*. New York, NY: Academic Press, first ed., 1985.

[92] C.H. Mastrangelo, "Adhesion-related failure mechanisms in micromechanical devices," *Tribology Letters*, vol. 3, no. 3, pp. 223–238, 1997.

[93] A.W. Adamson and A.P. Gast, *Physical Chemistry of Surfaces*. New York, NY: Wiley-Interscience, sixth ed., 1997.

[94] P.R. Scheeper, J.A. Voorthuyzen, W. Olthuis, and P. Bergveld, "Investigation of attractive forces between PECVD silicon nitride microstructures and an oxidized silicon substrate," *Sensors and Actuators, A: Physical*, vol. 30, pp. 231–239, February 1992.

[95] C.D. Bain, E.B. Troughton, Y.T. Tao, J. Evall, G.M. Whitesides, and R.G. Nuzzo, "Formation of monolayer films by the spontaneous assembly of organic thiols from solution onto gold," *Journal of the American Chemical Society*, vol. 111, pp. 321–335, January 1989.

[96] Z. Mekhalif, J. Riga, J.J. Pireaux, and J. Delhalle, "Self-assembled monolayers of n-dodecanethiol on electrochemically modified polycrystalline nickel surfaces," *Langmuir*, vol. 13, pp. 2285–2290, April 1997.

[97] W.R. Tyson and W.A. Miller, "Surface free energies of solid metals: estimation from liquid surface tension measurements," *Surface Science*, vol. 62, pp. 267–276, January 1977.

[98] E. Chibowski, A. Ontiveros-Ortega, and R. Perea-Carpio, "On the interpretation of contact angle hysteresis," *Journal of Adhesion Science and Technology*, vol. 16, pp. 1367–1404, October 2002.

[99] C. Ishiyama and Y. Higo, "Effects of humidity on Youngs modulus in poly(methyl methacrylate)," *Journal of Polymer Science, Part B: Polymer Physics*, vol. 40, pp. 460–465, March 2002.

[100] T. Abe, W.C. Messner, and M.L. Reed, "Effects of elevated temperature treatments in microstructure release procedures," *Journal of Microelectromechanical Systems*, vol. 4, pp. 66–75, June 1995.

[101] G.K. Fedder and R.T. Howe, "Thermal assembly of polysilicon microstructures," in *Proceedings of IEEE Micro Electro Mechanical Systems (MEMS)*, pp. 63–68, 1991.

[102] C.H. Mastrangelo and G.S.Saloka, "Dry-release method based on polymer columns for microstructure fabrication," in *Proceedings of IEEE Micro Electro Mechanical Systems (MEMS)*, pp. 77–81, February 1993.

[103] T. Abe, W.C. Messner, and M.L. Reed, "Effective methods to prevent stiction during post-release-etch processing," in *Proceedings of IEEE Micro Electro Mechanical Systems (MEMS)*, pp. 94–99, 1995.

[104] H. Guckel, J.J. Sniegowski, T.R. Christenson, S. Mohney, and T.F. Kelly, "Fabrication of micromechanical devices from polysilicon films with smooth surfaces," *Sensors and Actuators, A: Physical*, vol. 20, pp. 117–122, November 1989.

[105] L.-S. Fan, Y.-C. Tai, and R.S. Muller, "IC-processed electrostatic micro-motors," in *Technical Digest - International Electron Devices Meeting*, vol. 20, pp. 666–669, IEEE, December 1988.

[106] Y. Zhao, "Stiction and anti-stiction in MEMS and NEMS," *Acta Mechanica Sinica*, vol. 19, pp. 1–10, February 2003.

[107] Z. Mekhalif, F. Laffineur, N. Couturier, and J. Delhalle, "Elaboration of self-assembled monolayers of n-alkanethiols on nickel polycrystalline substrates: time, concentration, and solvent effects," *Langmuir*, vol. 19, pp. 637–645, January 2003.

[108] C.H. Mastrangelo and C.H. Hsu, "Simple experimental technique for the measurement of the work of adhesion of microstructures," in *Solid-State Sensor and Actuator Workshop*, pp. 208–212, June 1992.

[109] D.T. Haluzan, D.M. Klymyshyn, S. Achenbach, M. Börner, and J. Mohr, "VM-TEST: Mechanical property measurement using electrostatically actuated vertical MEMS test structures fabricated in thick metal layers," *Microsystem Technologies*, vol. 18, pp. 443–452, April 2012.

[110] D.T. Haluzan, D.M. Klymyshyn, S. Achenbach, and M. Börner, "Reducing pull-in voltage by adjusting gap shape in electrostatically actuated cantilever and fixed-fixed beams," *Micromachines*, vol. 1, pp. 68–81, July 2010.

[111] P.G. Slade and E.D. Taylor, "Electrical breakdown in atmospheric air between closely spaced (0.2 μm - 40 μm) electrical contacts," *IEEE Transactions on Components and Packaging Technologies*, vol. 25, pp. 390–396, September 2002.

[112] W.K. Schomburg, H.J. Baving, and P. Bley, "Ti- and Be-X-ray masks with alignment windows for the LIGA process," *Microelectronic Engineering*, vol. 13, pp. 323–326, March 1991.

[113] V. Saile, U. Wallrabe, O. Tabata, and J.G. Korvink, eds., *Advanced Micro & Nanosystems Vol. 7. LIGA and its Applications*. Weinheim, Germany: Wiley-VCH, 2009.

[114] S. Achenbach, F.J. Pantenburg, and J. Mohr, "Numerical simulation of thermal distortions in deep and ultra deep X-ray lithography," *Microsystem Technologies*, vol. 9, pp. 220–224, January 2003.

[115] M. Schaffer, "High aspect ratio microstructure coupler," M.Sc., University of Saskatchewan, Saskatoon, Saskatchewan, February 2011.

[116] E.S. Hung and S.D. Senturia, "Extending the travel range of analog-tuned electrostatic actuators," *Journal of Microelectromechanical Systems*, vol. 8, pp. 497–505, December 1999.

[117] R. Legtenberg, J. Gilbert, S.D. Senturia, and M. Elwenspoek, "Electrostatic curved electrode actuators," *Journal of Microelectromechanical Systems*, vol. 6, pp. 257–265, September 1997.

[118] F. Najar, S. Choura, S. El-Borgi, E.M. Abdel-Rahman, and A.H. Nayfeh, "Modeling and design of variable-geometry electrostatic microactuators," *Journal of Micromechanics and Microengineering*, vol. 15, pp. 419–429, March 2005.

[119] M.M. Abdalla, C.K. Reddy, W.F. Faris, and Z. Gürdal, "Optimal design of an electrostatically actuated microbeam for maximum pull-in voltage," *Computers & Structures*, vol. 83, pp. 1320–1329, June 2005.

[120] C.W. Baek, Y.K. Kim, Y. Anh, and Y.H. Kim, "Measurement of the mechanical properties of electroplated gold thin films using micromachined beam structures," *Sensors and Actuators, A: Physical*, vol. 117, pp. 17–27, January 2005.